Reactive Infiltration Processing and Compression Creep of NiAl and NiAl Composites

by

T.A. Venkatesh

Submitted to the Department of Materials Science and Engineering
in partial fulfillment of the requirements for the degree of

Doctor of Philosophy in Metallurgy

at the

MASSACHUSETTS INSTITUTE OF TECHNOLOGY

JUNE 1998

Author.....
Department of Materials Science and Engineering
May 1, 1998

Certified by.....
David C. Dunand
AMAX Associate Professor of Materials Engineering
Thesis Supervisor

Accepted by.....
Linn W. Hobbs
John F. Elliott Professor of Materials
Chairman, Departmental Committee on Graduate Students

Reactive Infiltration Processing and Compression Creep of NiAl and NiAl Composites

by

T.A. Venkatesh

Submitted to the Department of Materials Science and Engineering on May 1, 1998 in partial fulfillment of the requirements for the degree of Doctor of Philosophy in Metallurgy

Abstract

Reactive infiltration processing of bulk and composite NiAl was investigated with powder and wire preforms of nickel. Inhomogeneous microstructures were often obtained with powder preforms because their high surface-to-volume ratio, low permeability, and irregular infiltration paths lead to simultaneous infiltration and reaction. Homogenous NiAl could be obtained with nickel-wire preforms which had a lower surface-to-volume ratio, higher permeability, and regular infiltration paths, because infiltration was completed before the onset of reaction. Composites with continuous tungsten (W) and sapphire fibers were also successfully fabricated by reactive infiltration, while composites with molybdenum particulates and short-fibers showed significant dissolution in NiAl.

The high-temperature uni-axial compression creep behavior of uni-directionally reinforced continuous fiber composite materials was investigated using NiAl-W as a model system for the case where both the NiAl matrix and the W fiber underwent plastic deformation by creep. The creep behavior of the constituents NiAl and W and NiAl composites reinforced with 5-20 volume % W was characterized at 1025°C and 715°C. At 1025°C, the NiAl-W composites exhibited three stage creep behavior with distinct primary, secondary, and tertiary creep, wherein the composite creep-rate decreased monotonically, remained constant, and increased rapidly, respectively. At 715°C, the NiAl-W composites exhibited insignificant primary and tertiary creep but significant secondary creep. Microstructurally, primary and secondary creep were characterized by pure uni-axial compression of W fibers while brooming, bulging, buckling, and kinking were four fiber deformation modes that contributed to tertiary creep.

The composite primary creep was modeled by solving for transient stress-states while loads transferred from the weaker phase (matrix) to the stronger phase (fiber) as the composite transitioned from the elastic state present at loading to steady-states attained at later times. The effects of primary creep of the constituents on the primary creep of the composite were also captured. Composite primary creep strains were predicted to be significant at high applied composite stresses and for high fiber volume fraction composites, while the composite primary time was uniquely related to the composite steady-state creep-rate by a power-law at a given temperature and for the stress-range investigated. Good correlation between the primary creep model predictions and experiments was obtained when the observed composite steady-state creep behavior converged to the McLean steady-state.

The composite secondary creep was observed to correlate reasonably well with the rule-of-mixtures model developed by McLean.

The composite tertiary creep was modeled by solving for global or local kink-band evolution with composite deformation respectively contributing to fiber buckling or kinking. The model predicted the critical threshold strain for the onset of tertiary stage to be most sensitive to the initial kink angles while being relatively insensitive to the initial kink-band heights and varied inversely with the volume fraction of fiber in the composite. Reasonable correlation between the model and experiments was obtained when the observed composite steady-state correlated well with the McLean steady-state.

Thesis Supervisor: Prof. David C. Dunand
Title: AMAX Associate Professor of Materials Engineering

CONTENTS

LIST OF FIGURES

LIST OF TABLES

ACKNOWLEDGEMENTS

I would like to acknowledge:

Prof. David Dunand for providing me funding support through a research assistantship and thereby a wonderful opportunity to experience MIT. His trust, confidence, and interest in helping me learn to define, develop, and complete, research work on a fairly independent basis is deeply appreciated.

The Department of Materials Science and Engineering for supporting me through two teaching assistantships.

Prof. David Roylance, Prof. S. Mark Spearing, and Prof. Subra Suresh for agreeing to serve on my thesis committee, graciously reviewing my thesis at short-notice, and giving me many helpful suggestions.

Prof. Subra Suresh for his interest, empathy, and generosity in offering office-space and computational facilities that have greatly enabled me to finish writing up this thesis in a short time.

Prof. Andreas Mortensen for many helpful discussions on the reactive infiltration processing project as well as for providing free access to the use of his laboratory facilities. Assistance from Chris SanMarchi towards experimental set-up is gratefully acknowledged.

Prof. Ali Argon for helpful discussions on the kinking behavior of composites.

Prof. Ronald Ballinger for providing free access to his laboratory facilities which enabled me to perform creep-tests on tungsten wires. Assistance from David Grundy and Pete Stahl towards experimental set-up is gratefully acknowledged.

V. T. Srikar for helpful discussions on the primary creep model.

Group-mates: Kristi Fukami-Ushiro, Ann Jansen, Raj Vaidyanathan, and Mike Whitney; and
Group-visitors: Hermann Holzer, Angeliki Lakkis, Jean-Marc Lefeuvre, Jacques Teisen, and Christian Verdon;
for being a wonderful group.

Sumanth and Bhuvana Kaushik, Rizwan Koita, Pradeep Sreekanthan, V.T. Srikar, Sankar Sunder, Srinivas Sunder, and S.R. Venkatesh: for many a good laugh over the patented bagel-coffee routine that has produced some of the finest theories on life, science, politics, arts, people, and any issue of any significance (*I'm impressed!*).

Most importantly my parents and my sister who have always been there to encourage, support, love, and care for me through the years.

1 INTRODUCTION

In the broadest sense, the Materials Science and Engineering discipline investigates materials processing, structure, and properties with a view to understanding and optimizing material performance. This thesis captures this essence in a holistic manner by:

- developing a novel processing technique to produce advanced technologically important intermetallic NiAl and its composites;
- characterizing the microstructure and creep properties of pure NiAl and W as well as NiAl-W composites; and
- developing and validating continuum level mechanical models to capture the physics of compressive deformation of NiAl-W long-fiber composites for the case when both the NiAl matrix and the W fiber undergo plastic deformation by creep, and thus extending for general applicability to the generic case of a creeping fiber/creeping matrix system.

This chapter addresses briefly the rationale behind the choice of:

- NiAl-W as the material system selected for investigation;
- Reactive infiltration as the processing technique developed to fabricate NiAl and its composites; and
- Compression creep of long-fiber composites as the mechanics issue that is investigated.

1.1 Why NiAl, W, and NiAl-W?

- Ever since the first intermetallic compound β-brass was discovered by Karl Karsten in 1839, intermetallics have been the subject of research primarily because they present unusual and often unexpected discontinuities in physical, chemical, mechanical or magnetic properties at specific chemical compositions [1].

- The intermetallic NiAl with its low density, high melting point, good oxidation resistance, high thermal conductivity as well as a wide range of compositional stability has been considered as a potential candidate for replacement of nickel-based superalloys and for the matrix material of composites in high-temperature structural applications [2-4]. However there are two main mechanical property limitations of NiAl: poor creep strength at high temperatures; and low ductility and toughness below the brittle-to-ductile transition temperature [5].

- Metallic tungsten with its high melting point (highest for any metal), excellent density corrected creep strength (because of its lowest homologous temperature), relative ductility, easy and inexpensive availability compared to ceramic fibers, has been considered as a potential candidate for reinforcement in composites designed for high-temperature structural

applications [6]. However there is one main chemical property limitation of W: poor oxidation resistance above 600°C.

- The addition of creep-resistant and relatively ductile W to NiAl enhances the high temperature creep strength of NiAl by composite strengthening, and low temperature toughness of NiAl by ductile phase toughening mechanisms. NiAl protects W from oxidation due to its excellent oxidation resistance. Additionally, the NiAl-W system exhibits excellent thermodynamic stability thus enhancing the utility of the composite.

1.2 Why Reactive Infiltration Process?

As advanced materials with high melting points, NiAl and its composites are difficult and expensive to process by conventional techniques.

Reactive infiltration, an elegant cost-effective process provides for an inexpensive method to fabricate NiAl and by virtue of its flexibility to produce composites also provides a method to address the mechanical property limitations of NiAl.

An understanding of the microscopic and macroscopic factors that control reactive infiltration of NiAl is first developed and the fabrication of NiAl composites by reactive infiltration is demonstrated in Chapter 2.

1.3 Why compression creep?

While uni-axial compression is the simplest stress-state imaginable that can be imposed on a material from a mechanics point of view, the strain response induced in the material can range from a simple linear uni-axial elastic deformation to a complex non-linear multi-axial plastic deformation, depending on intrinsic material factors such as micro-and macro-structure as well as extrinsic factors such as stress and temperature.

1.3.1 Monolithic homogeneous materials

The compressive response of homogeneous isotropic monolithic materials has been studied since 1744 [7] and is well understood. It could be one of five types depending on the temperature as well as the presence or absence of any initial imperfections in the material as indicated in Figure 1.

At low temperatures when creep is not a dominant deformation mechanism, elastic materials with perfect geometries and no initial imperfections will exhibit:

- a linear elastic behavior following Hooke's law if the material obeys linear elasticity; or
- a non-linear elastic behavior if the material follows rubber elasticity;

for stresses below a certain critical limit as defined by Euler. The Euler stresses for different end-constraints [8] are as indicated in Figure 2.

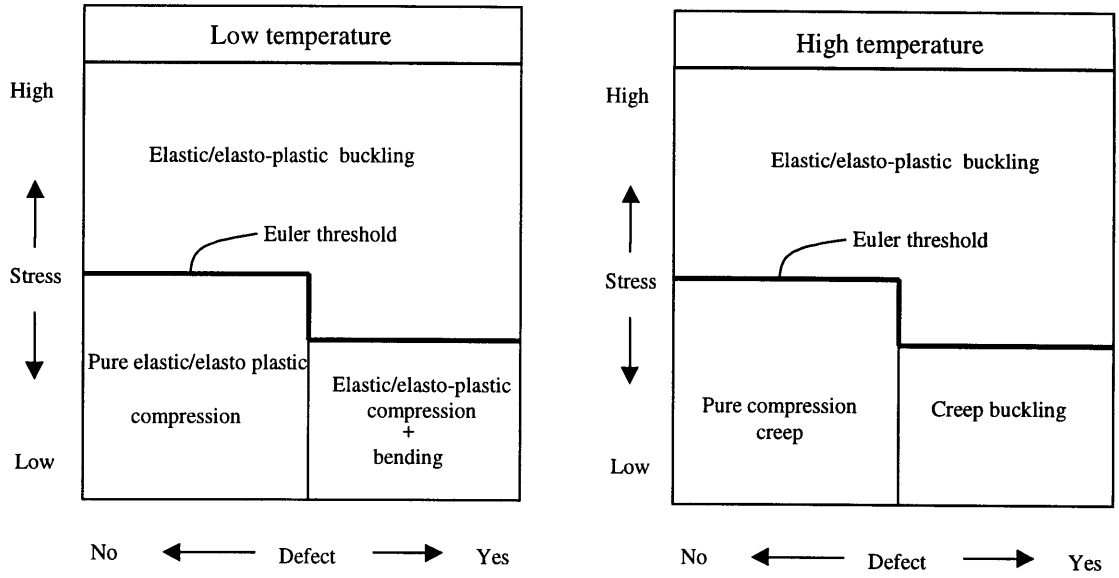

Figure 1. Schematic illustrating domains of mechanical stability for a homogenous monolithic material at low and high temperatures.

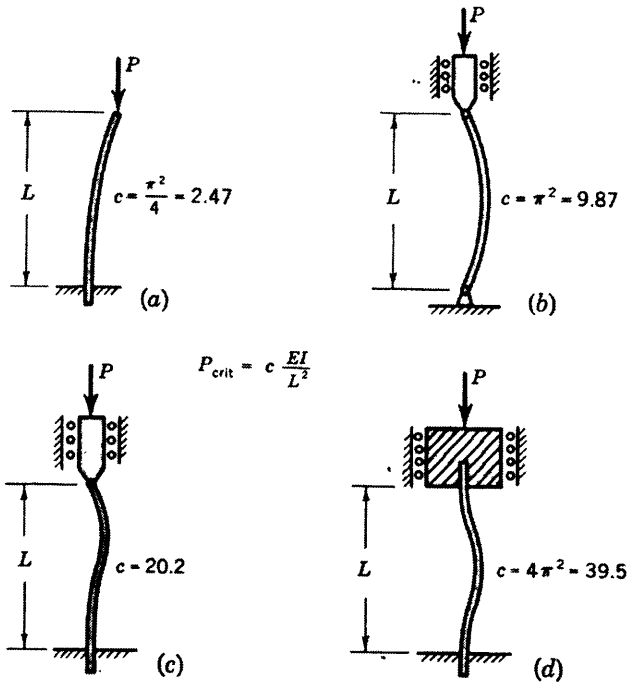

Figure 2. Euler buckling loads for various end-constraint conditions where P_{crit} is critical buckling load, E is Young's modulus and I is moment of inertia of the member under compression [8].

For stresses above the critical Euler stresses, the buckled configuration presents a lower energy state compared to the unbuckled straight form. Hence the system buckles rapidly to relieve the high elastic strain-energy accumulated in the system and achieve a lower energy configuration.

At high temperatures, below the Euler buckling threshold stress, the material will creep under pure compression if there are no initial imperfections and will exhibit time dependent creep buckling if the stresses are below the Euler limit. If the stresses are above the Euler limit, the material will exhibit instantaneous elastic or elasto-plastic buckling.

1.3.2 Composite materials

Monolithic homogeneous isotropic materials can be combined to form composite materials with varying degrees of microscopic structural homogeneity and corresponding macroscopic mechanical isotropy as indicated in Figure 3.

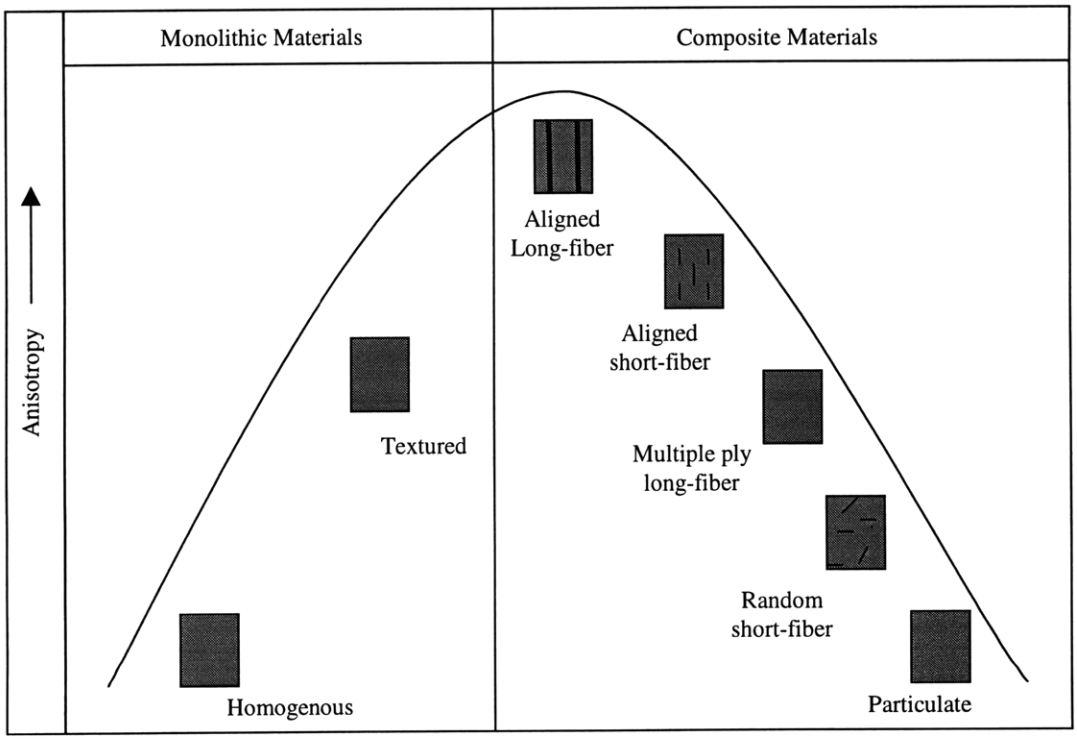

Figure 3. Schematic illustrating the relative anisotropy of monolithic materials and composite materials.

When composite materials are engineered primarily to enhance the specific strength of the material (be it directional or uniform), the *stability* of the resulting composite (particularly in compression) may not necessarily scale with the *strength* of the composite posing a serious design limitation and thus limiting the utility of the composite. This is particularly true for long-fiber composites which display the highest degree of anisotropy among the class of materials illustrated.

Hence this system has been the subject of study since 1965 [9][Figure 4]. Three approaches have been undertaken to check for and characterize instabilities in the long-fiber composite system:

- analytical modeling
- finite element/numerical modeling
- experimental analysis.

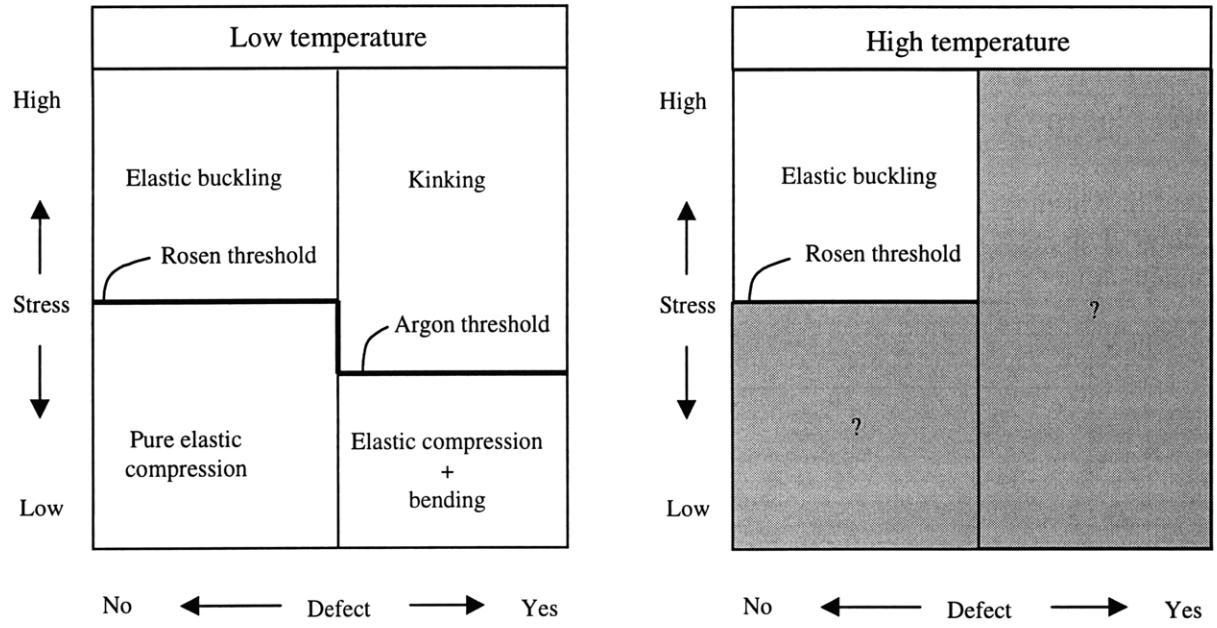

Figure 4. Schematic illustrating domains of mechanical stability for long-fiber composite materials to be well characterized for low temperatures and yet to be well understood for high temperatures.

At low temperatures, when perfectly aligned defect-free long-fiber composites are stressed in compression, stable elastic or elasto-plastic behavior is observed for stresses below a critical limit defined by Rosen [9]. Above this stress, the fibers embedded in the elastic matrix exhibit elastic instability and contribute to the failure of the composite.

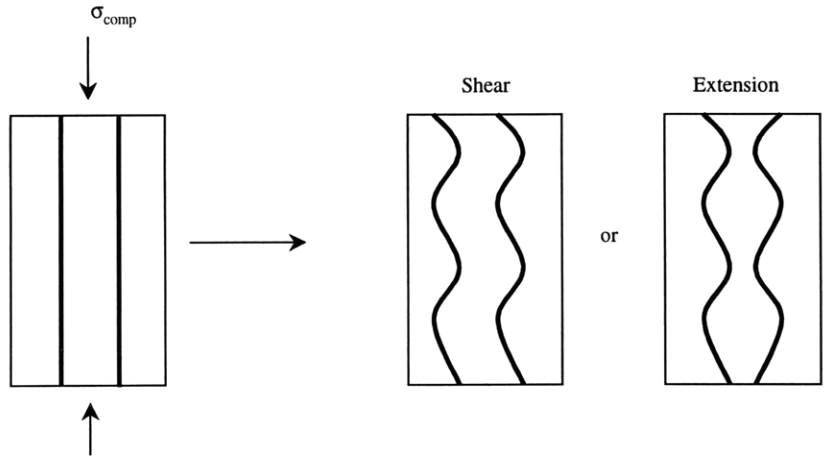

Figure 5. Schematic illustrating two possible modes of fiber failure – shear mode when the fibers buckle in phase and extensional mode when the fibers buckle out-of-phase with each other when the applied stress reaches the Rosen critical stress [9].

Depending on the mode of instability [Figure 5] – shear mode or extensional mode, the compressive strength σ_c of the composite is given respectively as [9]:

$$\sigma_c = \frac{G_m}{1 - v_f} \quad [1]$$

$$\sigma_c = 2v_f \left[\frac{v_f E_m E_f}{3(1 - v_f)} \right]^{1/2} \quad [2]$$

where G_m is the shear modulus of the matrix, v_f the volume fraction of fibers, and E_m and E_f are Young's moduli of the matrix and fiber respectively.

With the introduction of correction coefficients, these formulae are able to predict the compressive strength of almost defect-free high-quality composites reasonably well [10]. However, it has been shown [11] that for almost all commercial fiber composites, the prediction based on these equations, are significantly in excess of the compressive strength measured in experiments. This overestimate of compressive strength cannot be reduced by refining Rosen's elastic buckling analysis.

Argon [12] argued that processing of fiber composites inherently results in local imperfections in the fibers [Figure 6]. Upon application of a global compressive stress, local shear stresses are generated in the regions of imperfections. When the resolved shear stress in the direction of the misaligned fibers reaches the shear yield stress of the matrix, a shearing instability designated as kinking occurs leading to composite failure.

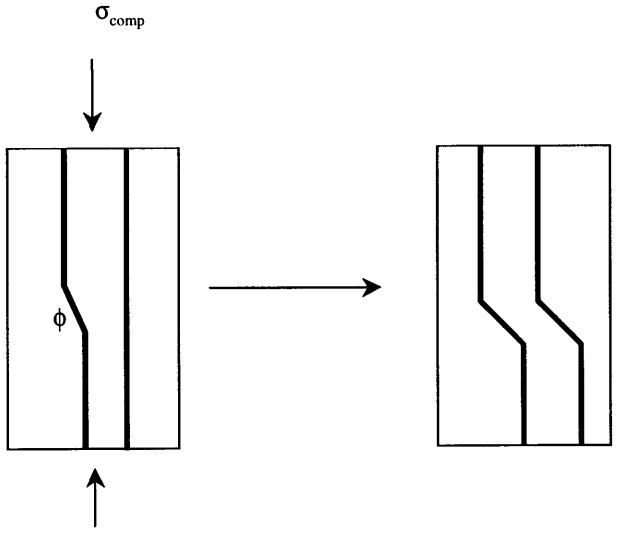

Figure 6. Schematic illustrating kinking mechanism as proposed by Argon [12].

From this argument the prediction of the compressive strength takes the simple form [12]:

$$\sigma_c = \frac{\tau_y}{\phi} \qquad [3]$$

where τ_y is the shear yield strength of the matrix and ϕ represents the initial fiber misalignment. This criterion, combining initial fiber misalignment and matrix plasticity gives satisfactory predictions of compressive strength of composites with typical fiber misalignments of 2-3°.

Actually, Eq. [3] was derived for rigid - perfectly plastic kinking. Budiansky [13] extended the result to elastic-perfectly plastic kinking:

$$\sigma_c = \frac{\tau_y}{\gamma_y + \phi} \qquad [4]$$

where γ_y is shear yield strain of the composite. Subsequently, Budiansky and Fleck [14] extended Eq. [4] to include matrix strain hardening. Assuming a Ramberg-Osgood shear stress-strain relation:

$$\frac{\gamma}{\gamma_y} = \frac{\tau}{\tau_y} + \alpha\left[\frac{\tau}{\tau_y}\right]^n \qquad [5]$$

where γ is the shear strain and τ is the shear stress, α is a constant, n is a strain-hardening exponent and subscript y represents the respective parameters at yield of the material, they obtained an expression for the compressive strength given by:

$$\frac{\sigma_c}{G_c} = \left[1 + n\alpha^{1/n}\left[\frac{\phi/\gamma_y}{n-1}\right]^{n-1/n}\right]^{-1} \qquad [6]$$

where G_c is the composite shear modulus. Budiansky and Fleck [14] found that strain hardening does not significantly alter the kinking stress predicted by Eq. [3].

Recently several other researchers have investigated the compressive failure mechanisms in long-fiber composite materials [15, 16] and have extended this analysis to look specifically at kink band initiation and propagation mechanisms.

Experimental work has been carried out by numerous researchers as reviewed by Waas and Schultheisz [11, 17].

Thus it is evident that the low temperature behavior of long-fiber composites has been well characterized. But the high-temperature compressive behavior is yet to be analyzed in a systematic manner. Through experiments, analytical formulation, and numerical analysis, Chapter 3 discusses the characterization of the compressive creep behavior of the long-fiber composite system for the particular case wherein both the matrix and the fiber undergo plastic deformation by creep.

Finite elements are not employed in this work for the following reasons:

- A simple 2-D formulation for developing a generic unit-cell model relies on the existence of periodicity in sample geometries as well as the deformation behavior. Real composites exhibit aperiodicity in sample geometry and more importantly in the deformation behavior when fibers bend globally or kink locally. Thus the generic 2-D unit-cell models would not adequately capture the true composite behavior.

- Aperiodicity in sample geometry can be captured by constructing special 2-D unit-cell models which will yield solutions to certain special conditions of fiber arrangement or deformation. However a general solution to the general composite creep behavior would still not be obtained.

- The most general solution that accounts for aperiodicity and out-of-plane deformations of the fiber can be obtained by constructing a 3-D model that meshes all fibers present in a given sample. However as all the fibers in a given sample have to be meshed and monitored for their response to the various input and boundary conditions, this approach is expected to be time and resource intensive.

2 REACTIVE INFILTRATION PROCESSING OF NiAl AND NiAl COMPOSITES

2.1 Introduction

The intermetallic NiAl exhibits low density, high melting point, good oxidation resistance, high thermal conductivity as well as a wide range of compositional stability [Figure 7] and is thus a potential candidate for replacement of nickel-based superalloys and for the matrix material of composites in high-temperature structural applications [2-4]. The two main limitations of NiAl as a structural material are its poor creep strength at high temperatures and its low ductility and toughness below the brittle-to-ductile transition temperature. Addition of ceramic or refractory metallic reinforcements can address the first problem by composite strengthening and the second problem by ductile phase toughening, crack bridging or crack deflection [5, 18].

However, because of their high melting point and reactivity, NiAl and NiAl composites are difficult to process by conventional casting, pressure infiltration or powder metallurgy techniques. Reactive processing, where two components nickel and aluminum react exothermally and drive the reaction toward completion, has the potential to simplify these processing problems [19] because the following advantages of reactive processing:

- Tremendous energy savings are achieved as the internal heat of reaction is utilized optimally with minimal external energy requirement;
- Short production cycles and minimal contamination of the product are realized due to rapid heating and cooling process cycles;
- High purity of product is ensured due to evaporation of volatile impurities at the high temperatures reached in the process;
- Ease of composite fabrication; and
- Ease of near net-shape processing.

outweigh the following disadvantages of reactive processing:

- Reactions are very sensitive to process conditions;
- Reactions can often be difficult to control; and
- Chemically homogenous products are not always obtained due to incomplete reaction and/or mixing.

Reactive powder metallurgy, where mixed nickel and aluminum powders are reacted, is difficult for NiAl because the large amount of heat released during reaction causes slumping [20] and because of the formation of pores [21]. Reactive infiltration, a recently developed method where liquid aluminum infiltrates and reacts with a nickel preform [22-28], provides an attractive alternative. It is also well suited for the fabrication of NiAl composites with reinforcements such

as alumina, tungsten, and molybdenum, which exhibit excellent thermodynamic stability with NiAl at typical processing and component service temperatures.

The objectives of the present investigation are to develop an understanding of the microscopic and macroscopic factors that control reactive infiltration of NiAl and to demonstrate the fabrication of NiAl composites by reactive infiltration.

2.2 Experimental procedures

NiAl and NiAl based composites were fabricated by reactive infiltration of nickel-powder and nickel-wire preforms with aluminum as indicated in Table 1.

Table 1. NiAl and NiAl-composites are fabricated by reactive infiltration with liquid aluminum of nickel-powder and nickel-wire preforms with and without reinforcements as indicated.

		NiAl	NiAl-Composites		
			Particulate	Short-fiber	Long-fiber
Nickel preform	Powder		• Molybdenum (<1 μm)	• Molybdenum (127 μm ø, 3 mm-4 mm l)	
	Wire				• Sapphire (125 μm ø) • Molybdenum (127 μm ø) • Tungsten (250 μm ø)

Optical metallography, back-scattered scanning electron microscopy (SEM), and electron-microprobe analysis (EMPA) studies of NiAl and NiAl-composites were performed in order to characterize the microstructural features such as grain size, porosity, homogeneity, and nature of the reinforcement-matrix interface. All samples were prepared by polishing with SiC paper and 1 μm diamond paste. Optical metallographic samples were subsequently etched with Kalling's reagent (5 g of $CuCl_2$ in 100 ml of HCl) for 0.5 min to 1 min to reveal the microstructure.

2.2.1 Monolithic NiAl

2.2.1.1 Nickel-powder preform experiments

Alumina crucibles [Table 2] were packed with either a single layer [Figure 8a] or two layers [Figure 8b] of nickel powders [Table 3]. In the latter case, the lower layer consisted of fine nickel powder with a higher surface-area to volume ratio and the top layer consisted of coarse nickel powder with a lower surface-area to volume ratio [Table 4]. The lower layer because of its

higher reactivity was expected to react quickly with aluminum and release heat, thus triggering the reaction in the top layer.

Table 2. Crucibles used in reactive infiltration experiments with nickel-powder and nickel-wire preforms.

		Crucibles	
		Alumina	Quartz
Nickel preform	Powder	15 cm long 2.5 cm diameter	
	Wire		15-20 cm long 2.5 cm diameter

Table 3. Sources and specifications of all materials used in the reactive infiltration experiments.

Product	Purity [%]	Vendor
Argon	99.9	BOC, MA
Aluminum	99.99	ALCOA
Alumina crucibles	99.99	LSP Industrial Ceramics, Inc., Lambertville, NJ
Fiberfrax	-	The Carborandum Company, Niagara Falls, NY
Molybdenum powder Nickel, Molybdenum, and Tungsten wires	99.98	Johnson Matthey, Ward Hill, MA
Nickel powder	99.9	Sherritt Technologies, Fort Saskatchewan, AB, Canada
Quartz crucibles	99.9	Quartz Plus, Inc., Concord, MA
Sapphire	99.9	Advanced Crystal Product, Woburn, MA
Zircwash	-	ZYP Coatings, OakRidge, TN

Table 4. Experimental parameters for the fabrication of NiAl from nickel-powder preforms.

Code	Al-mass	Ni-lower layer		Ni-upper layer		T	P	t	Global nickel composition
		size	mass	size	mass				
	[g]	[μm]	[g]	[μm]	[g]	[°C]	[MPa]	[min]	[at. %]
A1	17.4	75-90	9.0	-	-	710	7.0	15	19.2
A2	15.0	25-53	10.1	-	-	721	6.3	15	23.6
A3	9.6	< 1 μm	7.0	-	-	700	7.0	10	25.1
B1	5.6	< 1 μm	3.6	25-53	6.4	700	7.0	10	44.9
B2	4.8	< 1 μm	3.1	25-53	7.1	700	7.0	10	49.6
B3	3.6	< 1 μm	3.5	25-53	7.5	700	7.0	10	58.1
B4	3.7	< 1 μm	3.5	25-53	9.0	700	7.0	10	60.8

T=Temperature; P=Pressure; t=time.

δ–alumina fiber wool (~ 1 cm in thickness) placed between the nickel bed and aluminum functioned as a gate that physically separated nickel from aluminum. A layer of insulation (~ 2 cm) was placed on top of the aluminum layer. The crucible was wrapped in Fiberfrax paper and placed in a steel container.

The entire set-up was then lowered in to a pressure infiltration rig described in Ref. [29] and heated under vacuum. Poor wetting of δ–alumina by molten aluminum held the liquid pool of

aluminum above the alumina gate. The rig was then pressurized with argon, forcing liquid aluminum to flow past the gate, infiltrating the preform and reacting with nickel to form NiAl. The pressure was maintained for a few minutes and released [Table 4]. The set-up was then allowed to cool in the residual argon atmosphere.

2.2.1.2 Nickel-wire preform experiments

Some alumina crucibles cracked as they were unable to absorb the thermal shock produced when nickel and aluminum reacted at 700°C to produce nickel aluminide at 1638°C in less than 10 seconds. Hence quartz crucibles [Table 2] with superior thermal shock resistance were used for the larger nickel-wire preform experiments wherein the reaction-induced thermal shock was expected to be more severe.

Flat bottomed quartz crucibles were coated with a zirconia slurry (Zircwash). This coating served as a reaction barrier and virtually eliminated silicon pickup from the quartz crucible by liquid aluminum prior to the reaction and by liquid NiAl after the reaction, thus reducing sample contamination. The coated crucibles were air dried at room temperature and at 200°C. Preforms of nickel were made by bundling chopped nickel wires to about 37% volume fraction, in order to be close to 1:1 stoichiometry of nickel and aluminum. These bundles were then introduced into the coated crucible and placed at one of two locations depending on the experimental configuration employed.

In the first configuration, the bundle was placed above the aluminum billet [Figure 8c]. Frictional forces held the bundle in place and prevented it from sliding down and contacting aluminum. The crucible was insulated with fibrous alumina at the top to minimize heat losses. The crucible was also wrapped with Fiberfrax paper and wool and placed in another graphite crucible. The assembly was lowered in to the pressure infiltration rig [29] and heated under vacuum. A plunger mechanism was then operated that gently slid the nickel wire-preform into the pool of liquid aluminum. Upon contact, nickel reacted with aluminum to form nickel-aluminide. The set-up was then allowed to cool under vacuum [Table 5].

Table 5. Experimental parameters for the fabrication of NiAl from nickel-wire preform using plunger mechanism.

Code	Ni-mass [g]	Al-mass [g]	Temperature [°C]	Pressure [MPa]	Global nickel composition [at. %]
D1	22.0	11.0	710	Vac	47.9
D2	35.0	16.0	710	Vac	50.1
D3	51.8	24.4	710	Vac	49.4
D4	63.2	28.8	710	Vac	50.2
D5	65.0	30.0	710	Vac	49.9

Table 6. Experimental parameters for the fabrication of NiAl from nickel-wire preform using gas-pressure mechanism.

Code	Ni-mass [g]	Al-mass [g]	Temperature [°C]	Pressure [MPa]	Time [min]	Global nickel composition [at. %]
E1	44.3	20.7	711	2.8	1	49.6
E2	45.3	21.8	710	2.8	1	48.9

In the second configuration, the nickel bundles were placed at the bottom of the crucible [Figure 8d]. A gating system comprising of a graphite ring with a graphite disk on top (1-2 mm in thickness and with uniformly-spaced 40 to 50 hand-drilled 0.8 mm holes) was placed on top of the wire preform. This gating system enabled liquid aluminum that was squeezed through the graphite disk to first collect in the reservoir space beneath the disk and then infiltrate the preform with a planar front [Table 6].

The required amount of pure aluminum was placed on top of the gate.

The crucibles were insulated and introduced into the pressure infiltration apparatus as described earlier. The set-up was heated under vacuum and the chamber was pressurized with argon, forcing liquid aluminum to infiltrate the preform and react with nickel to form NiAl. The pressure was maintained for a few minutes and released. The set-up was then allowed to cool in the residual argon atmosphere.

2.2.2 NiAl-Composites

2.2.2.1 Particulate composites

The nickel-molybdenum powder preforms were obtained by hand-blending the required volume fraction of molybdenum with nickel powder [Figure 8e]. Subsequent experimental set-up and procedures were identical to those described in § 2.2.1.1 on processing NiAl from powder preforms [Table 7].

Table 7. Experimental parameters for the fabrication of NiAl-Mo composites from nickel-powder preform.

Code	Ni-size	Ni-mass	Mo-form	Mo-mass	Al-mass	T	P	t	Composite composition [at. %]		
	[μm]	[g]		[g]	[g]	[°C]	[MPa]	[min]	Ni	Al	Mo
M1	25-53	9.0	Particulate	1.0	2.0	720	7	15	64.5	31.2	4.4
M2	25-53	10.0	Particulate	2.0	2.2	710	7	15	62.5	29.9	7.6
M3	25-53	10.0	Short-fiber	0.62	1.9	698	7	20	68.6	28.8	2.6
M4	25-53	10.2	Short-fiber	0.92	2.0	700	7	15	67.2	29.1	3.7

T=Temperature; P=Pressure; t=time.

2.2.2.2 Short-fiber composites

Short-fiber composites were fabricated by incorporating molybdenum fibers in the nickel-powder preforms [Figure 8f] and infiltrating the preform with liquid aluminum according to the procedure outlined in § 2.2.1.1 [Table 7].

2.2.2.3 Long-fiber composites

Long-fiber composites were fabricated by incorporating the required volume fraction of fibers (e.g. tungsten [Table 8], molybdenum or sapphire single crystals [Table 9]) in the nickel-wire preforms [Figure 8g]. Care was taken to maximize homogeneity in distribution and minimize distortion of the reinforcing fibers. Because NiAl is 14% denser (in the solid state at room temperature) than the corresponding equi-atomic mixture of metallic nickel and aluminum, the NiAl formed in the crucible had a height lower than that of the infiltrated, unreacted perform. Hence, fibers of the same height as the preform stood out from the liquid NiAl product, and clustered because of capillary effects [Figure 9], leading to an inhomogeneous distribution and misalignment of fibers in the composite. To eliminate this problem, a short layer of fiber-free nickel-wire preform was placed on top of the composite preform. After infiltration and reaction, this top molten layer served as a feed of NiAl compensating for the reaction volume shrinkage.

Table 8. Experimental parameters for the fabrication of NiAl-W composites from nickel-wire preform.

Code	Composite layer [g]		Feed layer [g]	Al [g]	T [°C]	P [MPa]	t [min]	Composite composition [at. %]		
	Ni	W	Ni					Ni	Al	W
F1	71.26	44.19	41.84	53.42	710	0.7	8	45	46	9
F2	72.68	45.55	41.77	51.43	714	3.5	7	46	45	9
F3	70.92	45.88	81.06	71.00	715	3.5	7	45	46	9
F4	64.40	41.08	48.95	50.66	710	3.5	20	45	46	9
F5	85.61	44.98	40.46	61.76	715	3.5	20	52	39	9
F6	63.76	40.89	50.06	50.83	712	3.5	5	45	46	9

T=Temperature; P=Pressure; t=Time.

Table 9. Experimental parameters for the fabrication of NiAl-Sapphire composites from nickel-wire preform.

Code	Composite layer [g]		Feed layer [g]	Al [g]	T [°C]	P [MPa]	t [min]	Composite composition [at. %]		
	Ni	Al_2O_3	Ni					Ni	Al	Al_2O_3
G1	74.91	~ 10	39.56	53.78	715	3.5	20	48	49	3
G2	75.07	~ 10	40.40	54.50	717	3.5	5	48	50	2
G3	76.18	~ 10	40.80	57.70	712	3.5	5	47	51	2

T=Temperature; P=Pressure; t=Time.

2.3 Results

2.3.1 Monolithic NiAl

2.3.1.1 Nickel-powder preform experiments

Reactive infiltration of the powder preforms (with and without a fuse) produced a complex mixture of various intermetallic phases [Figure 10 (a, b)]. Selected regions exhibited dendritic structures.

2.3.1.2 Nickel-wire preform experiments

Reactive infiltration of the wire preforms (with volume fractions near 0.37) resulted in ingots with a macrostructure characterized by a predominantly single-phase NiAl region with a porous aluminum-rich region at the ingot top [Figure 11]. The grain-size was approximately 200 μm [Figure 4(c-f)]. Some dendrites were found at the NiAl grain-boundaries [Figure 4d]. Certain grains also exhibited a sub-structure [Figure 4f]. Electron probe microanalysis indicated that within the NiAl region the elemental compositions varied linearly from about 53 at. % Ni towards ingot top to about 64 at. % Ni towards the ingot bottom [Figure 5].

2.3.2 NiAl Composites

2.3.2.1 Particulate composites

The nickel-molybdenum preforms were fully infiltrated and reacted. However all of the fine molybdenum particulates were dissolved by the nickel aluminide matrix [Figure 12(a-b)]. The microstructure was typically inhomogeneous and selected regions exhibited a dendritic structure.

2.3.2.2 Short-fiber composites

Powder preforms with randomly-oriented short molybdenum fibers were completely infiltrated and fully reacted to form a fairly homogeneous nickel aluminide matrix across the entire sample containing a few small pockets of partially reacted Ni-Al phases. In some cases, the NiAl-Mo interface exhibited a reaction layer possibly an Mo-Al intermetallic [Figure 12c], while in some other cases the interface was eroded due to molybdenum dissolution into the melt [Figure 12d].

2.3.2.3 Long-fiber composites

Wire preforms with aligned continuous tungsten or sapphire fibers were completely infiltrated and fully reacted to form an NiAl matrix in the bulk of the ingot with a porous aluminum-rich layer at the top of the ingot. In the case of NiAl-W composites, the tungsten fibers were quite

well aligned. While some tungsten dissolution and NiAl-W eutectic formation were observed [Figure 12f], the fiber/matrix interface was sharp with no reaction zones. Selected regions in the tungsten fibers were recrystallized [Figure 13]. The recrystallization zone was typically about 15 μm thick indicating that 22% of each of the W fibers had recrystallized to produce equi-axed grains with a size of about 10 μm. The core of the W wires retained their as-drawn texture and exhibited grains that were elongated (approximately 100 μm) in the longitudinal direction and about 2 μm along the width direction. In the case of NiAl-Al_2O_3 composites, there was evidence of fiber breakage and misalignment, but the interface appeared to be clean and the fibers unrecrystallized [Figure 12e].

2.4 Discussion

The reactive infiltration process comprises two steps, physical infiltration and chemical reaction. Dominance of either of these steps leads to two limits: (i) rapid reaction rate with low infiltration rate and (ii) rapid infiltration rate with low reaction rate [30].

Powder preforms, with high surface-to-volume ratios, low permeability and irregular infiltration paths, conform to the first limit. As different regions of the sample react at different times and to different extents, the resulting macrostructures are often characterized by an irregular distribution of multi-phase intermetallics. On the other hand, wire preforms with lower surface-to-volume ratio, higher permeability and more regular infiltration paths conform to the second limit. In this case reactive infiltration can be envisioned as two processes, infiltration and reaction, occurring in sequence and separated by an incubation period.

When aluminum reacts with nickel at 700°C under adiabatic conditions, thermodynamic calculations [28] predict that all of the product NiAl formed would be in the liquid state [Figure 14]. The dentritic structure of NiAl [Figure 11b] obtained confirms that NiAl is indeed formed in the liquid state and thus validates the assumption that the NiAl-formation reaction is near adiabatic.

It has also been demonstrated [31, 32] that reactive infiltration of nickel wire preforms resulted in ingots with five different macrostructures, independent of applied pressure but dependent on the global composition [Figure 16]:

- A predominantly single-phase NiAl region with aluminum-rich phases (Al_3Ni and Al_3Ni_2) at the ingot top (Type I);
- A single-phase NiAl region across the entire ingot length (Type II);
- A single-phase NiAl region with nickel-rich phase (Ni_3Al) at the ingot bottom (Type III);
- A single-phase NiAl region with partially infiltrated but unreacted nickel wires at the ingot bottom (Type IV);
- A homogenous structure of fully infiltrated but partially reacted nickel wires embedded in a near-eutectic (Al-Al_3Ni) material with thin layers of the intermetallics separating the eutectic-phase from the unreacted nickel wires (Type V).

Type I structure obtained at intermediate nickel concentrations between 38 at. % and 53 at. %, was attributed in part to the rapid movement of unreacted aluminum pools (density = 2.4 g/cc) to the top of molten NiAl (density ~ 5.0 g/cc) driven by buoyancy forces. With lower aluminum contents (i.e. higher nickel concentrations) this type of phase separation was not expected to happen and the resulting microstructure was single phase NiAl (Type II). At higher nickel concentrations, all of the available aluminum wetted the nickel wires before the bottom of the preform could be infiltrated. If the heat of reaction of formation of NiAl released at the top was sufficient to completely melt the nickel which remained at the bottom, a final macrostructure with a nickel-rich phase at the ingot bottom was obtained (Type III). At even higher nickel concentrations, the heat of the reaction was insufficient to melt all of the nickel wires at the bottom; the resulting microstructure then featured partially melted free nickel wires (Type IV). At high nickel concentrations and high preform volume fractions, the reaction to form NiAl was incomplete as it was quenched by the relatively large amount of unreacted nickel which acted as heat sink. Thus the preforms were largely unreacted (Type V).

The results of the present investigation which investigated reactive infiltration with nickel wire preforms with nickel concentrations around 50 at. % and volume fractions around 38 % produced ingots that conformed to and in good agreement with Type I discussed above.

While the NiAl composition was expected to be uniform at all locations in the ingot, a linear composition gradient with concentrations typically ranging from about 53 at. % Ni towards ingot top to about 64 at. % Ni towards the ingot bottom, was found. This macrosegregation could be explained as follows.

The aluminum that infiltrated the nickel preform could dissolve some nickel from the nickel wires. The aluminum present closer towards the infiltration front which swept through the entire preform and filled the preform-bottom was in contact with nickel for longer times and hence dissolved more nickel compared to the aluminum that filled the preform-top. Thus a concentration gradient in the liquid aluminum phase prior to its reaction with nickel to form NiAl, could have been developed with the aluminum at the preform-bottom being richer in nickel compared to the aluminum at the preform-top. Correspondingly the nickel preform was leaner in nickel towards the preform-top compared to the preform-bottom. Thus as the local compositions of the reactants nickel and aluminum were different at different locations in the preform before the reaction to form NiAl, the NiAl formed after the reaction also exhibits composition gradients.

The saturation limit of nickel in liquid aluminum at the infiltration temperature of 710°C is about 5 at. % [Figure 7a]. As the nickel dissolution in aluminum is exothermic, and the infiltration set-up well insulated, the heat of dissolution is expected to increase the aluminum temperature above the initial infiltration temperature (710°C) and thereby increase this saturation limit. The actual temperature increase could not be experimentally determined due to the following limitations:

- The infiltration and subsequent reactions were very fast, typically a few seconds and the crucibles were well insulated. Thus thermocouples placed outside the crucible were unable to record the relatively small temperature increase due to the release of the heat of dissolution.

- A thermocouple could not be placed inside the nickel-preform due to the limitations of the experimental set-up and as the set-up was opaque (as it was enclosed in a metallic pressure vessel) optical pyrometry could not be employed.

Hence the actual level of saturation could not be determined.

Thus this dissolution mechanism could explain in part the observed composition gradient (~11 at. %) in the ingot preform.

The second mechanism that contributes to global segregation, involves movement of parts of unreacted aluminum to the top of the preform driven by buoyancy forces, as discussed earlier.

The concentration gradients, if undesirable can be prevented, or if desirable can be accentuated, by preparing preforms with variable porosity/volume fraction. This could be obtained by:

- Preparing graded nickel preforms such that there is lower/higher nickel (i.e. more/less porosity) towards the preform-bottom compared to the preform-top while using crucibles with constant cross-sectional area and/or
- Preparing preforms with constant nickel concentration but using crucibles with increased/decreased cross-sectional area at the bottom (thus effectively increasing/decreasing porosity at the preform bottom).

Alternatively aluminum pre-saturated with about 5 at. % nickel, instead of pure aluminum, could also be used as the infiltrant to prevent further dissolution of nickel in aluminum and thus limit the level of macrosegregation. This technique could also be extended to fabricate microalloyed NiAl by using liquid aluminum alloys as the infiltrants.

At room temperature (25°C), the domain of existence of single phase NiAl is limited to concentrations between 44 at. % Ni and 59 at. % Ni at. % [Figure 7a]. Hence, if complete thermodynamic equilibrium is obtained in the reactive infiltration process then the mid-section of the ingot is expected to be single phase NiAl and the ingot bottom is expected to be a two-phase mixture of NiAl and Ni_5Al_3.

At high temperatures, the width of the single phase NiAl domain is larger (reaching a maximum at 1395°C wherein the range is between 42 at. % Ni and 68 at. % Ni) and thus nickel aluminide with 64 at. % Ni is also expected to be single phase NiAl at this temperature. Upon rapid cooling this nickel-rich NiAl can be retained in a metastable form at room temperature. As metallographic observations did not reveal two different phases at the ingot bottom, it can be concluded that the upon formation, the intermetallic NiAl cooled rapidly and thus complete thermodynamic equilibrium was not obtained.

The NiAl-Mo pseudo-binary eutectic phase diagram [33] predicts that 10.9 at. % molybdenum will be dissolved by liquid NiAl at its melting point of 1638°C [Figure 15a] if thermodynamic equilibrium is attained. The sub-micron sized Mo particulates that have a high specific surface area, do not present kinetic barriers to dissolution and thus reach thermodynamic equilibrium with NiAl almost instantaneously, while the dissolution of coarser molybdenum fibers (127 μm

diameter) that have a lower specific surface area is kinetically rate-limited and hence the dissolution-reaction does not reach the equilibrium state in the short-times that NiAl remains a liquid.

The NiAl-W pseudo-binary eutectic phase diagram [34] predicts that 2.0 at. % W will be dissolved by molten NiAl at 1638°C [Figure 15b] if thermodynamic equilibrium is attained. As the W fiber like Mo fiber has lower specific surface area, the dissolution of W is also expected to be kinetically rate-limited and be less than 2 at. %. Also in most cases only the peripheral regions of the W fibers were recrystallized, confirming that the samples remained at high temperatures only for very short times.

NiAl-sapphire composites are difficult to fabricate by conventional pressure casting techniques as NiAl does not wet sapphire fibers. Strong oxide forming additives such as Mg, Si, and Ti (5.0, 3.0, and 0.5 at. % respectively) are required to promote wetting and ensure complete infiltration [35]. The additives typically tend to segregate to NiAl-sapphire interfaces and/or the NiAl grain-boundaries, thus potentially reducing the efficiency of load transfer across the interface and/or reducing the fracture-toughness of NiAl by embrittling the grain-boundaries, respectively.

The present investigation also uses pressure to infiltrate composite preforms but relies primarily on wetting of Ni in the composite preform by liquid Al for successful infiltration. Subsequently as NiAl is formed in-situ, NiAl-sapphire composites are fabricated without the additives. It is thus possible to produce clean NiAl-sapphire interfaces with better load-transfer capability and additive-free NiAl cohesive grain-boundaries with better fracture toughness, thus enhancing the utility of the composite. However the sapphire fibers are lighter than molten NiAl and thus tend to rise in the liquid, leading to significant misalignment in the solidified composite produced by reactive infiltration. This problem could be addressed by mounting the sapphire fibers to the bottom of crucible and thus constraining the fibers from floating freely.

2.5 Conclusions

Reactive infiltration processing has been systematically investigated for the Ni-Al system. It has been demonstrated that:

- Infiltration temperature, infiltration pressure, preform volume fraction, preform permeability, and nature and quality of insulation are process variables that influence the success of reactive infiltration.

- Within the temperature and pressure ranges investigated (i.e. 700°C and 725°C; and 0.7 MPa and 7.0 MPa respectively) the process is relatively insensitive to infiltration temperature or pressure.

- The process displays a strong dependence on the nature of the preform employed. Upon reactive infiltration with liquid aluminum, nickel-powder preforms, which have high surface-to-volume ratios, low permeability, and irregular infiltration paths feature macro- and microscopically inhomogeneous mixtures of many Ni-Al intermetallic phases. Reactive infiltration of nickel-wire preforms, which have lower surface-to-volume ratio, higher

permeability, and regular infiltration paths produce homogeneous NiAl microstructures with composition gradients.

- It is kinetically near impossible to prevent substantial dissolution of fine Mo particulates into the NiAl matrix. Thus this process is not suitable for fabricating NiAl with low volume fractions of fine Mo particulates.

- Randomly-oriented NiAl-Mo short-fiber composites and aligned NiAl-W and NiAl-sapphire long-fiber composites can be successfully fabricated by reactive infiltration.

2.6 Figures and Illustrations

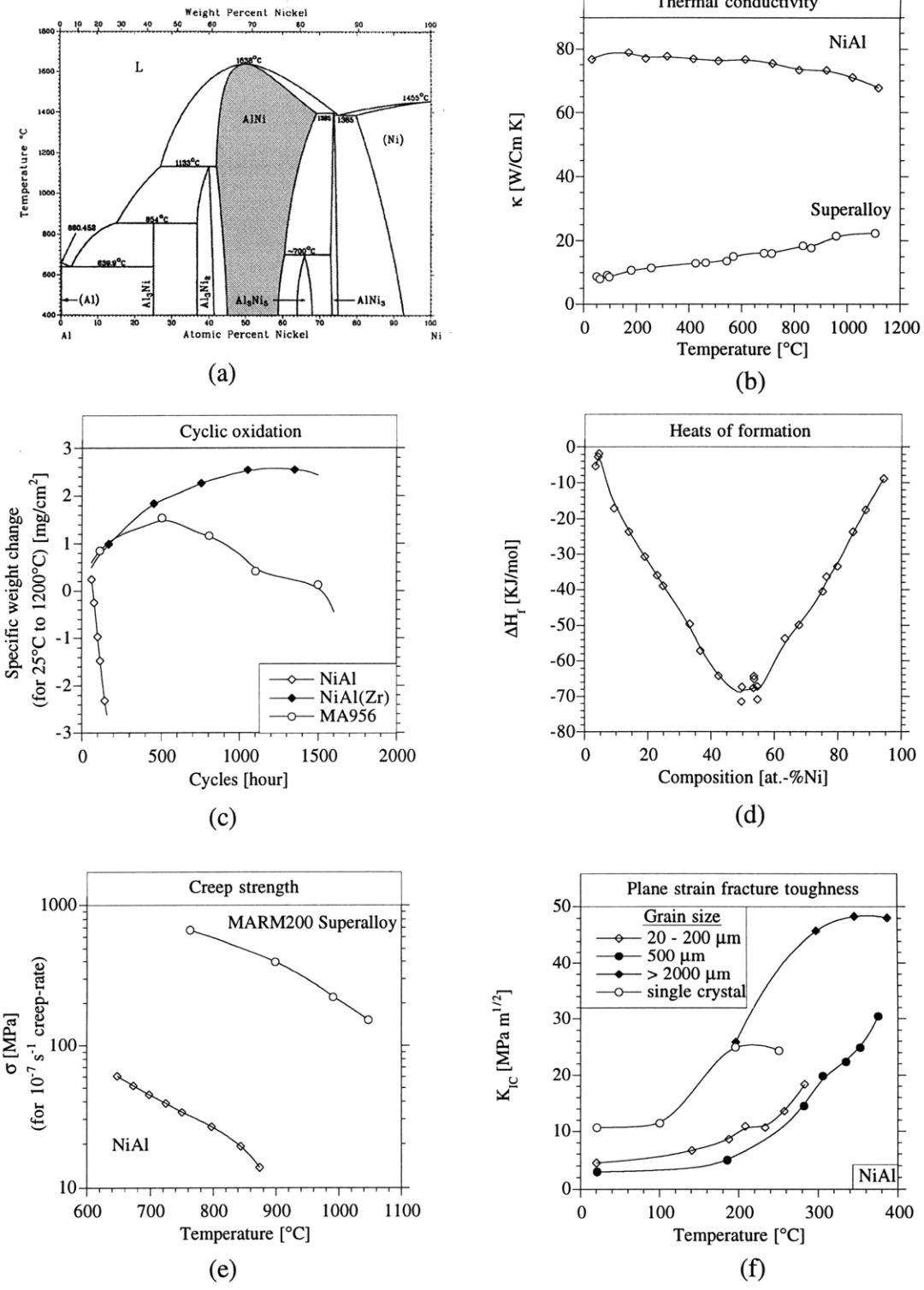

Figure 7. Physical (a[36]-b[37]), chemical (c[38]-d[3]), and mechanical (e[39]-f[40]) properties of NiAl.

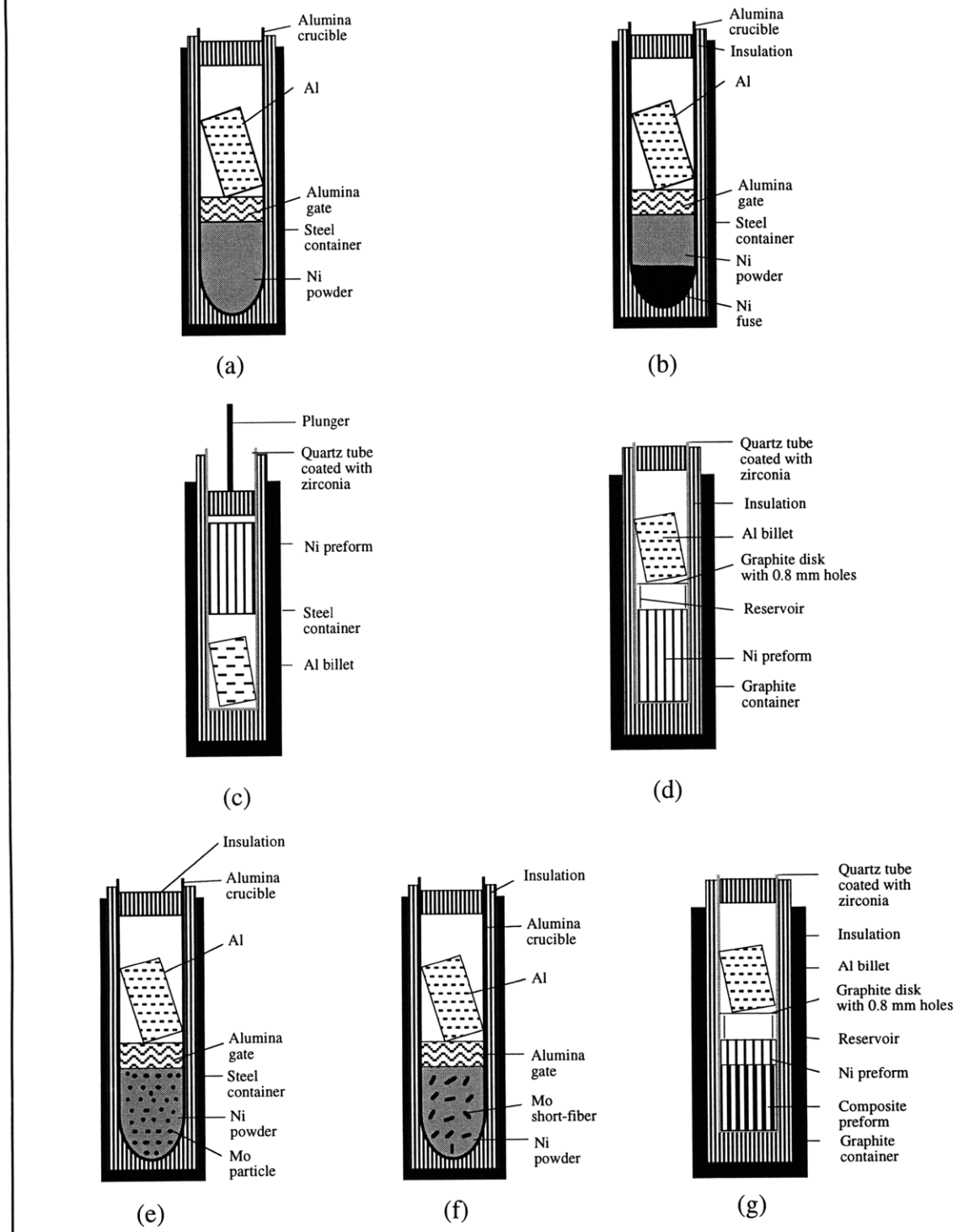

Figure 8. Schematics illustrating processing of:
(i) NiAl from one-layered (a) and two-layered (b) Ni-powder preforms;
(ii) NiAl from Ni-wire preforms using plunger (c) and gas pressure (d) mechanisms; and (iii) NiAl-composites with Mo (e-f), W and Sapphire (g).

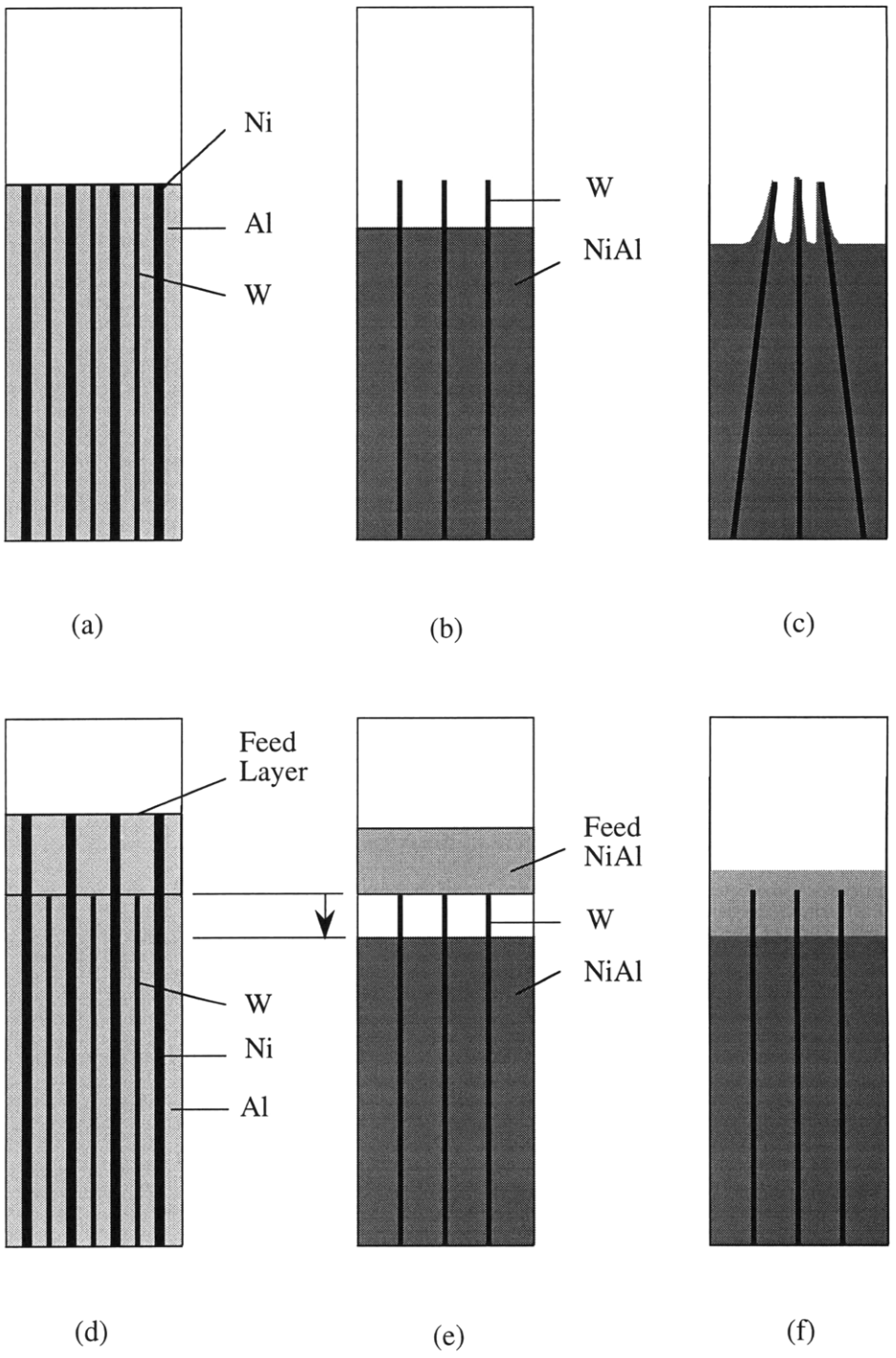

Figure 9. Schematic illustrating fiber clustering problem (a-c) and use of feed layer to solve that problem (d-f).

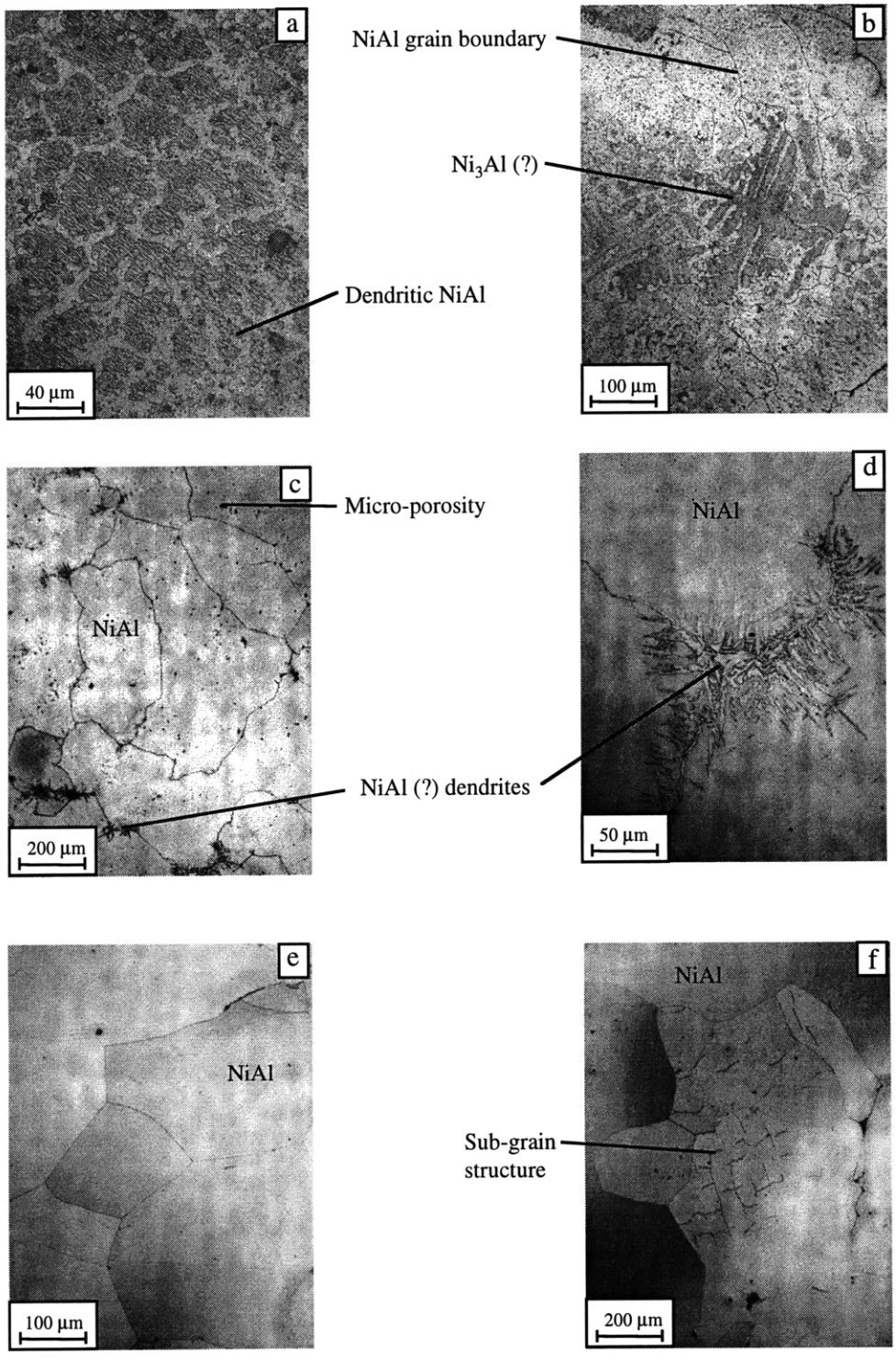

Figure 10. NiAl microstructures obtained with nickel-powder preforms A1 (a) and A2 (b) and nickel-wire preforms E1 (c, d) and E2 (e, f).

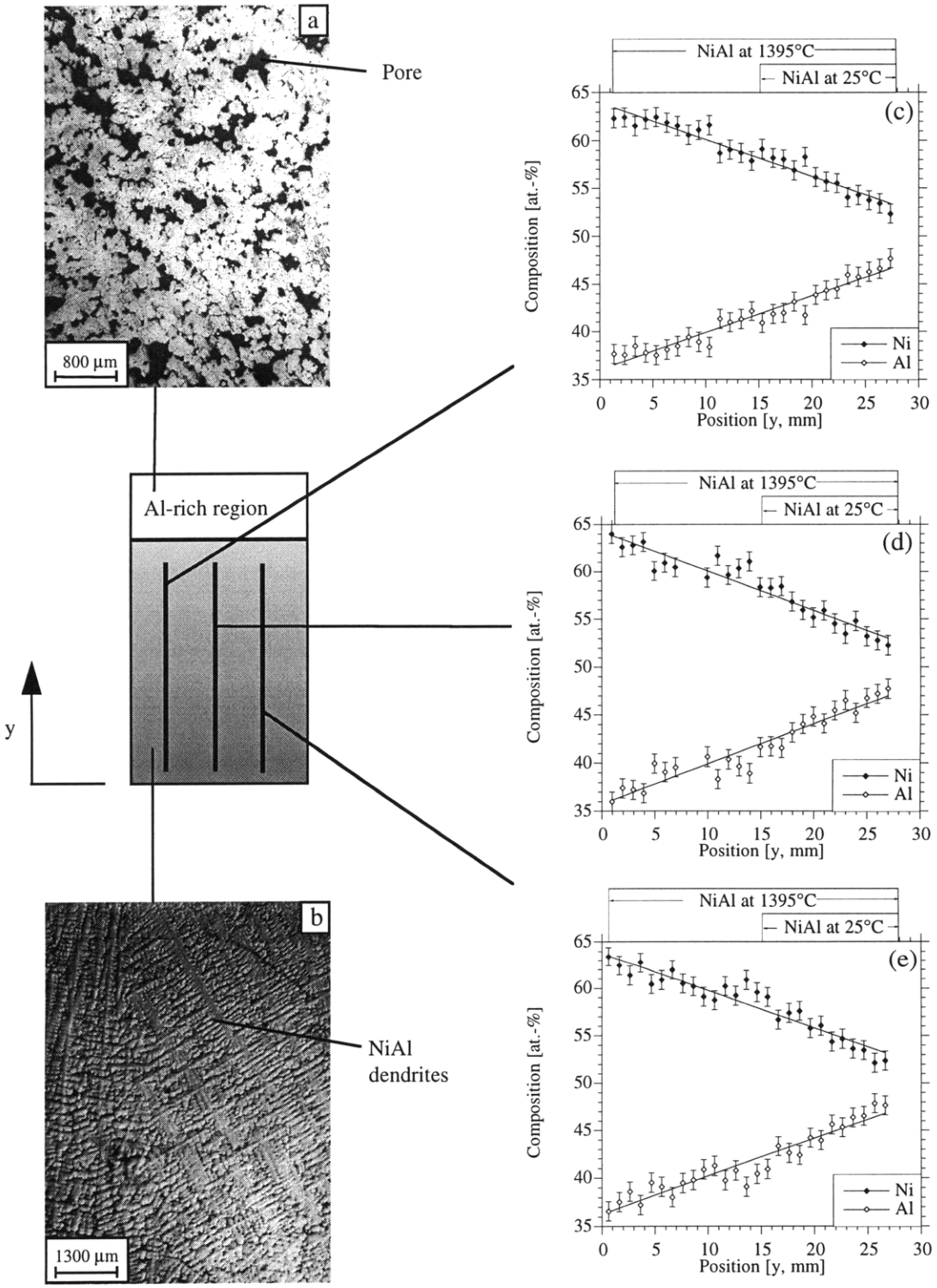

Figure 11. NiAl macrostructure (E1) with an Al-rich porous top (a), a coarse-grained and dendritic bottom (b), and composition profiles (c-e).

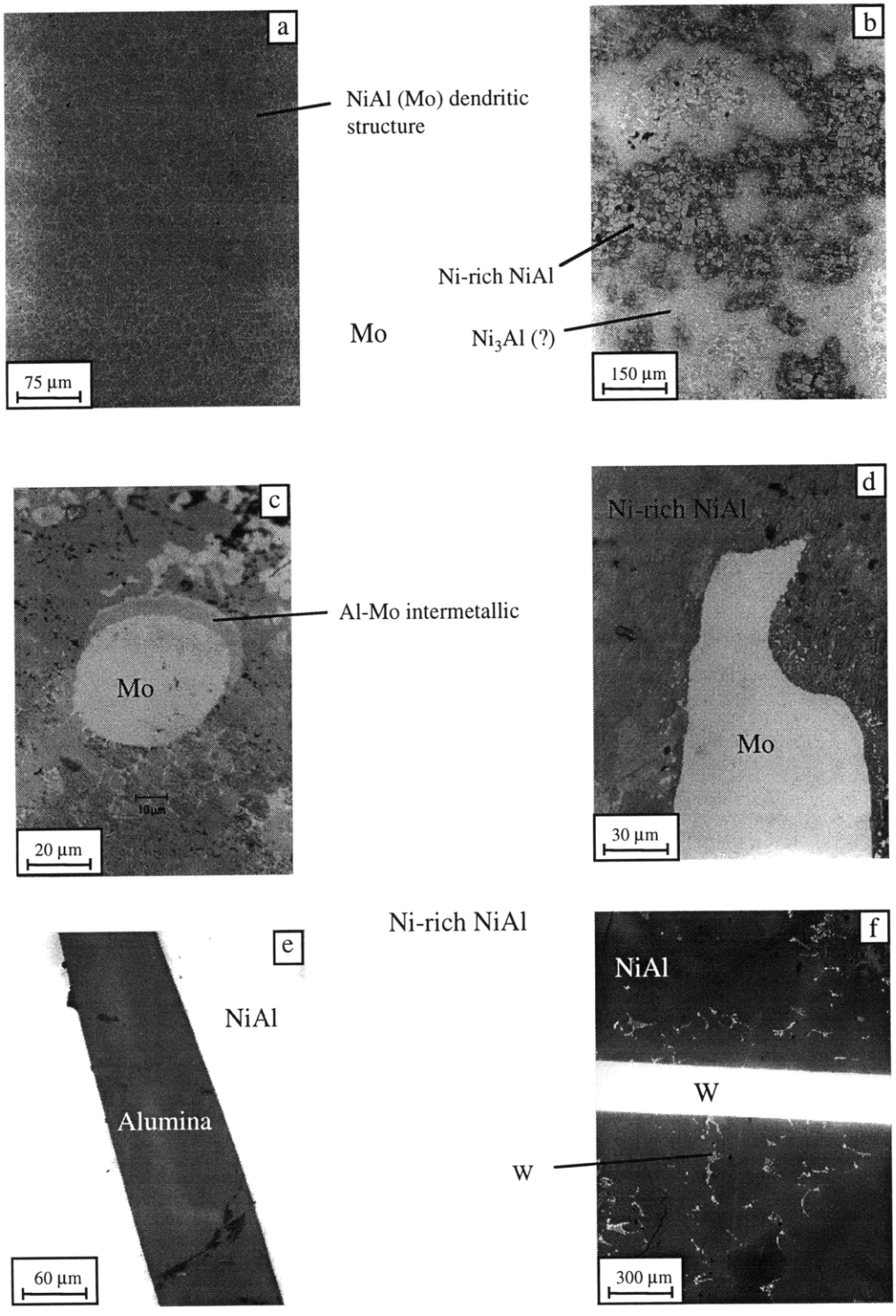

Figure 12. Optical microstructures of composites of NiAl with: (i) Mo particulates (M1) (a-b); (ii) Mo short-fibers (M3) (c-d); (iii) Alumina (G1) (e) and SEM image of NiAl-W (f) long-fiber composite (F1).

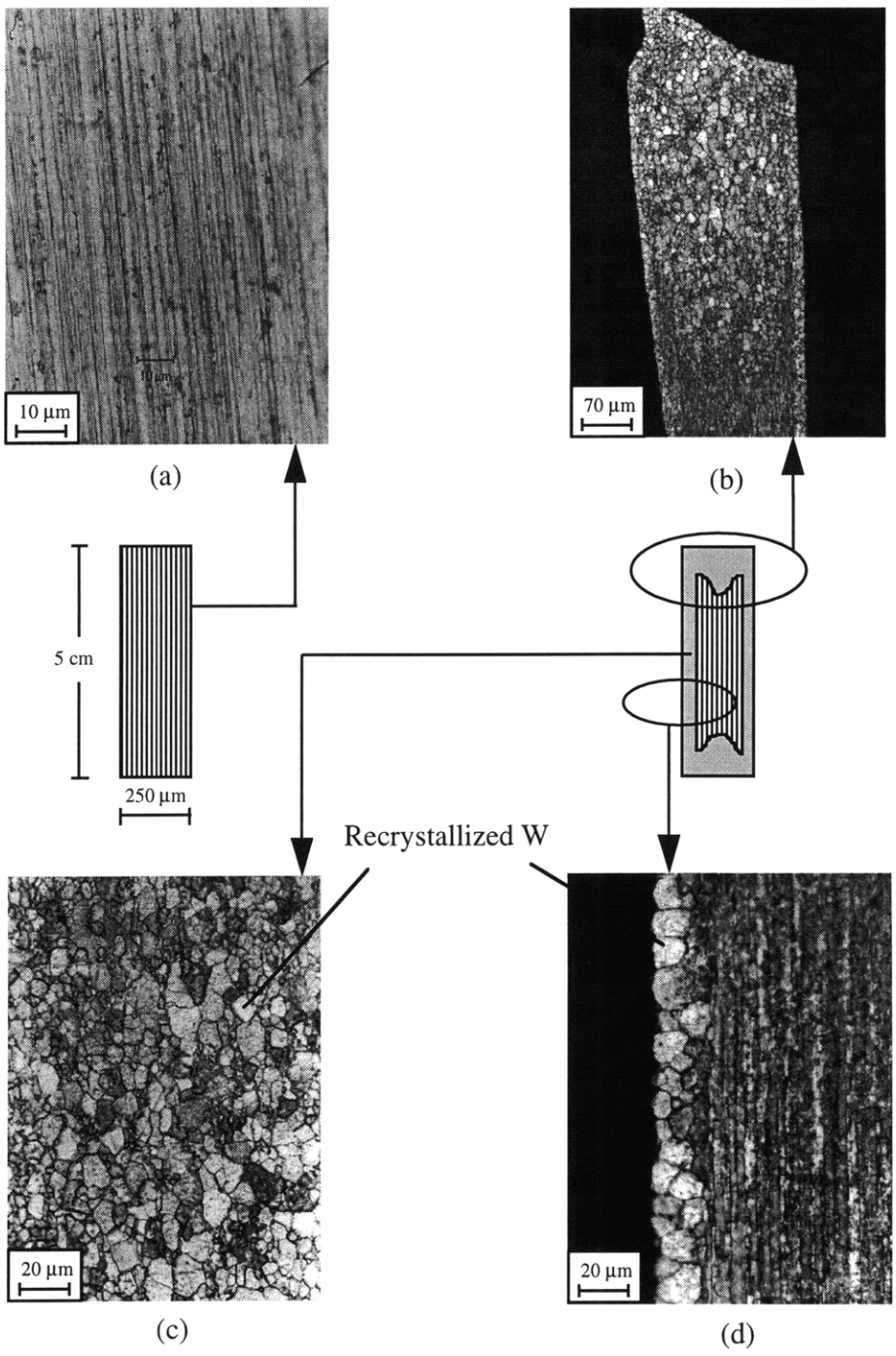

Figure 13. Optical microstructures of W in the as-received unrecrystallized state (a) and in the as-cast partially recrystallized state (b-d) (Etched in a solution of NaOH + $K_3Fe(CN)_6$ for 30 seconds).

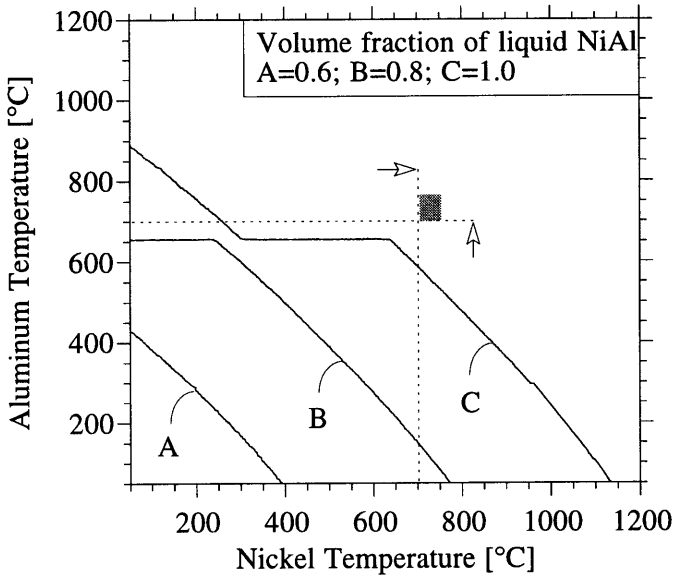

Figure 14. Thermodynamic calculations predicting volume fraction of stoichiometric liquid NiAl formed under adiabatic conditions [28].

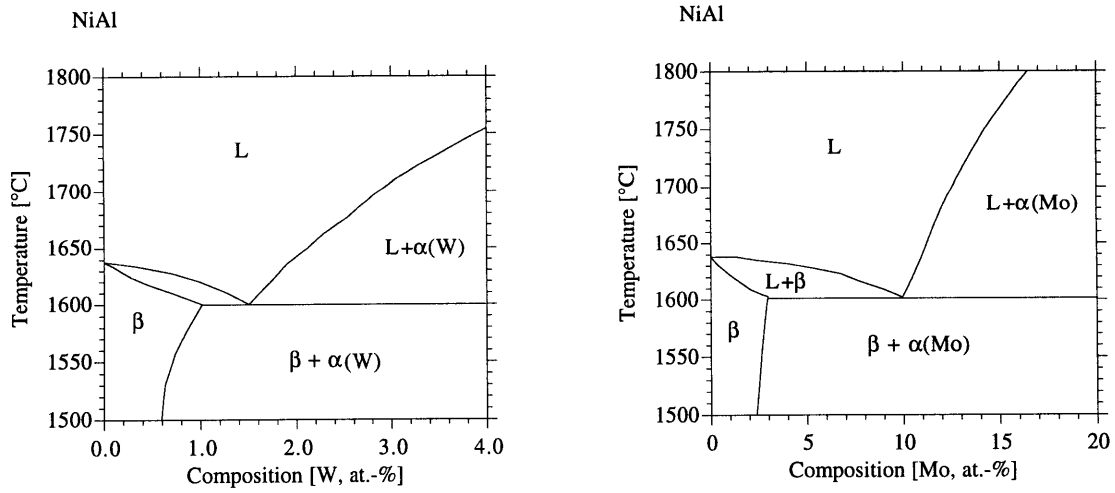

Figure 15. NiAl-Mo [33], NiAl-W [34] pseudo-binary phase diagrams showing eutectic and solubilty.

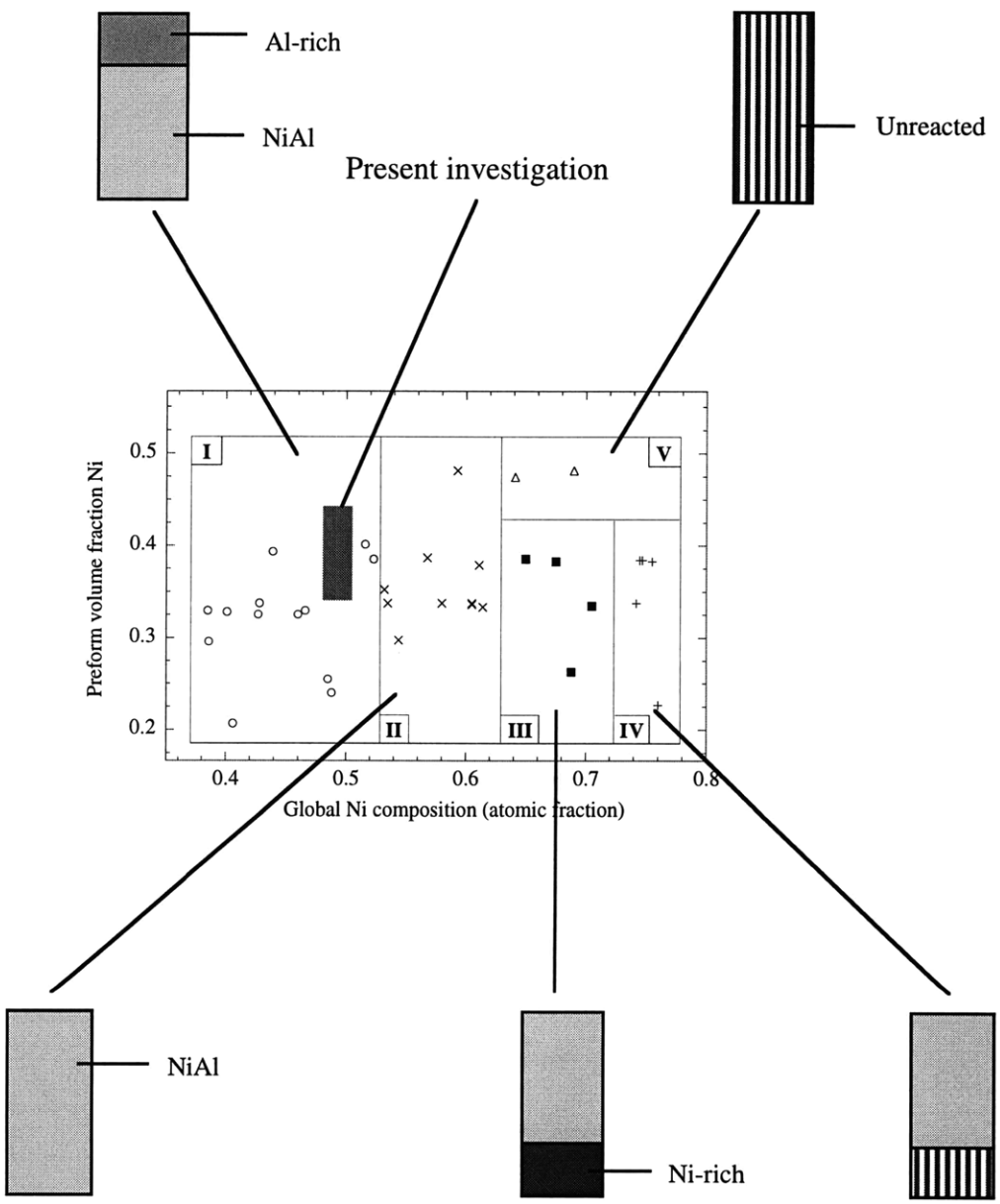

Figure 16. Processing map depicting five domains, each with its characteristic macrostructure, obtained in nickel-wire experiments [30, 31].

3 COMPRESSION CREEP OF NiAl-W COMPOSITES

3.1 Introduction

Continuous fiber metal matrix composites (MMC) have been developed with a view to obtaining high specific strength and stiffness at low and elevated temperatures. Their tensile [41] and compressive response [9, 11, 12, 14, 17] at low temperatures have been studied extensively. The composite response to tensile stresses at elevated temperatures where creep of one (i.e. the matrix) or both constituents (i.e. matrix and reinforcement) is the dominant deformation mechanism has also been modeled successfully [42, 43]. While the compressive response of these composites is expected to be qualitatively similar to their tensile response during the primary and secondary creep stages, the onset and progression of instabilities in compression is expected to be vastly different from that in tension and thus it poses a serious design limitation for composite use at elevated temperatures [44] . But a systematic study of their compressive creep behavior has not yet been undertaken.

A review of relevant literature indicates that compression creep studies, primarily experimental in nature, have been conducted on three MMC systems: NiAl-Al_2O_3 [45], Al-$CuAl_2$ [46] and $MoSi_2$-Nb [47]. The principal results of these investigations were:

- The NiAl-Al_2O_3 system was able to accommodate more than 10% in creep strain before samples failed by macrobuckling or delamination. The microstructural effects were not investigated [45]. It is quite likely that extensive fracture of alumina fibers might have contributed to the tertiary behavior.
- The eutectic Al-$CuAl_2$ system, tested under constant stress, exhibited primary, secondary and tertiary creep behavior. Microstructural evidence indicated that elastic bending and subsequent buckling of the $CuAl_2$ lamellae (approximately 7 μm in width) occurred during the secondary and tertiary creep regimes respectively [46]. No mechanical modeling was undertaken.
- The $MoSi_2$-Nb system exhibited two types of behavior. At temperatures below the brittle to ductile transition temperature (BDTT), very low failure strains were obtained as a consequence of matrix cracking. At temperatures above the BDTT, larger strains to failure were observed. No microstructural investigation of the deformed Nb fibers (800 μm in diameter) was conducted [47]. It is expected that both the Nb fibers and the $MoSi_2$ matrix would have crept under these test conditions.

As for ceramic matrix composites, one study [48] investigated creep of a SiC fiber reinforced carbon (C) composite and concluded that the composite creep was controlled by creep of the SiC fibers as a consequence of matrix failure by cracking.

Very few creep studies exist for polymer matrix composites under compression [49].

Hence the objectives of this investigation are to (i) develop simple mechanistic models to characterize the uniaxial compressive creep response of Uni-directional Continuous Fiber Reinforced Composites (UCFRC) and (ii) obtain experimental verification of these models. The high temperature mechanical behavior of a composite system can be classified into four distinct classes, depending on the dominant operative deformation mechanism of the constituents [Table 10]. The present investigation uses the NiAl-W system to study an important, yet hitherto unexplored, type of materials' behavior [Class IV, Table 10] where both the matrix (NiAl) and the fibers (W) undergo plastic deformation by creep under the action of an uniaxial compressive stress.

Table 10. Classification of compressive creep behavior for fiber reinforced composites.

		Matrix	
		Elastic	Creeping
Fiber	Elastic	Class I	Class II
		Studied extensively [9-17]	$NiAl-Al_2O_3$ [45] $Al-CuAl_2$ [46]
	Creeping	Class III	Class IV
		SiC-C [48]	NiAl-W [Present work]

3.2 Experiments

3.2.1 Materials Selection

The NiAl-W system has been chosen for this investigation for the following reasons.

- NiAl exhibits low density, high melting point, good oxidation resistance, high thermal conductivity and a wide range of compositional stability and is thus a prime candidate to replace nickel based superalloys in high-temperature structural applications [2-4]. Nevertheless the NiAl system has two major limitations [5]: (i) poor creep strength at elevated temperatures and (ii) low ductility and toughness at low temperatures, below the brittle to ductile transition temperature (BDTT).
- W offers excellent specific creep resistance at high temperatures [50-52], thus addressing the first limitation of NiAl.
- NiAl-W composite system exhibits very good chemical stability as W is thermodynamically stable with, and has virtually zero solid solubility in, NiAl [53]. NiAl protects W from oxidation, while W enhances toughness through ductile phase toughening mechanisms at low temperatures, thus addressing the second limitation of NiAl.
- Reactive infiltration, a novel processing technique, which combines the advantages of reactive synthesis synergistically with those of infiltration processing, has been developed to process NiAl and NiAl-W composites [Chapter 2].

3.2.2 Experimental Procedures

Cylindrical billets of unreinforced NiAl and NiAl reinforced with 5-20 volume % W wires were fabricated by reactive infiltration as described in § 2.2.

As-cast billets were electro-discharge-machined (Sheffield Progressive, MA) from the mid-sections of the as-cast ingots wherein the compositions were such that a single phase NiAl was expected to be predominantly present. Creep samples 10 mm and 20 mm in height and with circular and square cross-sections, 5 mm in diameter and width respectively, were thus obtained. The composite samples had fibers aligned with the longitudinal direction. Sample densities were estimated from sample mass and volume measurements using NiAl and W densities of 5.9 g/cc and 19.3 g/cc respectively.

Constant-load compression creep tests were performed in air. A superalloy (MAR M246) creep cage (Applied Test Systems, Inc., Butler, PA) translated tensile loads in the pull-rods to compressive stresses on the sample. Frictional effects on the end-loaded samples were minimized by using boron nitride coated flat alumina platens (Bomas Machine Specialty, MA) in the creep cage. (Alumina platens with a recess depth of 1 mm were also used in some experiments to prevent sample brooming.) Sample temperature was measured using one K-type thermocouple in contact with the sample and was maintained within 1°C of the set temperature through the duration of the experiment. Sample strains were calculated from extensometric displacements of the platens measured using a linear variable differential transducer (LVDT) with an accuracy of 1 μm. The creep set-up was interfaced to a computer through a data acquisition system to record displacements and temperatures.

Compression creep tests were performed on unreinforced NiAl and NiAl-W composites [Table 11] at 715°C and 1025°C within an applied stress range of 15 MPa and 300 MPa. The samples were heated to the test temperature in approximately 1 hour, soaked at the test temperature for 1 hour and then loaded gently in approximately 10 seconds.

Tension creep tests were performed on W wires in vacuum at 715°C and 1025°C within an applied stress range of 450 MPa and 1260 MPa. The W wires were wound on molybdenum threaded rods (Schwarzkopf Technology, MA) to obtain a gauge section of 100 mm and held by friction while tensile stresses where applied through superalloy (MAR M246) pull-rods. The vacuum was maintained at 1 10^{-4} torr through the duration of the experiment. The temperature was measured by one K-type thermocouple placed close to the W wire in the vacuum chamber and was maintained within 1°C of the test temperature. The samples were typically brought to the test temperature in 1 hour and soaked at the test temperature for 30 minutes and loaded gently by adding appropriate dead-weights. The creep-strains were computed by measuring the load-train displacements.

Matrix of as-cast and creep tested NiAl-W composites were dissolved in aqua-regia (3 HCl: 1 HNO_3 by volume) at room temperature for times between 4 and 8 hours. W fibers were extracted to compare fiber geometry before and after the test. From a physical count of the actual number

of W fibers recovered from each sample, the total cross-sectional area of W was determined. From a measurement of the total cross-sectional area of the composite sample prior to creep testing, the area fraction and thus the volume fraction of W in the composite sample was obtained. If the recovered W fibers had lengths shorter than the length of the creep sample, then their contribution to the overall volume fraction was suitably weighted down as well (i.e. 10 recovered fibers with length equal to 80% of the sample length, were effectively considered as 8 fibers with 100% of the sample length).

Pure W was also treated with aqua-regia to check for the effects of aqua-regia on W and it was found that there was little dissolution of W in aqua-regia.

Table 11. Experimental parameters for the compressive creep investigation of NiAl-W composites.

Experiment	Temperature [°C]	Stress [MPa]	Aspect ratio	Cross-section	Platen	W-Volume fraction [%]
Z1	715	102	2	O	F	7
Z2		205	2	O	F	7
Z3		200	2	■	F	11
Z4		300	2	■	F	11
Z5		300	2	O	F	10
Z6		300	2	O	F	6
A1f	1025	80	2	O	F	9
A2f			2	O	F	7
A3f			2	O	F	8
B1f			2	■	F	10
B2f			2	■	F	10
A1r			2	O	R	6
D1r			4	■	R	8
F1f		120	2	■	F	11
F1r			2	■	R	13
F2r			2	■	R	12
F3r			2	■	R	12
F4r			2	■	R	14
H1r			4	■	R	15
H2r			4	■	R	16
H3r			4	■	R	11

■ = Square cross-section; O = Circular cross-section; F = Flat platen; R = Recessed platen.

3.3 Results

3.3.1 Creep of NiAl

Unreinforced NiAl specimens, creep tested in compression at 715°C [Figure 17] and 1025°C [Figure 18], reached a steady-state after a very short primary stage. The steady-state strain-rate $\dot{\varepsilon}$ can be described by a power-law [Figure 19]:

$$\dot{\varepsilon} = K\sigma^n \qquad [7]$$

where σ is the stress. The experimentally determined stress exponents n and constants K are tabulated in Table 12.

Table 12. The 715°C and 1025°C power-law creep constants determined from compression and tension creep of NiAl and W respectively.

Temperature [°C]	NiAl		W	
	n	K [$MPa^{-n}\ s^{-1}$]	n	K [$MPa^{-n}\ s^{-1}$]
715	5.5	$1.74\ 10^{-18}$	13.6	$3.83\ 10^{-49}$
1025	5.6	$6.37\ 10^{-14}$	6.8	$3.48\ 10^{-26}$

The power law can also be expressed as:

$$\dot{\varepsilon} = A\exp\left[-\frac{Q}{RT}\right]\sigma^n \qquad [8]$$

where A is a constant for a given temperature which takes into account variables such as microstructure and stacking fault or antiphase boundary energy, Q is the activation energy for creep and R is the universal gas constant.

The activation energy for creep deformation of NiAl obtained by using Eq. [8] (at 50 MPa and 100 MPa) for the two temperatures 715°C and 1025°C investigated was 375 kJ/mol.

3.3.2 Creep of W

Tungsten wires creep tested in tension at 715°C [Figure 20] and 1025°C [Figure 21], reached a steady-state after a fairly pronounced primary stage, esp. at 1025°C. The steady-state strain-rate $\dot{\varepsilon}_{ss}$ can be described by a power-law [Eq. 7] [Figure 22] with the experimentally determined creep constants being listed in Table 12.

3.3.3 Creep of NiAl-W composites

NiAl-W composites exhibited two types of behavior [Table 13].

First, at 715°C, all experiments, exhibited stable steady-states over large strains on the order of 10 % [Figure 23, Figure 24]. No primary creep or tertiary creep was observed.

Second, at 1025°C, all experiments, with or without flat platens, irrespective of sample aspect ratios, exhibited visible primary creep followed by stable steady-states over varying amounts of strains and followed by a tertiary stage with a rapid increase in the strain-rates [Figure 29-Figure 34].

Upon visual inspection of the creep tested samples and the W fibers extracted from those samples, the tertiary stage was associated with four modes of fiber deformation:

1. Brooming [Figure 25] occurred in samples that had an aspect-ratio of 2 and were tested using flat platens.
2. Bulging [Figure 26] occurred predominantly in samples that had an aspect-ratio of 2 and tested using recessed platens.
3. Buckling [Figure 27] occurred in sample A2f.
4. Kinking [Figure 28] occurred only in samples that had an aspect-ratio of 4 and tested using recessed platens.

3.3.4 Volume fraction of W

When compared to the volume fraction of W present in the samples prior to creep-testing [Table 13], there was a clear indication of loss of W upon exposure to air at 715°C and 1025°C. A visual inspection of the creep tested samples confirmed heavy oxidation of W with an yellow-green oxide of tungsten found curling out of the sample surface. It was also determined from trial experiments that almost all of the oxidation occurred during the heating and soaking stage prior to the application of loads to the samples. Thus it is believed that there was no change in the W volume fraction during the actual creep-tests. Since the actual amount of W present at the sample surface varied across the different samples, the loss of W also varied across samples, thus explaining the variations in W loss across different samples.

Table 13. The 715°C and 1025°C compression creep test results of NiAl-W composites.

Expt.	T [°C]	Stress [MPa]	$[v_f]b$ [%]	$[v_f]a$ [%]	ε_p [%]	t_p [hour]	ε_{ss} [s^{-1}]	ε_t [%]	ε_{total} [%]	t_{total} [hour]	Tertiary type
Z1	715	102	11	7	-	-	$4.4\ 10^{-9}$	-	0.5	210	None
Z2		205	11	7	-	-	$1.0\ 10^{-7}$	-	0.6	85	
Z3		200	14	11	-	-	$1.1\ 10^{-8}$	-	3.2	120	
Z4		300	14	11	-	-	$8.2\ 10^{-7}$	-	3.5	11.5	
Z5			13	10	-	-	$4.1\ 10^{-6}$	-	10.0	8.5	
Z6			11	6	-	-	$6.8\ 10^{-6}$	-	13.0	7.3	
A1f	1025	80	14	9	1.0	5.0	$2.0\ 10^{-7}$	3.5	18.0	64	Brooming
A2f			11	7	1.5	1.0	$1.3\ 10^{-6}$	3.5	9.0	10	Buckling
A3f			14	8	1.3	2.0	$4.9\ 10^{-7}$	5.0	11.0	28	Brooming
B1f			15	10	1.5	5.0	$3.0\ 10^{-7}$	8.0	15.0	163	Brooming
B2f			15	10	3.5	16.0	$4.6\ 10^{-7}$	7.0	18.0	83	Brooming
A1r			10	6	1.0	0.5	$1.6\ 10^{-6}$	3.0	19.0	21	Bulging
D1r			9	8	2.5	25.0	$1.5\ 10^{-7}$	10.5	13.5	410	Bulging
F1f		120	15	11	1.3	0.1	$2.1\ 10^{-5}$	5.5	10.3	1.3	Kinking
F1r			17	13	1.5	7.0	$3.5\ 10^{-7}$	5.5	19.0	94	Bulging
F2r			16	12	1.0	1.0	$9.6\ 10^{-7}$	4.0	2.5	16.4	Incipient
F3r			15	12	6.0	1.0	$1.8\ 10^{-5}$	10.0	14.0	2.7	Brooming
F4r			19	14	1.3	2.0	$7.6\ 10^{-7}$	2.0	2.4	6.4	Incipient
H1r			18	15	1.3	3.0	$6.4\ 10^{-7}$	3.5	14.0	17	Kinking
H2r			17	16	1.0	1.5	$3.5\ 10^{-7}$	3.0	14.0	32	Kinking
H3r			13	11	3.5	5.0	$8.0\ 10^{-7}$	6.0	13.5	29	Brooming

ε_p=primary creep strain; t_p=primary time; ε_{ss}=steady-state creep-rate; ε_t=threshold strain for onset of tertiary creep; ε_{total}=total creep strain accumulated; $[v_f]b$=volume fraction of W before creep-test; $[v_f]a$=volume fraction after creep testing; t_{total}=total time of creep test.

3.3.5 Figures and Illustrations

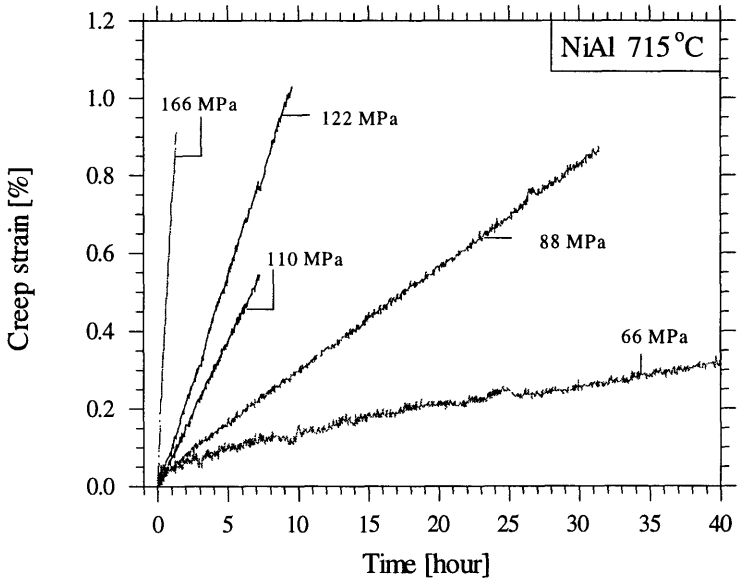

Figure 17. Compression creep of reactively processed monolithic NiAl at 715°C at different stresses.

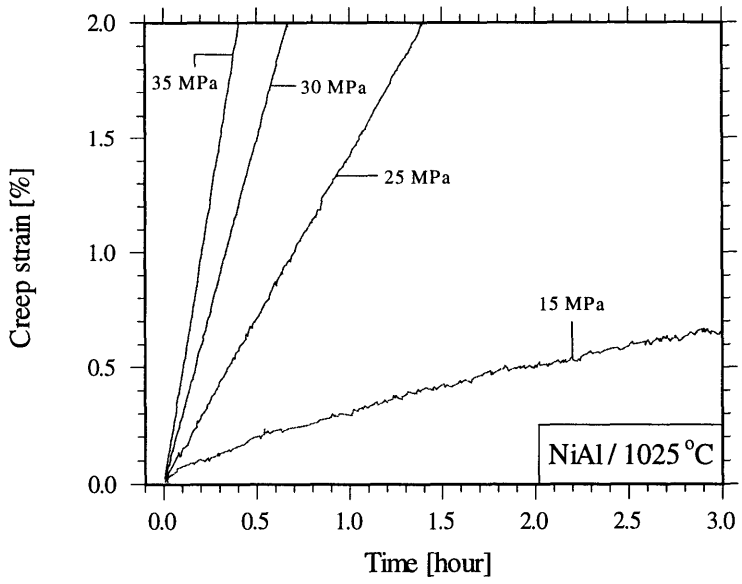

Figure 18. Compression creep of reactively processed monolithic NiAl at 1025°C at different stresses.

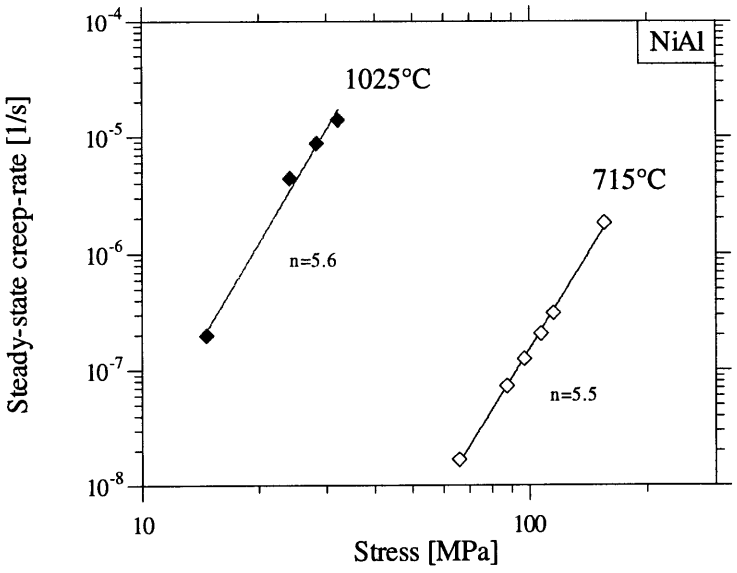

Figure 19. Experimentally obtained steady-state creep-rates of NiAl at 715°C and 1025°C exhibiting power-law behavior.

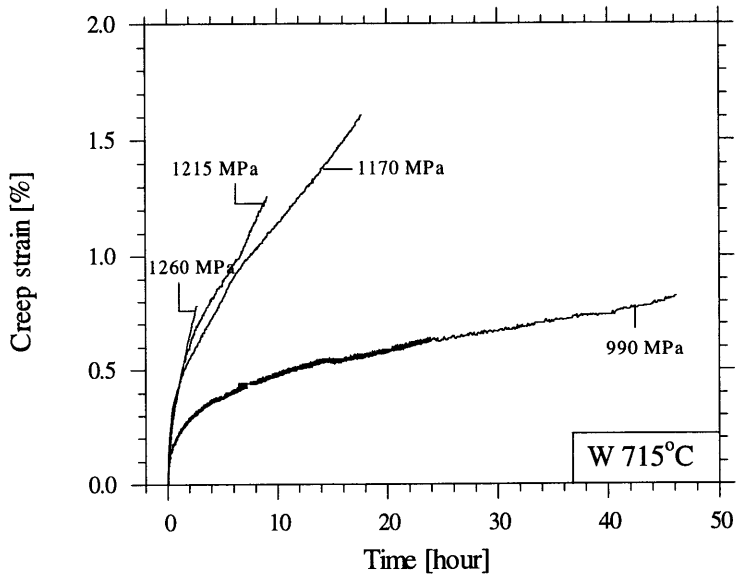

Figure 20. Tension creep of unrecrystallized W wires at 715°C at different stresses.

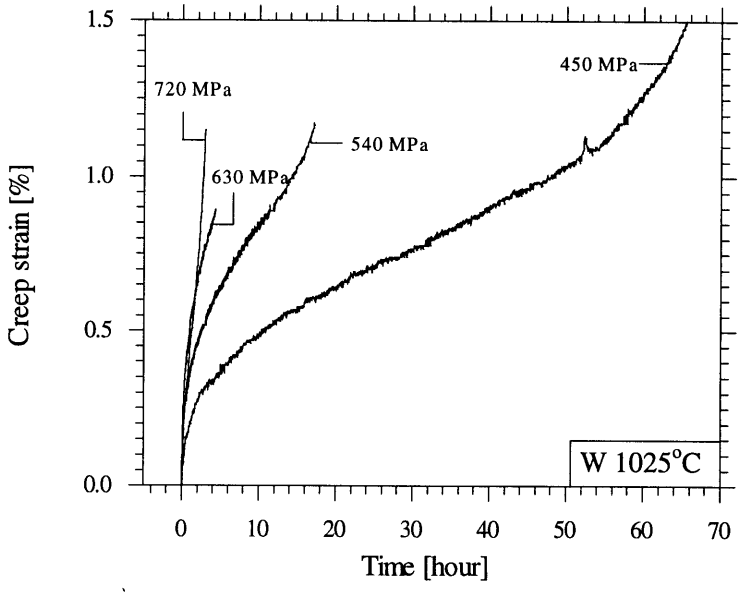

Figure 21. Tension creep of unrecrystallized W wires at 1025°C at different stresses.

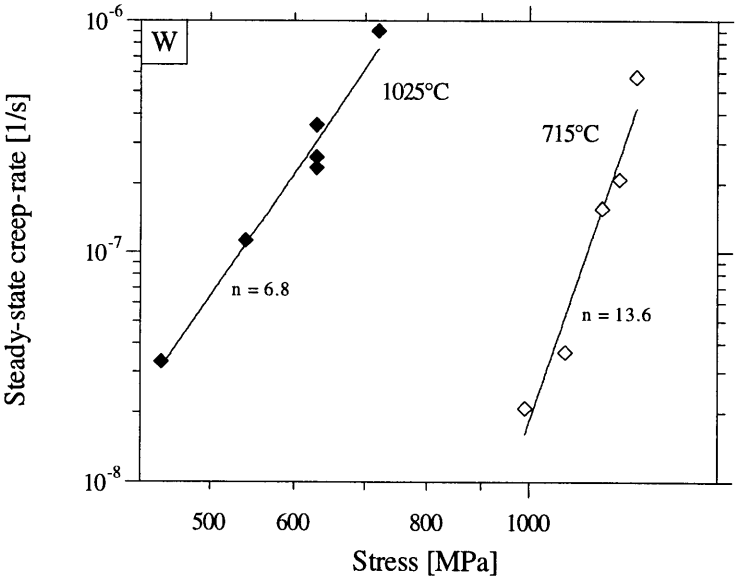

Figure 22. Experimentally obtained steady-state creep rates of unrecrystallized W wires at 715°C and 1025°C demonstrating power-law behavior.

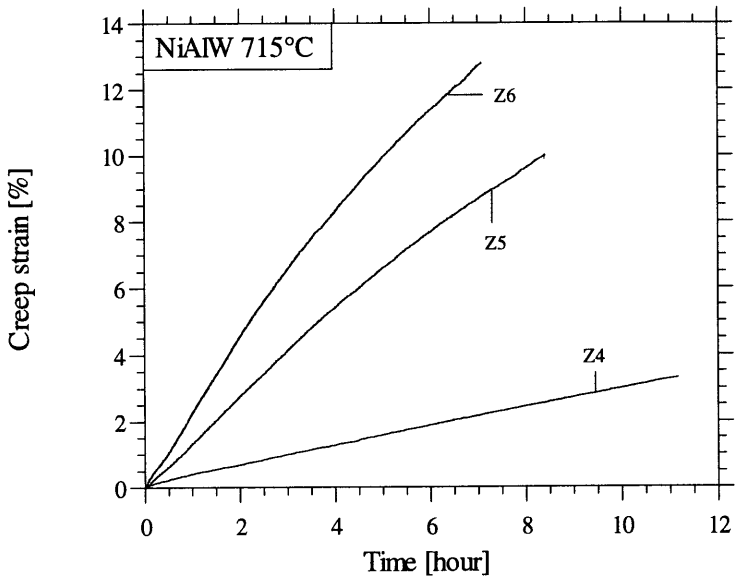

Figure 23. 715°C creep of NiAl-W composites with different volume fractions of W, at an applied composite stress of 300 MPa.

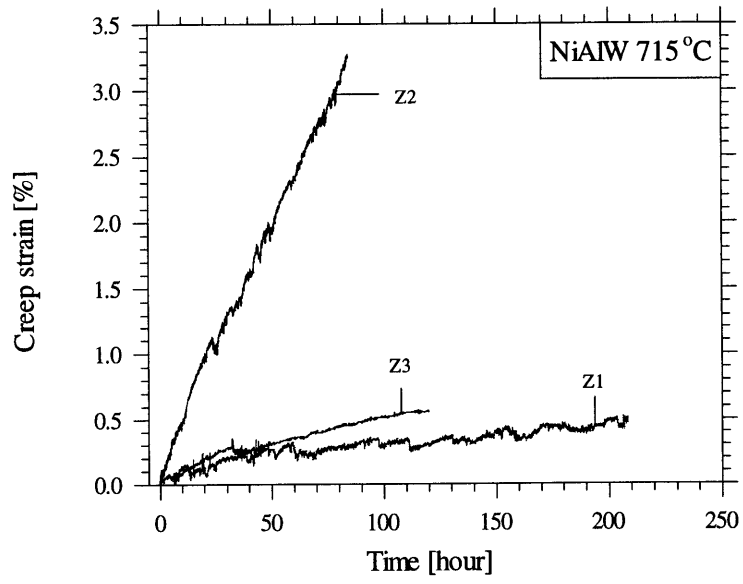

Figure 24. 715°C creep of NiAl-W composites under varying stresses (Z1 = 102 MPa, Z2 = 205 MPa, Z3 = 200 MPa) and with different volume fractions of W.

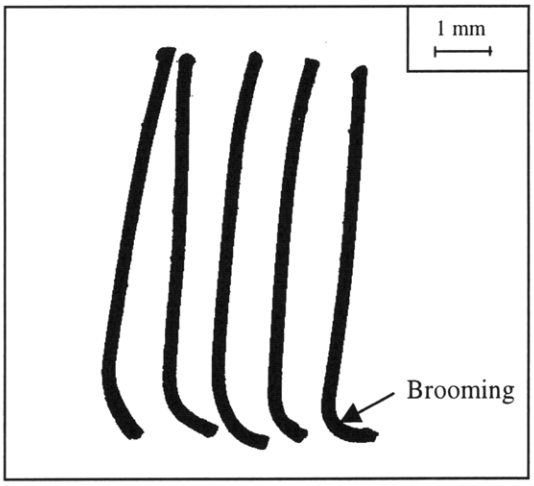

Figure 25. NiAl-W composite (B2f) exhibiting tertiary behavior by fiber brooming at 1025°C.

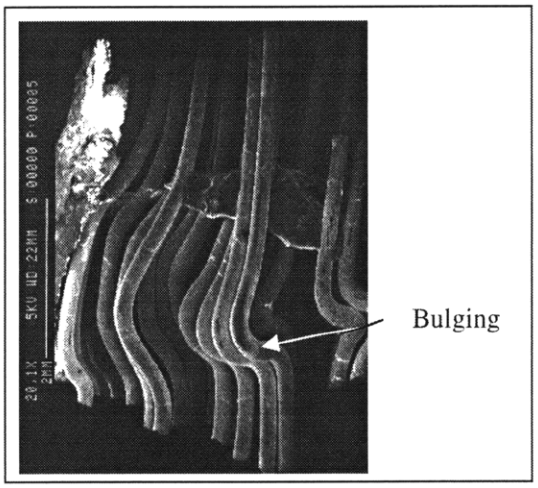

Figure 26. NiAl-W composite (F1r) exhibiting tertiary behavior by fiber bulging at 1025°C.

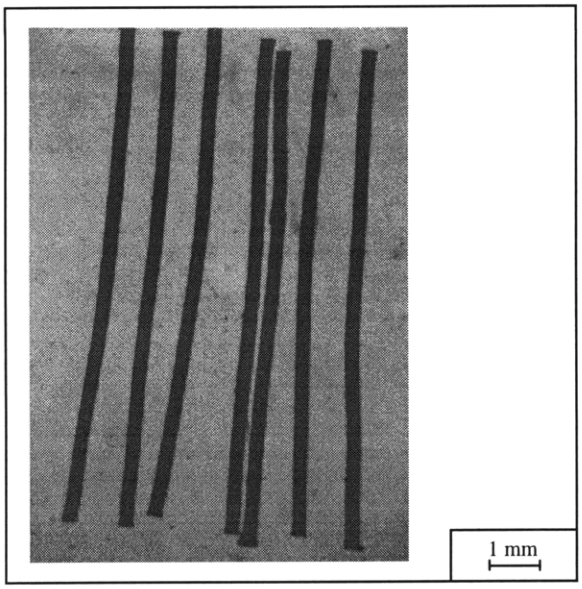

Figure 27. NiAl-W composite (A2f) exhibiting tertiary behavior by fiber buckling at 1025°C.

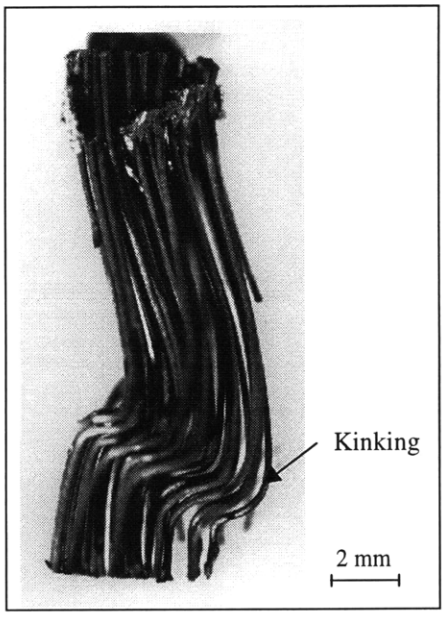

Figure 28. NiAl-W composite (H2r) exhibiting tertiary behavior by fiber kinking at 1025°C.

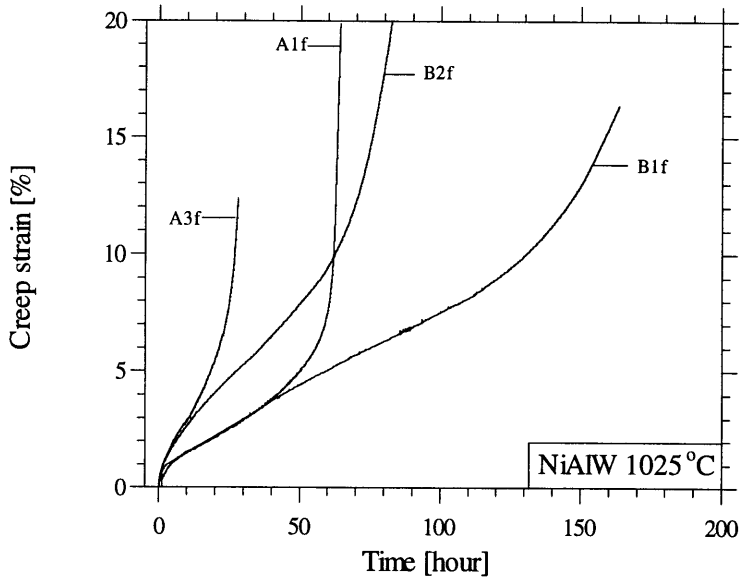

Figure 29. 1025°C NiAl-W composite creep exhibiting tertiary by brooming at 80 MPa.

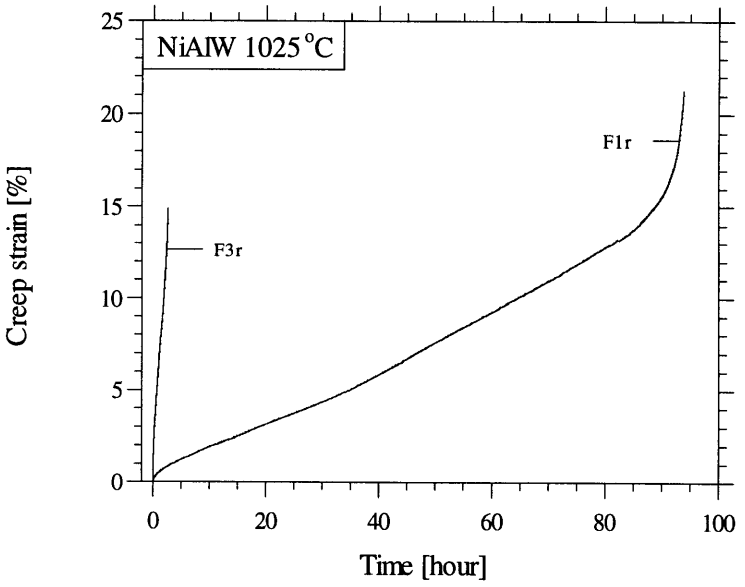

Figure 30. 1025°C NiAl-W composite creep exhibiting tertiary by bulging (F1r) and brooming (F3r) at 120 MPa.

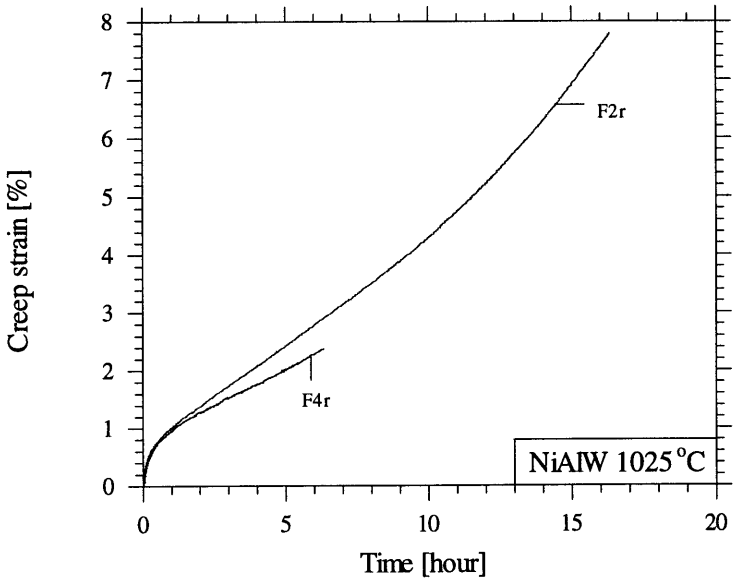

Figure 31. 1025°C NiAl-W composite creep exhibiting incipient tertiary at 120 MPa.

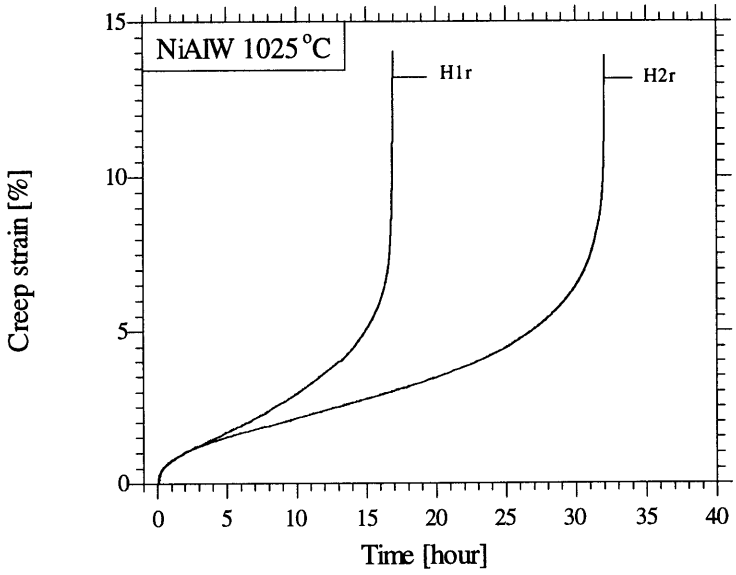

Figure 32. 1025°C NiAl-W composite creep exhibiting tertiary by kinking under 120 MPa.

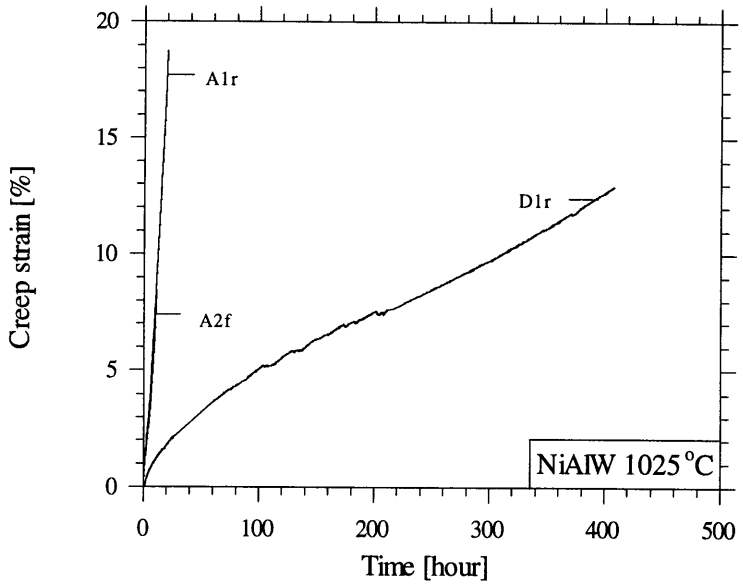

Figure 33. 1025°C NiAl-W creep exhibiting tertiary by bulging (A1r, D1r) and partial buckling (A2f) at 80 MPa.

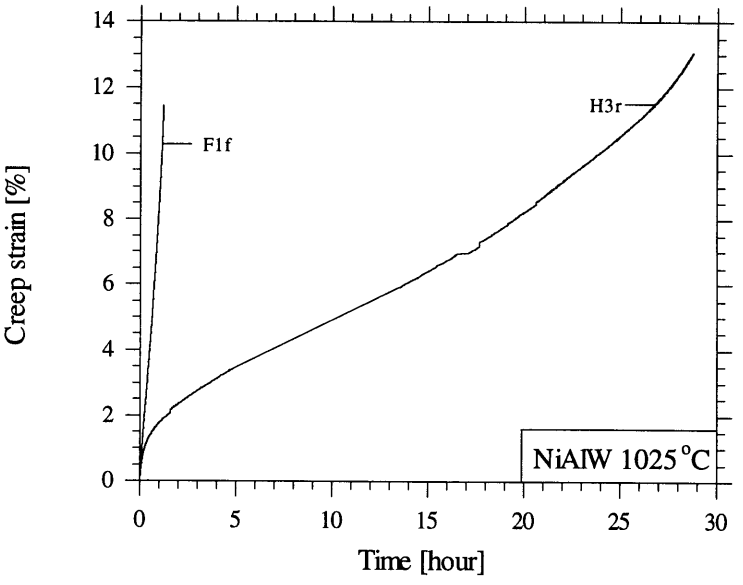

Figure 34. 1025°C NiAl-W creep exhibiting tertiary by partial kinking (F1f) and brooming (H3r) at 120 MPa.

3.4 Discussion

3.4.1 Creep of NiAl

It is fairly well established that creep of NiAl is typically governed by dislocation creep mechanisms for the temperatures, stresses, and grain-sizes investigated [3]. For single phase metals and alloys, dislocation creep can be classified as either of two main types, known as class M, or pure metal type, and class A, or alloy type. Class M creep is characterized by glide being much faster than climb, and thus creep becomes controlled by the rate of climb past substructural obstacles. Class A creep is characterized by climb being much faster than glide and thus creep becomes controlled by the rate of glide past solute atoms or glide against the high lattice-friction stress resulting from long-range order. These two types of behavior can be distinguished by several criteria including stress exponent, the shape of the primary creep curve, dislocation substructure, and the response of the material to stress or strain-rate transients.

A summary of the stress exponents and activation energies reported in literature have been reviewed by Noebe [3] and are presented in Table 14.

Table 14. Summary of NiAl creep parameters obtained by other researchers [3].

Composition [Al – at. %]	Grain-size [μm]	Temperature [°C]	n	Q [kJ mol^{-1}]
48.25	5-9	727-1127	6.0-7.5	313
44-50.6	15-20	827-1127	5.75	314
50	12	927-1027	6	350
50	450	800-1045	10.2-4.6	283
50	500	900	4.7	-
50.4	1000	802-1477	7.0-3.3	230-290
50	Single crystal [123]	750-950	7.7-5.4	-
50	Single crystal [001]	727-1027	6	440

For NiAl the average value for the activation energy for creep is ~ 314 kJ mol^{-1}. Examination of the stress exponents of NiAl having a wide variety of grain-sizes, including single crystals, reveals that between 827°C and 1127°C, the values of n cluster between 5 and 7 and all experimental evidence point toward the high temperature creep of NiAl to be dislocation climb-controlled.

It has also been observed that a number of factors such as presence of impurities, interstitials, oxide inclusions, and changes in composition can affect the steady-state creep-rate at a given stress by one or even two orders of magnitude [2].

The steady-state strain-rates observed at 1025°C is quite consistent with literature values while at 715°C, the NiAl obtained from reactive infiltration exhibits creep properties better than that

reported in the literature [Figure 35]. As discussed above this could be due to the differences in the levels of impurities and grain-sizes of NiAl used by different researchers.

The stress exponents of 5.5 and 5.6 [Table 12] obtained in this investigation are thus quite consistent with established theory on creep of NiAl, while the activation energy of 375 kJ/mol obtained in this investigation is higher than that reported for polycrystalline NiAl (283-350 kJ/mol) but lower than that reported for single crystal NiAl (440 kJ/mol). The activation energy computed here is obtained by considering only two temperatures and thus constitutes an approximation of the true activation energy of the system.

3.4.2 Creep of W

The tension creep curves of W exhibit primary, secondary, and tertiary stages.

The primary stage is more pronounced at 1025°C. The total creep-strain accumulated in the primary stage, at 1025°C [Figure 36] can be modeled as follows:

$$\varepsilon_f = \dot{\varepsilon}_{ss} t + q t^{1/3} \qquad [9]$$

where $\dot{\varepsilon}_{ss}$ is the steady-state creep-rate and q is a constant that varies with the applied stress [Table 15].

Table 15. The experimentally determined 1025°C primary creep parameters of W.

Stress [MPa]	q [$s^{-1/3}$]	Chisq	R
450	$1.1\ 10^{-4}$	$9.2\ 10^{-5}$	0.97
540	$1.8\ 10^{-4}$	$2.2\ 10^{-4}$	0.97
630	$2.7\ 10^{-4}$	$7.8\ 10^{-5}$	0.96

The observed steady-state creep-rates of W at 715°C are lower than those at 1025°C as expected. The stress exponents vary sharply from 13.6 at 715°C to 6.7 at 1025°C most likely indicative of a change in the deformation mechanism for creep or a transition from a time-independent elasto-plastic deformation to time-dependent plastic deformation by creep across this temperature range for the stress range considered. The Frost and Ashby maps [54] predict W deformation to conform to the low-temperature power-law region.

The steady-state creep-rates of unrecrystallized W wires are many orders of magnitude lower than those obtained for recrystallized W [51] [Figure 37]. This is most likely due to the fact that the wire drawing process induces a textured microstructure with narrow elongated grains with a very high density of dislocations and dislocation tangles. This severely impedes dislocation motion causing the creep strength of W to increase by several orders of magnitude. The actual extent of strengthening that could be induced by the wire-drawing process was investigated by Harris and Ellison using 76 μm diameter drawn and unrecrystallized W wires [52] [Figure 38].

The steady-state creep-rates of unrecrystallized W with diameter of 250 μm, obtained in this investigation appear to correlate reasonably well with the steady-state creep-rates obtained by Harris and Ellison.

Recrystallization of W can be driven by thermal and/or chemical effects. In the NiAl-W composites processed by reactive infiltration, the W fibers are exposed to high temperatures (approximately 1638°C). This induces the transformation of the high energy, highly textured wire-drawn microstructure to a lower energy untextured recrystallized microstructure. As the W fibers are exposed to high temperatures only for a short time, only parts of the W fiber are recrystallized as discussed in § 2.4. It has been demonstrated that there is limited solid solubility (0.5 at. %) of Ni in W [55] while there is a substantial solid solubility (12 at. %) of Al in W [56]. Diffusion of Ni or Al into W is expected to enhance the recrystallization of W primarily by reducing the recrystallization temperature of W [6]. In the intermetallic NiAl, which does exhibit considerable off-stoichiometry, Ni and Al are tightly bound to one-another, and exposed to high-temperatures only for a few seconds. Consequently only limited amount of diffusion of Ni or Al into W is expected. Comparison of the untested and creep-tested microstructures of W fibers indicate little difference in the size of the recrystallized zone indicating little diffusion of Ni or Al into W at test temperatures (715°C and 1025°C). Thus it is concluded that the recrystallization of W is predominantly influenced by the thermal effects of the reactive infiltration process.

As recrystallization embrittles W, the partially recrystallized W fibers in the NiAl-W composite are expected to contribute less towards enhancing the low temperature toughness of the NiAl-W composite.

3.4.3 Figures and Illustrations

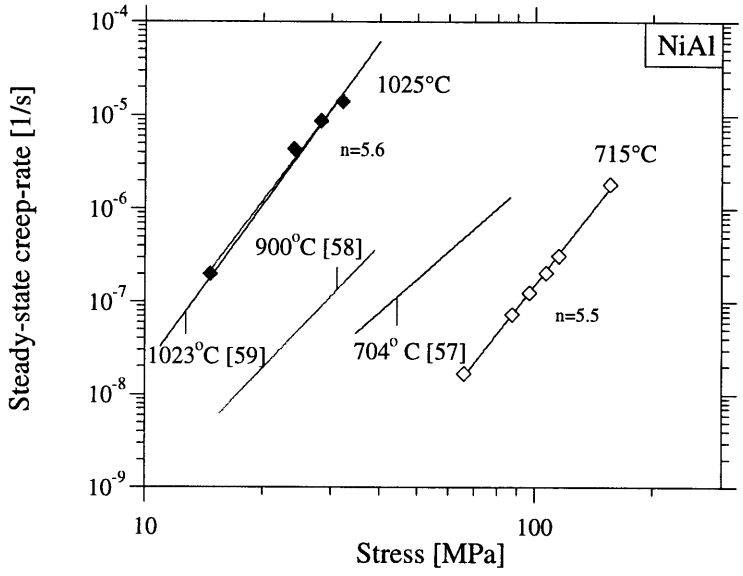

Figure 35. Steady-state creep-rates of NiAl produced by reactive infiltration [present investigation] compared to conventional as-cast NiAl [57-59].

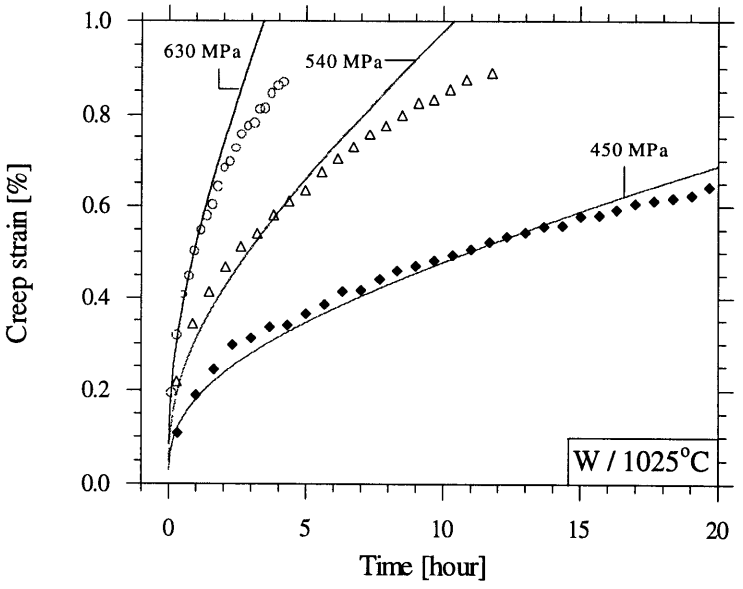

Figure 36. 1025°C W primary creep modeled using Andrade time law with an exponent = 1/3.

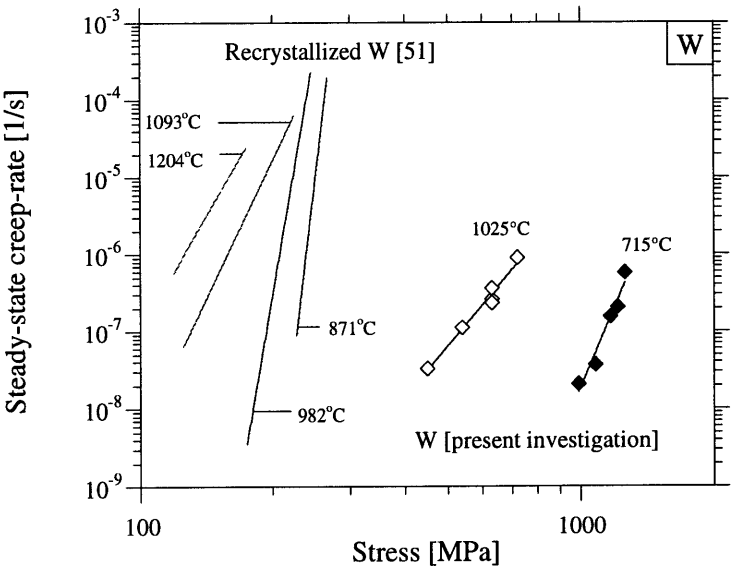

Figure 37. Steady-state creep-rates of W-wires [present investigation] compared to those of recrystallized W [51].

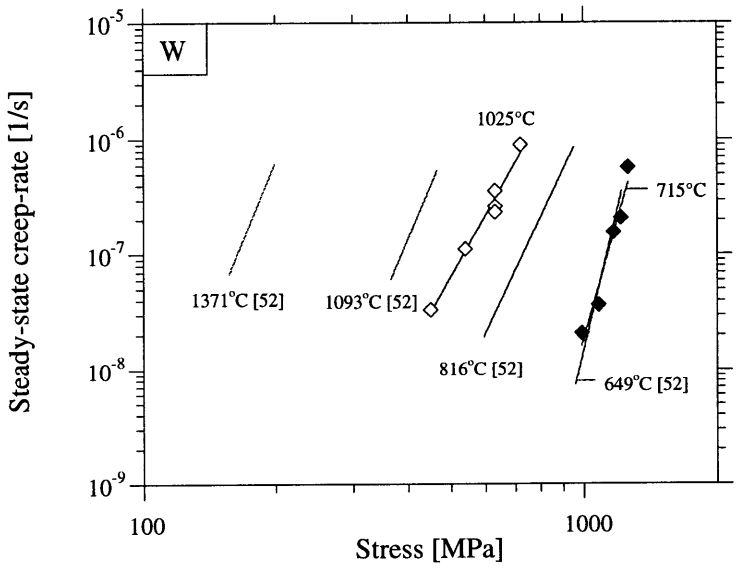

Figure 38. Steady-state creep-rates of W-wires (250 μm diameter) [present investigation] compared to those of W-wires (76 μm diameter) [52].

3.4.4 Creep of NiAl-W composites

3.4.4.1 Primary creep

3.4.4.1.1 Model

The instantaneous elastic/elasto-plastic response as well as long-term creep relaxation behavior of UCFRC systems loaded in uniaxial compression [Figure 39a] is modeled using a simple one-dimensional spring-dashpot model [Figure 39b]. The model developed here for uni-axial compression is equally valid for uniaxial tension. The springs and the dash-pots capture the elastic and creep responses of the constituent phases respectively.

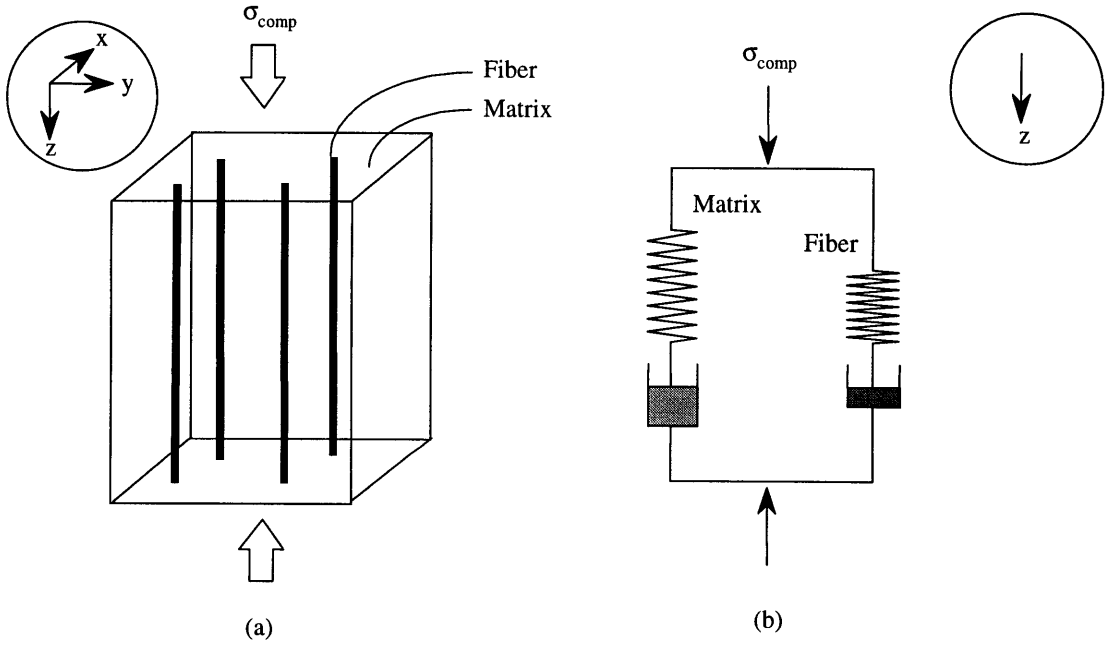

Figure 39. Schematic of primary creep model.

3.4.4.1.1.1 Model assumptions

1. This one-dimensional model assumes in-plane material behavior (i.e. in 'yz' plane) to be representative of the bulk behavior of the composite.
2. Perfect bonding between fiber and the matrix is assumed and hence no slippage takes place. Thus strain compatibility is maintained at all times during deformation.

3. The constituents are expected to be in a stress-free state prior to loading. Hence residual stresses are not introduced.
4. Fibers are modeled as being perfectly straight with no imperfections. Hence they are under pure compression and no bending moments are introduced into the system.
5. Systems have low volume fractions of reinforcements and hence inter-fiber interactions can safely be ignored and thus the unit cell in this model has one fiber only.
6. No end effects are introduced and hence only bulk behavior is modeled.
7. Creep experiments indicate that the primary regime in NiAl is insignificant [§ 3.3.1]. Hence matrix primary is ignored.
8. Creep experiments indicate that the primary regime in W is fairly significant esp. at 1025°C [§ 3.3.2]. Hence fiber primary is taken into account.
9. The elastic and plastic Poisson's ratios of both the constituents have been taken to be identical.

3.4.4.1.1.2 Initial conditions

The model is set-up such that at t=0 upon loading, the instantaneous elastic solutions for fiber and matrix stresses is obtained.

Table 16. List of symbols used in the development of the primary creep model.

Symbol	Parameter
σ	stress
ε	strain
t	time
$\dot{\sigma}$	$d\sigma/dt$ - instantaneous stress-rate
$\dot{\varepsilon}$	$d\varepsilon/dt$ - instantaneous strain-rate
$[\dot{\varepsilon}]_{ss}$	steady-state strain-rate
v	volume fraction
E	Young's modulus
subscripts 'm', 'f', and 'comp'	matrix, fiber, and composite respectively

3.4.4.1.1.3 Boundary conditions

At very long times when t tends to infinity, the composite creep-rate is expected to converge to the corresponding McLean steady-state creep-rate $\dot{\varepsilon}_{ss}$ at a composite stress σ_{comp} as:

$$\sigma_{comp} = v_f \left[\frac{\dot{\varepsilon}_{ss}}{K_f}\right]^{1/n_f} + \left[1 - v_f\right]\left[\frac{\dot{\varepsilon}_{ss}}{K_m}\right]^{1/n_m} \qquad [10]$$

The steady-state fiber and matrix stresses are then given as:

$$\sigma_f\big|_{ss} = \left[\frac{\dot{\varepsilon}_{ss}}{K_f}\right]^{1/n_f} \quad [11]$$

$$\sigma_m\big|_{ss} = \left[\frac{\dot{\varepsilon}_{ss}}{K_m}\right]^{1/n_m} \quad [12]$$

3.4.4.1.1.4 Model derivation

Upon applying a compressive stress to the composite, the matrix and fiber stresses, at all times, are governed by the rule of mixtures relation as discussed by McLean [42]:

$$\sigma_{comp} = v_f\sigma_f + v_m\sigma_m \quad [13]$$

where:

$$v_m = 1 - v_f \quad [14]$$

For a constant stress experiment wherein the composite stress remains invariant with time, Eqs. [13, 14] yield:

$$\dot{\sigma}_m = -\left[\frac{v_f}{v_m}\right]\dot{\sigma}_f \quad [15]$$

The steady-state creep-rates of the matrix and the fiber follow power-law behavior with stress-exponents n_m and n_f respectively:

$$\left[\dot{\varepsilon}_m\right]_{ss} = K_m\left[\sigma_m\right]^{n_m} \quad [16]$$

$$\left[\dot{\varepsilon}_f\right]_{ss} = K_f\left[\sigma_f\right]^{n_f} \quad [17]$$

where K is a constant that accounts for microstructural effects and activation energies for creep deformation. The strain and strain-rate compatibility between the matrix and fiber dictate:

$$\varepsilon_m = \varepsilon_f = \varepsilon_{comp} \quad [18]$$

$$\dot{\varepsilon}_m = \dot{\varepsilon}_f = \dot{\varepsilon}_{comp} \quad [19]$$

At any given time 't', the total strain in the matrix and fiber is decoupled into their respective elastic and plastic components as follows:

$$\varepsilon_m = \varepsilon_m^{elastic} + \varepsilon_m^{plastic} \quad [20]$$

wherein the plastic component has contributions from the primary and secondary creep regimes:

$$\varepsilon_m^{plastic} = \varepsilon_m^{primary} + \varepsilon_m^{secondary} \quad [21]$$

The elastic strain is given by Hooke's law:

$$\varepsilon_m^{elastic} = \frac{\sigma_m}{E_m} \quad [22]$$

The primary creep contribution to the matrix plastic strain can be modeled using Andrade time law with an exponent of 1/3:

$$\varepsilon_m^{primary}\Big|_{\sigma=constant} = q_m t^{1/3} \quad [23]$$

where q_m is taken as a constant that exhibits a linear dependence with stress:

$$q = q_{0m} + q_{1m}\sigma_m \quad [24]$$

wherein the constants q_{om} and q_{1m} are determined from experiments.

From Eqs. [23, 24], the total primary creep strain that accumulates under conditions of varying stresses is computed as:

$$\varepsilon_m^{primary} = \int_0^t \frac{1}{3}\left[q_{om} + q_{1m}\sigma_m\right] t^{-2/3} dt \quad [25]$$

The secondary creep contribution to the matrix plastic strain is obtained by integration of Eq. [16]:

$$\varepsilon_m^{secondary} = \int_0^t K_m\left[\sigma_m\right]^{n_m} dt \quad [26]$$

Similarly, the fiber strain is described by:

$$\varepsilon_f = \varepsilon_f^{elastic} + \varepsilon_f^{plastic} \quad [27]$$

$$\varepsilon_f^{plastic} = \varepsilon_f^{primary} + \varepsilon_f^{secondary} \quad [28]$$

$$\varepsilon_f^{elastic} = \frac{\sigma_f}{E_f} \quad [29]$$

The constant stress primary creep strain in the fiber is also modeled using Andrade time law with an exponent of 1/3:

$$\varepsilon_f^{primary}\Big|_{\sigma=constant} = q_f t^{1/3} \quad [30]$$

where q_f is a function of stress and has been experimentally determined [§ 3.4.2] to vary as:

$$q = q_{0f} + q_{1f}\sigma_f \quad [31]$$

with q_{0f} and q_{1f} being constants.

From Eqs. [30, 31], the total primary creep strain that accumulates under conditions of varying stresses is obtained as:

$$\varepsilon_f^{primary} = \int_0^t \frac{1}{3}[q_{of} + q_{1f}\sigma_f]t^{-2/3}dt \quad [32]$$

The constant stress secondary creep strain is obtained by integrating Eq. [17]:

$$\varepsilon_f^{secondary}\Big|_{\sigma=constant} = K_f[\sigma_f]^{n_f} t \quad [33]$$

From integration of Eq. [33], total secondary creep strain accumulated under conditions of varying stresses is given as:

$$\varepsilon_f^{secondary} = \int_0^t K_f[\sigma_f]^{n_f} dt \quad [34]$$

Using Eqs. [20-22, 25-29, 32, 34], in the strain-compatibility condition of Eq. [18] leads to:

$$\underbrace{\frac{\sigma_m}{E_m}}_{\text{matrix-elastic-strain}} + \underbrace{\int_0^t \left[\frac{1}{3}\left[q_{om} + q_{1m}\sigma_m\right]t^{-2/3} + K_m\left[\sigma_m\right]^{n_m}\right]dt}_{\text{matrix-plastic-strain}} = \underbrace{\frac{\sigma_f}{E_f}}_{\text{fiber-elastic-strain}} + \underbrace{\int_0^t \left[\frac{1}{3}\left[q_{of} + q_{1f}\sigma_f\right]t^{-2/3} + K_f\left[\sigma_f\right]^{n_f}\right]dt}_{\text{fiber-plastic-strain}} \quad [35]$$

Using Eq. [35] in the strain-rate compatibility condition Eq. [18]:

$$\underbrace{\frac{\dot{\sigma}_m}{E_m}}_{\text{matrix-elastic-rate}} + \underbrace{\frac{1}{3}\left[\left[q_{om} + q_{1m}\sigma_m\right]t^{-2/3}\right] + K_m\left[\sigma_m\right]^{n_m}}_{\text{matrix-plastic-rate}} = \underbrace{\frac{\dot{\sigma}_f}{E_f}}_{\text{fiber-elastic-rate}} + \underbrace{\frac{1}{3}\left[\left[q_{of} + q_{1f}\sigma_f\right]t^{-2/3}\right] + K_f\left[\sigma_f\right]^{n_f}}_{\text{fiber-plastic-rate}} \quad [36]$$

Introducing Eq. [13, 15] in Eq. [36] and upon rearranging:

$$\dot{\sigma}_f = \left[\frac{K_m\left[\frac{\sigma_{comp} - \sigma_f v_f}{v_m}\right]^{n_m} - K_f\sigma_f^{\,n_f} + \frac{1}{3}\left[q_{om} + q_{1m}\left[\frac{\sigma_{comp} - \sigma_f v_f}{v_m}\right] - q_{of} - q_{1f}\sigma_f\right]t^{-2/3}}{\frac{1}{E_f} + \left[\frac{v_f}{v_m}\right]\frac{1}{E_m}}\right] \quad [37]$$

This differential equation can then be solved numerically using standard Runge-Kutta method for fiber stress as a function of time subject to the initial condition that upon loading at time=0, the stress in the fiber as dictated by the elastic solution:

$$\varepsilon_m^{plastic} = \varepsilon_f^{plastic} = 0 \quad [38]$$

is:

$$\sigma_f\big|_{t=0} = \frac{\sigma_{comp}}{\left[v_f + v_m\frac{E_m}{E_f}\right]} \quad [39]$$

where Eqs. [13, 22, 29] are used with Eq. [38].

The composite strain-rates and strains are then computed as functions of time from Eq. [35, 36]. If the matrix primary is insignificant, i.e.:

$$\varepsilon_m^{primary} = 0 \quad [40]$$

then Eq. [37] can be rewritten as:

$$\dot{\sigma}_f = \left[\frac{K_m \left[\frac{\sigma_{comp} - \sigma_f v_f}{v_m} \right]^{n_m} - K_f \sigma_f^{n_f} + \frac{1}{3}\left[-q_{of} - q_{1f}\sigma_f \right] t^{-2/3}}{\frac{1}{E_f} + \left[\frac{v_f}{v_m} \right] \frac{1}{E_m}} \right] \quad [41]$$

and solved numerically for composite strain-rates and strains as indicated above.

3.4.4.1.1.5 Comparison of present and existing primary creep models

A review of literature indicates there has been one attempt to quantify the primary creep of long-fiber composites for the case of a creeping fiber in a creeping matrix [64]. This analysis was performed as follows.

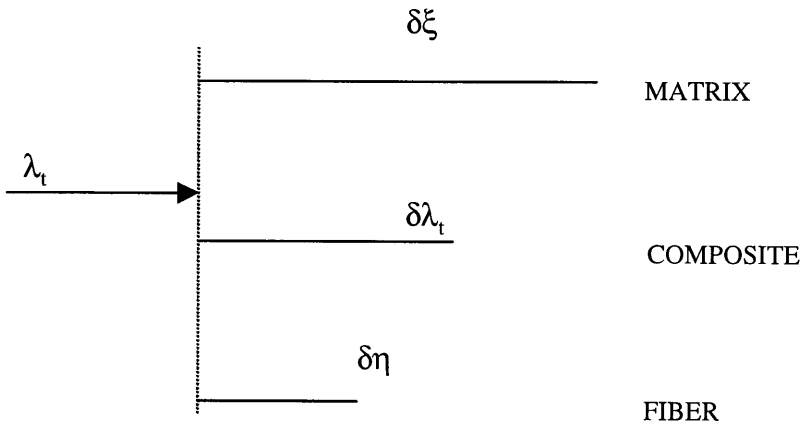

Figure 40. Virtual displacements in time δt of the components of a continuously reinforced composite during creep.

Let λ_t be the extension of the composite at any instant t [Figure 40]. In the next small time interval δt the matrix creeps a distance δξ under the influence of stress σ_m present at the beginning of the time-step. Then:

$$\delta\xi = h_o \frac{d\varepsilon_m}{dt} \delta t \quad [42]$$

where h_o is the initial length of the composite, $d\varepsilon_m/dt$ is the creep-rate of the matrix at the beginning of the time-step. Similarly the fiber creeps a distance δη given by a similar expression:

$$\delta\eta = h_o \frac{d\varepsilon_f}{dt} \delta t \quad [43]$$

In order to maintain material strain-compatibility the composite extends an intermediate amount $\delta\lambda_t$.

Therefore during the interval δt the matrix relaxes its stress by $(-\delta\sigma_m)$ given by:

$$-\delta\sigma_m = E_m\left[\frac{\delta\xi - \delta\lambda_t}{h_o}\right] \qquad [44]$$

As the total composite stress remains constant the decrease in matrix stress is matched by a corresponding increase in the fiber stress weighted by corresponding volume fractions obeying rule of mixtures given as:

$$E_m\left[\frac{\delta\xi - \delta\lambda_t}{h_o}\right]v_m = E_f\left[\frac{\delta\lambda_t - \delta\eta}{h_o}\right]v_f \qquad [45]$$

From Eqs. [42-45] the rate of change of matrix stress with time is given as:

$$\frac{\delta\sigma_m}{\delta t} = \frac{\left[\frac{d\varepsilon_f}{dt} - \frac{d\varepsilon_m}{dt}\right]}{\left[\frac{1}{E_m} + \frac{v_m}{v_f E_f}\right]} \qquad [46]$$

Matrix and fiber strains are modeled as functions of stress and time as:

$$\varepsilon_m = \psi_m(\sigma_m, t) \qquad [47]$$

$$\varepsilon_f = \psi_f(\sigma_f, t) \qquad [48]$$

and matrix and fiber strain-rates are modeled as:

$$\frac{d\varepsilon_m}{dt} = \frac{\partial\psi_m}{\partial\sigma_m}\frac{d\sigma_m}{dt} + \frac{\partial\psi_m}{\partial t} \qquad [49]$$

and

$$\frac{d\varepsilon_f}{dt} = \frac{\partial \psi_f}{\partial \sigma_f}\frac{d\sigma_f}{dt} + \frac{\partial \psi_f}{\partial t} \qquad [50]$$

Under constant stress conditions, the fiber and matrix stress changes are related as:

$$\dot{\sigma}_m = -\left[\frac{v_f}{v_m}\right]\dot{\sigma}_f \qquad [51]$$

Substituting Eq. [51] in Eq. [50]:

$$\frac{d\varepsilon_f}{dt} = -\frac{v_m}{v_f}\frac{\partial \psi_f}{\partial \sigma_f}\frac{d\sigma_m}{dt} + \frac{\partial \psi_f}{\partial t} \qquad [52]$$

Using Eqs. [46, 52] the rate of change of matrix stress with time is given as:

$$\frac{\delta\sigma_m}{\delta t} = \frac{\left[\frac{\delta \psi_m}{\delta t} - \frac{\delta \psi_f}{\delta t}\right]}{\left[\frac{1}{E_m} + \frac{v_m}{v_f E_f} + \frac{\delta \psi_m}{\delta \sigma} + \frac{v_m}{v_f}\frac{\delta \psi_f}{\delta \sigma}\right]} \qquad [53]$$

This model can then be checked with the model presented in this thesis by using explicit expressions for the matrix and fiber strains for the simple case when the matrix and the fiber do not exhibit primary creep:

$$\psi_m(\sigma_m, t) = \frac{\sigma_m}{E_m} + \int_0^t K_m[\sigma_m]^{n_m}\, dt \qquad [54]$$

$$\psi_f(\sigma_f, t) = \frac{\sigma_f}{E_f} + \int_0^t K_f[\sigma_f]^{n_f}\, dt \qquad [55]$$

Using Eqs. [54, 55] in Eq. [53], the rate of change in the matrix stress with time is given as:

$$\frac{\delta\sigma_m}{\delta t} = \frac{\left[K_f[\sigma_f]^{n_f} - K_m[\sigma_m]^{n_m}\right]}{2\left[\frac{1}{E_m} + \frac{v_m}{v_f E_f}\right]} \qquad [56]$$

Setting the primary creep of fiber to zero in Eq. [41] the composite primary creep model developed in this thesis transforms to:

$$\frac{\delta\sigma_m}{\delta t} = \frac{\left[K_f[\sigma_f]^{n_f} - K_m[\sigma_m]^{n_m}\right]}{\left[\frac{1}{E_m} + \frac{v_m}{v_f E_f}\right]} \qquad [57]$$

Comparing Eq. [56] and Eq. [57], it is evident there is a factor of two difference between the model developed by De Silva and the one presented in § 3.4.4.1.1.4.

While the imposition of strain-compatibility Eq. [45] is correct, De Silva's assumption in Eq. [44] that the stress relaxation in the matrix is accommodated entirely by elastic strains appears to be incorrect and De Silva also does not impose the strain-rate compatibility criterion. The exact solution as demonstrated in the primary creep model developed in § 3.4.4.1.1.4 depends on the elastic and creep components of fiber and the matrix and is determined by imposing both strain and strain-rate compatibility criteria without approximating for changes in stress levels in either of the two constituents.

3.4.4.1.1.6 Application of the model to a typical composite

The model developed in the previous section is applied to characterize the 1025°C creep response of a NiAl-W composite under a compressive stress of 120 MPa. The various input parameters are as indicated in Table 17.

Table 17. 1025°C input parameters for the primary creep model.

Property	NiAl	Measured stress-range	W	Measured stress-range
E	128 GPa [44]		366 GPa [44]	
k	$6.37\ 10^{-14}$ MPa$^{-5.6}$ s^{-1}	15-32 MPa	$3.48\ 10^{-26}$ MPa$^{-6.77}$ s^{-1}	450-720 MPa
n	5.6		6.77	
q_0	0		-0.00028242 MPa	
q_1	0		$8.6417\ 10^{-7}$ MPa^{-1}	

At time t=0, upon loading a composite with 15% W to 120 MPa, the stresses in fiber and matrix evolve from their elastic values of 268 MPa and 94 MPa [Eq. [39]] to their respective steady-state values of 700 MPa and 18 MPa [Eqs. [17, 18]] over a time-scale of 10000 seconds, as illustrated in Figure 41. (As there is a singularity in the solution for stress at time t=0, the initial time used in numerical simulations is set at 0.001 seconds. The subsequent time-steps for the numerical computations are typically on the order of 1 second.)

Over the same time-span the contribution to total fiber strain-rate from the elastic and plastic (i.e. primary and secondary) parts is illustrated in Figure 42. At very short-times (less than 4 seconds) the elastic strain-rate term dominates while at longer times (after 2000 seconds) it becomes

vanishingly small. This is to be expected as the fiber stress changes rapidly at short-times and remains virtually unchanged at longer times [Figure 42].

At short-times, the primary part of the plastic-rate dominates over the secondary part of the plastic-rate while at longer times, the secondary term dominates as the primary contribution diminishes with time.

Thus the total fiber strain-rate is determined almost entirely by the secondary part of the plastic component [Eq. [35]] at longer times.

The composite creep strains can then be calculated as a function of time under three different conditions.

a. Using McLean's model [Eq. [26]] assuming the composite reaches a steady-state virtually instantaneously upon loading. In this case the creep curve is linear in time with the composite creeping at a constant steady-state McLean rate from time=0 [Eq. [12]] [Figure 43].

b. Using the present model, but ignoring primary creep regime in W [Eq. [41] with $q_{of} = q_{1f} = 0$]. In this case, the composite creep curve exhibits a primary region wherein the creep-rate is constantly decreasing, and followed by a secondary region where the creep-rate remains constant and equal to the McLean strain-rate. [Figure 44].

c. Using the present model, but incorporating the primary creep regime in W [Eq. [41]]. In this case, the composite exhibits a primary region that is more pronounced and extended over longer times compared to case (b) and followed by a secondary region. As expected, at any time t, composite creep strain predicted by this model is more than that predicted by either case (a) or case (b) [Figure 44].

This model can then be applied to systematically investigate the compressive creep behavior, particularly the primary portion, of composites at different conditions of applied temperatures, stresses, and volume fractions of reinforcements.

The two most important parameters that characterize the composite primary are:

- Total primary-creep strain accumulated by the composite ε_p defined as the total strain that is accumulated by the composite while the primary region is dominant.
- Total time over which the primary region is dominant t_p defined as the time over which the primary plastic-rate contribution is greater than the secondary plastic-rate contribution [Figure 42].

The primary creep strain ε_p exhibits a complex dependence with changes in applied stress and reinforcement volume fraction at a given temperature [Figure 45]. This is because primary creep-strains are integrated from strain-rate transients whose dependence with the composite stresses and volume fractions is fairly complex.

The primary time t_p on the other hand, decreases with applied stress at all the four different volume fractions [Figure 46]. The parametric [Figure 67] study also indicates that t_p can be uniquely related to the steady-state McLean strain-rate of the composite through the following empirical relation:

$$t_p[\dot{\varepsilon}_{ss}]^{\nu} = \lambda \qquad [58]$$

where the steady-state strain-rate exponent ν has been determined to be 1.1 and λ is 6 10^{-4} at 1025°C for the applied composite stress range 100 to 130 MPa investigated.

3.4.4.1.1.7 Model conclusions

- Primary creep is more significant at relatively high stresses and for composites with high volume fraction of reinforcements.
- Primary creep strain displays a complex dependence with changes in stresses and reinforcement volume fraction, while primary time can be uniquely linked to the McLean steady-state creep rate of the composite.

3.4.4.1.2 Experimental verification

Compression creep experiments were carried out on NiAl-reinforced with 6-14 volume % of W at 1025°C and at two different stress levels, 80 MPa [Figure 48, Figure 49] and 120 MPa [Figure 50, Figure 51] [§ 3.2.2].

Experimentally obtained creep curves exhibit reasonable agreement with model predictions for the spectrum of volume fractions investigated in most cases [Figure 48, Figure 49, Figure 51]. It is also noted that for cases where there exists a good correlation between the predicted and the observed steady-state creep-rates, there is also a good correlation between the predicted and observed primary creep strains. As the strain-rate transients converge to the predicted steady-state creep-rates the primary creep-strains computed by integration of strain-rate transients are also expected to converge to the observed values.

3.4.4.1.3 Limitations of the primary creep model

- The accuracy of predictions of the primary creep model developed here is strongly dependent on the accuracy of the various input parameters, particularly NiAl and W, primary and steady-state creep parameters, and W volume fraction.

- In developing the model, it has been assumed that primary creep of NiAl can be considered negligible. A more accurate analysis could be carried out by including the primary creep effects of NiAl.

- Also the steady-state creep parameters have been obtained as power-law fits of steady-state strain-rates vs. stress. It is quite likely that individual samples may exhibit deviations in steady-state creep-rates from the expected value by up to a factor of 2 at a given stress.

- All the fibers have been modeled as being perfectly straight with no imperfections. If the fibers do bend/buckle then the mechanics of primary creep need to reworked to compute the new primary creep-strains.

3.4.4.1.4 Figures and illustrations

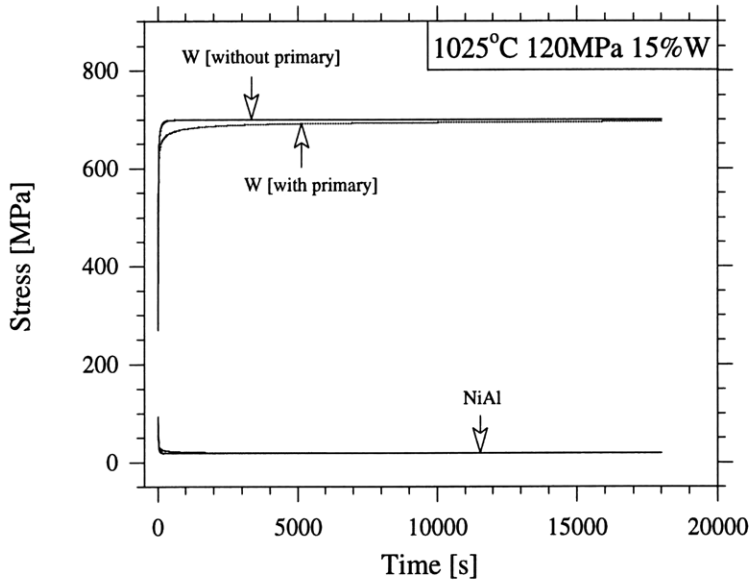

Figure 41. Evolution of stresses in NiAl and W from the primary to secondary stage.

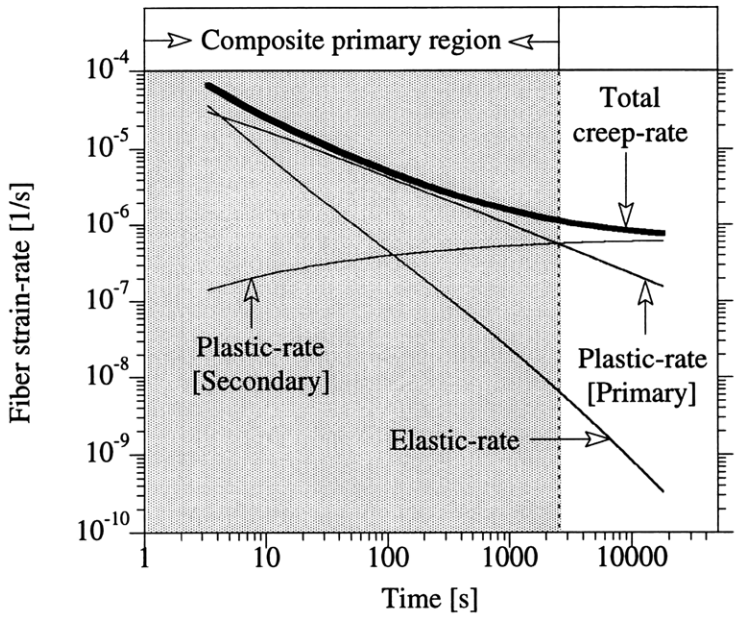

Figure 42. Primary and secondary contributions to the fiber creep-rate at 120 MPa.

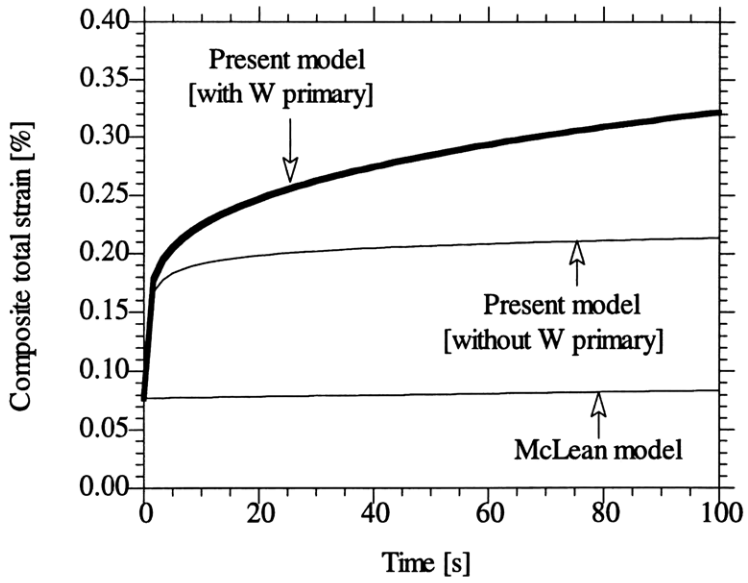

Figure 43. Composite creep strain obtained as a function of time using primary creep model (120 MPa, 15% W, 1025°C).

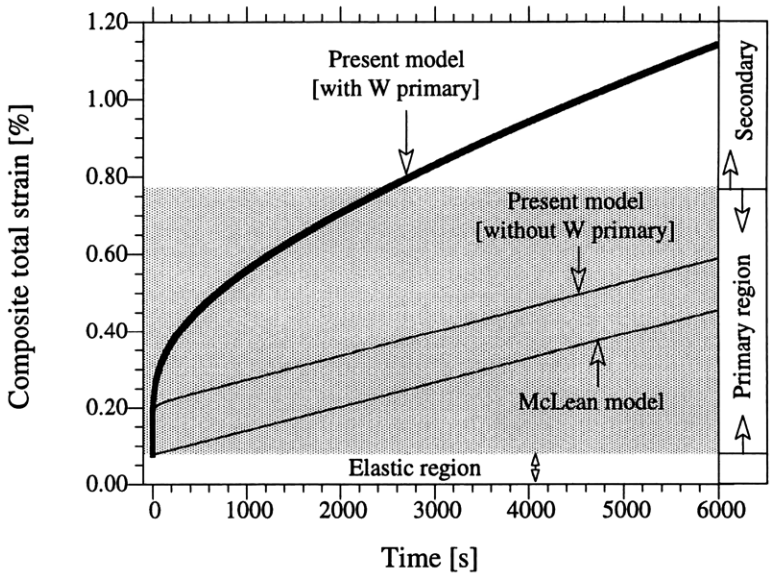

Figure 44. Composite creep strain obtained as a function of time using primary creep model (120 MPa, 15% W, 1025°C).

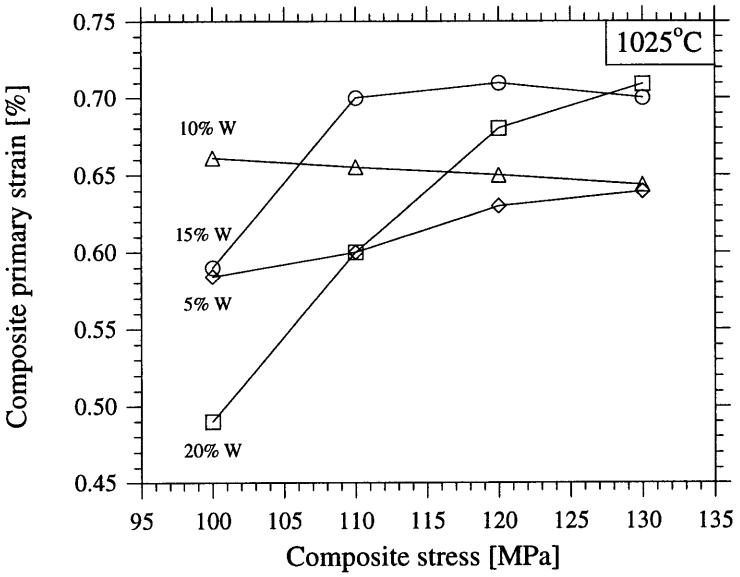

Figure 45. Variation of composite primary creep strain with applied composite stress indicating complex dependence of primary creep strain with composite stress.

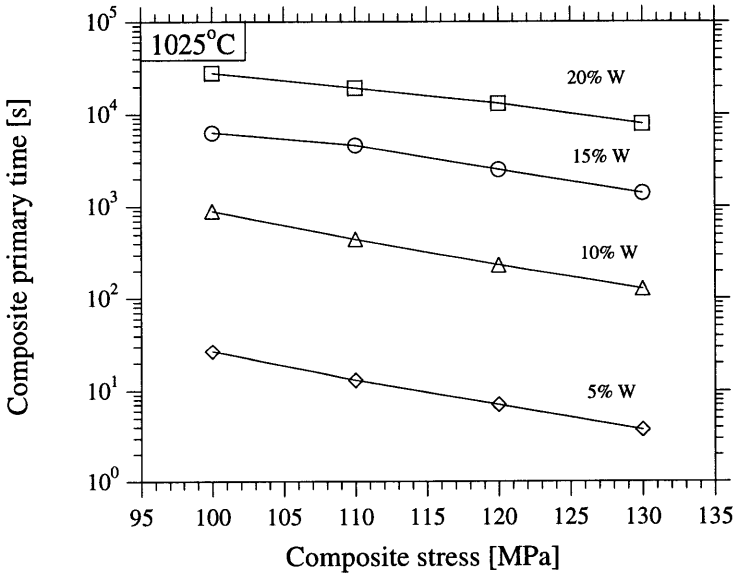

Figure 46. Variation of composite primary time with applied composite stress indicating a simple dependence of primary creep time with composite stress.

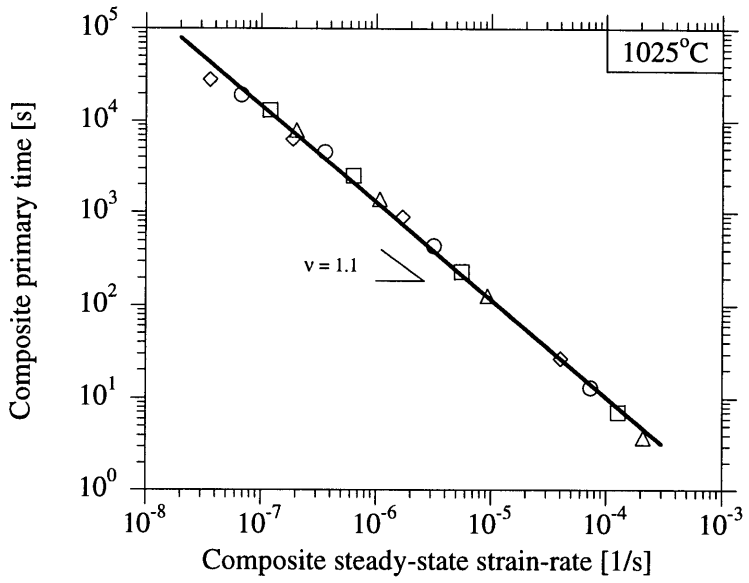

Figure 47. Variation of composite primary time with the composite steady-state strain-rate demonstrating a unique dependence with the composite steady-state creep-rate.

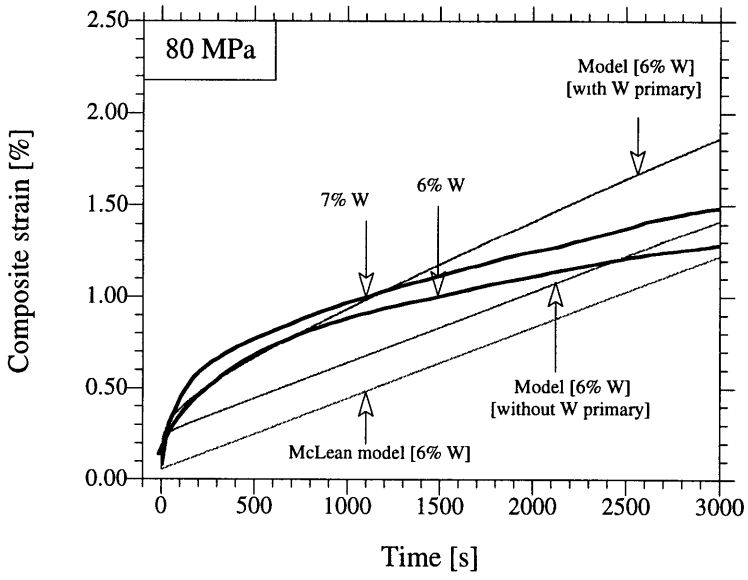

Figure 48. Comparison of theoretically predicted with experimental observed creep behavior demonstrating good correlation.

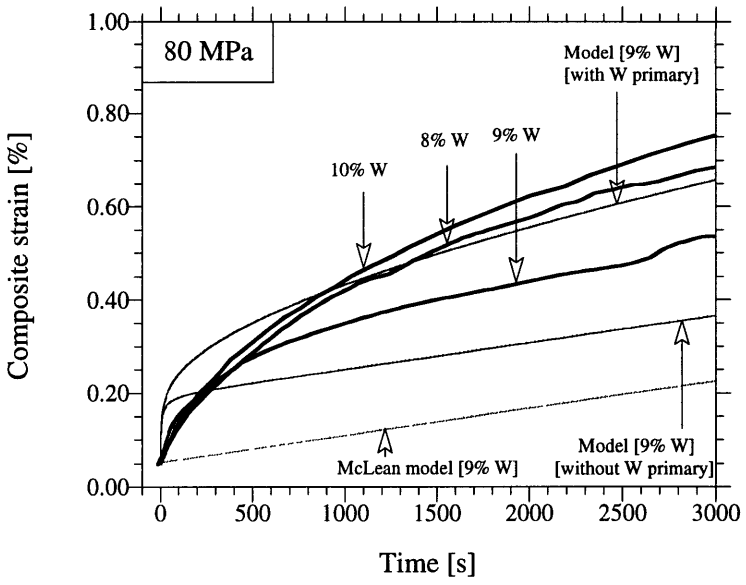

Figure 49. Comparison of theoretically predicted with experimental observed creep behavior demonstrating good correlation.

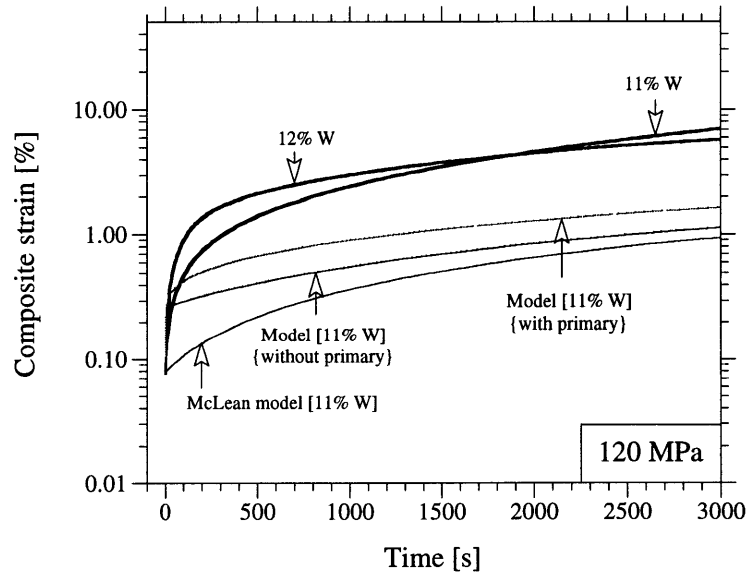

Figure 50. Comparison of theoretically predicted with experimental observed creep behavior with the model underpredicting the primary creep behavior by one order of magnitude at large times.

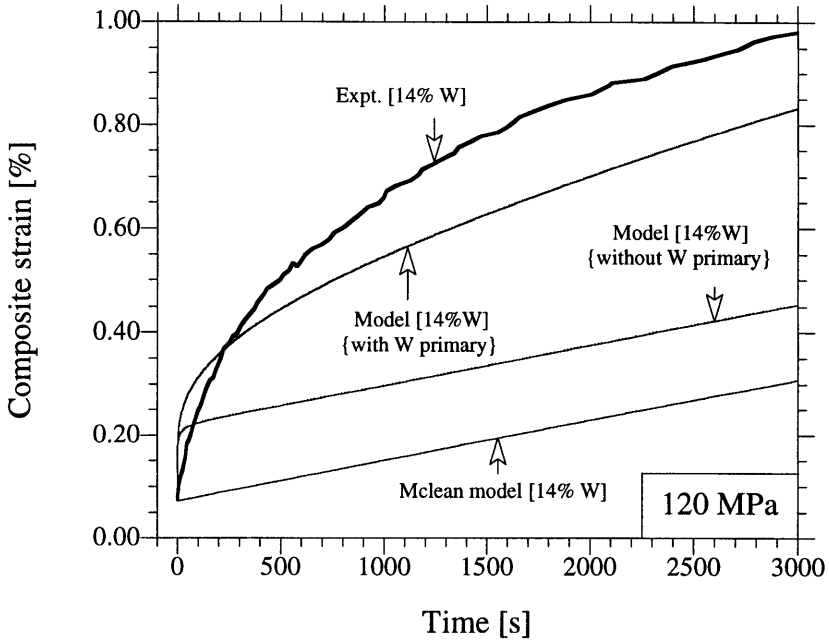

Figure 51. Comparison of theoretically predicted with experimental observed creep behavior demonstrating good correlation.

3.4.4.2 Secondary creep

Uni-directionally reinforced long-fiber composite systems loaded longitudinally in the direction of fibers exhibit a secondary creep regime, characterized by a steady-state in the composite creep-rate under conditions of constant stresses. This steady-state is established when both creeping constituents (i.e. matrix and fiber) attain their respective steady-states.

3.4.4.2.1 Model

The composite secondary creep behavior has been modeled by McLean [42] using a system of parallel dash-pots [Figure 52] – a limiting case of the model presented in § 3.4.4.1.1 [Figure 39] on modeling primary creep behavior, wherein at long times, the elastic and primary creep components cease to be of importance.

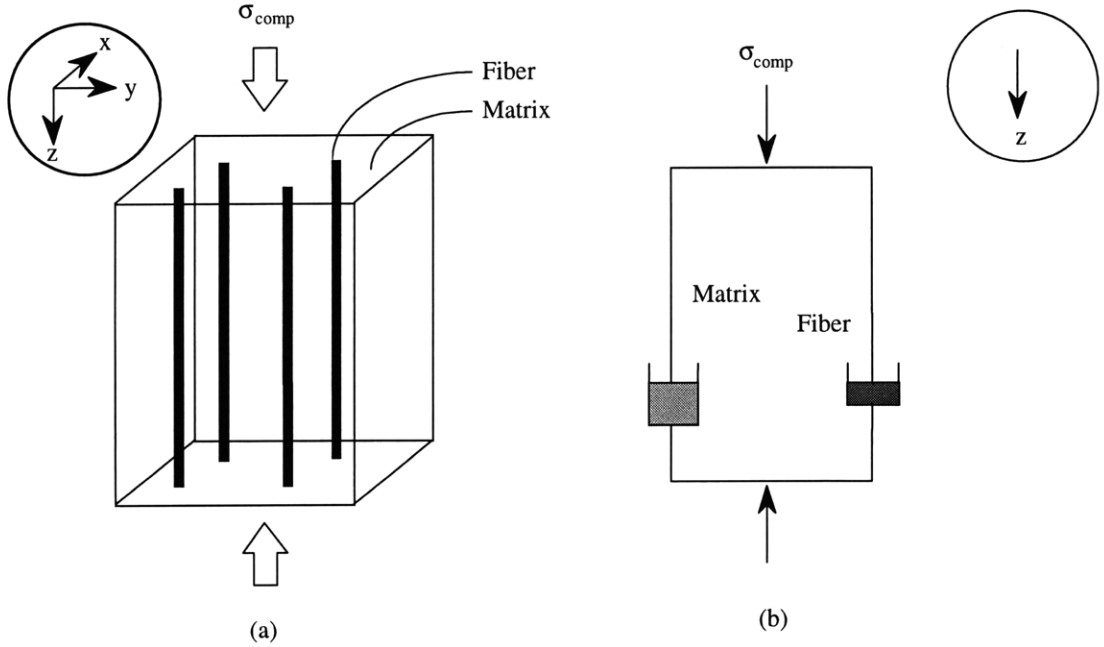

Figure 52. Schematic of model for secondary creep stage.

The composite creep stress is related to the fiber and the matrix stress as in Eq. [13] which essentially is a rule of mixtures formulation. The McLean steady-state strain-rate of the composite $\dot{\varepsilon}_{ss}$ is obtained as an implicit function of the applied composite stress σ_{comp} [42]:

$$\sigma_{comp} = v_f \left[\frac{\dot{\varepsilon}_{ss}}{K_f}\right]^{1/n_f} + \left[1 - v_f\right]\left[\frac{\dot{\varepsilon}_{ss}}{K_m}\right]^{1/n_m} \qquad [59]$$

where n, K, and v represent stress exponent, pre-exponent, and volume fraction – with subscripts m and f denoting matrix and fiber respectively. It has been demonstrated [60] that the zone of dislocation interaction with the fibers is on the order of about 1 μm. Hence in composites with large fiber diameters (>100 μm) the effects of dislocation interaction at the fiber-matrix interface are expected to be small and hence are ignored in this model analysis.

3.4.4.2.1.1 Application of the model to a typical composite system

The McLean model developed for tensile loading conditions is applied to a model NiAl-W composite system, reinforced with 5-20% W, loaded in compression at 715°C and 1025°C, using experimentally obtained creep constants n and K, for NiAl and W [Table 12].

The model analysis indicates:

- At the lower temperature, 715°C [Figure 53], where the stress exponents of NiAl and W are vastly different the strengthening effect as determined by the ratio of strain-rates at a given stress due to increasing volume fraction of reinforcement is more pronounced at lower applied composite stresses.

- At the higher temperature, 1025°C [Figure 54], where the stress exponents of NiAl and W are very similar, the strengthening effect due to increasing volume fraction of reinforcement does not exhibit a strong dependence on the applied stress.

In this analysis, it is implicitly assumed that the deformation mechanism does not change over the entire stress-range. In reality, diffusional creep could become dominant at strain-rates below 10^{-9} s^{-1} and power-law breakdown is expected above 10^{-3} s^{-1}. As the experiments were carried out typically within a stress-range that produced creep-rates between 10^{-8} s^{-1} and 10^{-5} s^{-1}, this assumption is quite valid.

3.4.4.2.2 Experimental verification

The 715°C compressive steady-state creep behavior was investigated over a range of stresses and volume fractions [Table 11]. The experimentally obtained steady-state strain-rates correlate reasonably well with model predictions [Figure 55].

The 1025°C compressive steady-state behavior was also investigated at 120 MPa and 80 MPa for low volume fractions of W, between 5 and 15% [Table 11]. Good correlation between model predictions and experimental results is demonstrated [Figure 56].

3.4.4.2.3 Limitations of the secondary creep model

The NiAl-W composite steady-state creep-rate can be influenced by many metallurgical and mechanical factors as summarized in Table 18.

Table 18. Expected effect on the NiAl-W composite compressive steady-state creep-rate due to various metallurgical/mechanical phenomena occurring in NiAl, W and at the NiAl-W interface.

NiAl	W	NiAl-W interface	Expected effect on composite compressive steady-state creep-rate
Inclusions, impurities, interstitials			Strengthening
Off-stoichiometry			Weakening
	Tension/compression asymmetry (cavitation in tension)		Strengthening
	Solid solution of Ni in W		Strengthening
	Recrystallization		Weakening
W in solid solution with NiAl			Strengthening
Reprecipitation of W at NiAl grain boundaries			Strengthening
	W fiber misorientation		Weakening
		Debonding	Weakening

Aluminum oxide (from surface of aluminum stock) and zirconium oxide (from Zircwash slurry) inclusions, carbon (from reservoir and gate), oxygen (from oxides), silicon (from quartz crucible), and manganese (from Ni wires) impurities may have been picked up by NiAl during the processing stage. Even trace amounts of these impurities could enhance the creep-strength of NiAl by impeding dislocation glide. While the monolithic NiAl could also pick up similar impurities, the extent of contamination might vary across different samples.

It has been demonstrated that NiAl ingots obtained by reactive infiltration have composition gradients. Off the 50-50 at. % Ni-Al stoichiometry by about 5 at. % could reduce the creep strength by up to a factor of 2 [2].

The W wires have been tested in tension while W wires in the composite are under compressive stress-states. Typically little difference is expected in the creep-rates of monolithic homogeneous metals when tested in tension and compression. However, it has been observed that cavitation could occur during early stages of creep under tensile stresses, thus enhancing creep-rates, while cavitation does not occur in compression until the later stages of creep, thus making the material stronger in compression.

While nickel has very little solid-solubility in W a limited amount of solid-state diffusion of Al into W wire is possible. This could strengthen W by solid solution strengthening. It has been demonstrated that reactive infiltration processing causes part of W fibers to recrystallize. This could reduce the strengthening effects induced by the wire-drawing process. As current models are based on experiments with W that has not been recrystallized, the effects of recrystallization are not captured.

It has also been demonstrated that reactive infiltration processing of NiAl-W composites results in the dissolution of 2% W into the NiAl matrix and its subsequent reprecipitation at the NiAl

grain-boundaries. While this is expected to increase creep strength of NiAl, the extent of creep-strengthening due to this phenomenon has also not been quantified.

The secondary creep model assumes all W fibers to be perfectly straight and aligned with the loading axis. Any deviations from the loading axis will result in a reduction in the creep strength.

It has also been implicitly assumed that the NiAl-W interface is strong and does not debond. Any debonding will reduce the load-transfer capability across the interface and thus reduce the creep strength of the composite, thus explaining the variations in Figure 55 and Figure 56.

Thus depending on the degree of dominance of each factor, an overall strengthening or weakening of the NiAl-W composite could be obtained.

3.4.4.2.4 Figures and illustrations

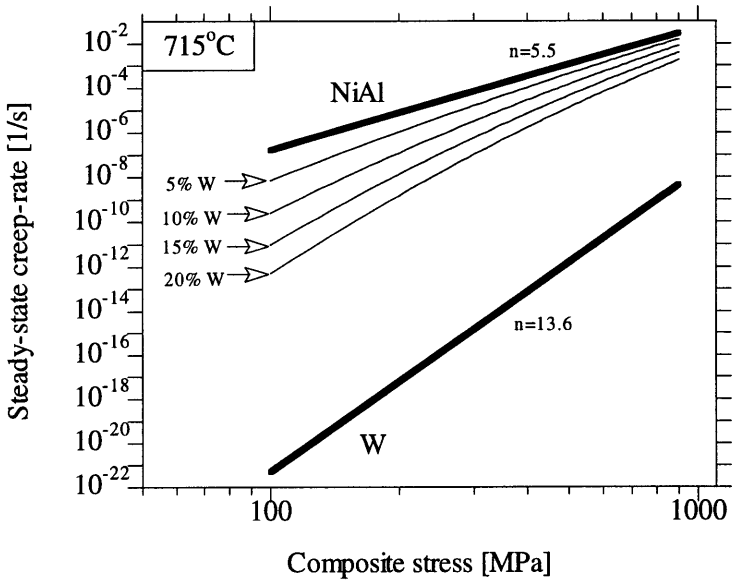

Figure 53. 715°C steady-state creep behavior of NiAl reinforced with different volume fractions of W.

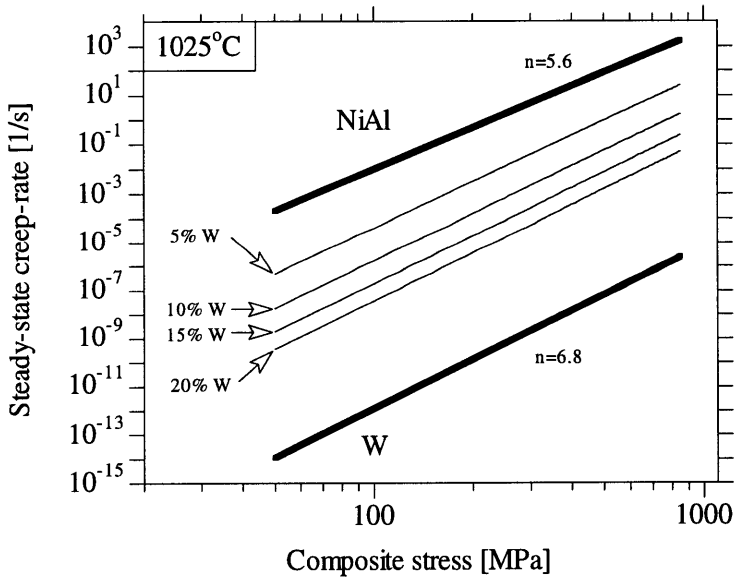

Figure 54. 1025°C steady-state creep behavior of NiAl reinforced with different volume fractions of W.

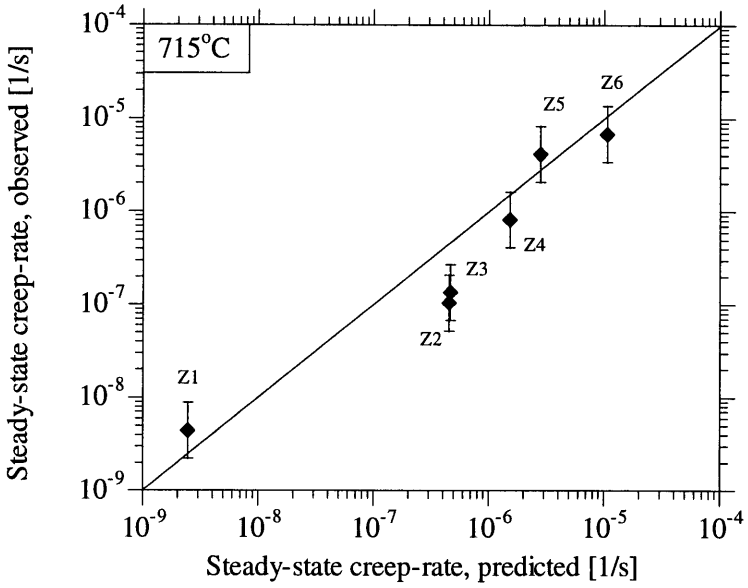

Figure 55. Comparison of the steady-state creep-rates predicted by secondary model prediction with experiments for NiAl-W composites at 715°C.

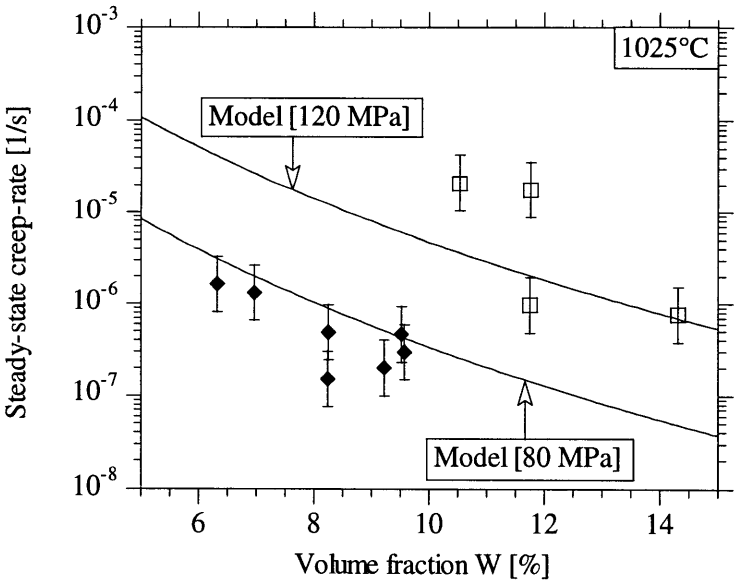

Figure 56. Comparison of the steady-state creep-rates predicted by secondary model prediction with experiments for NiAl-W composites at 1025°C.

3.4.4.3 Tertiary creep

Uni-directionally reinforced fiber-composite materials, loaded longitudinally in the direction of fibers, at temperatures wherein both the constituents (fiber and matrix) creep, exhibit a secondary creep regime, characterized by a steady-state in the composite creep-rate under conditions of constant compressive stresses. This overall composite steady-state is established when both creeping constituents attain their respective steady-state stress after load partitioning is completed as has been discussed in § 3.4.4.2 on secondary creep. This secondary stage can be followed by a tertiary stage wherein the composite creep-rate increases over and above the steady-state value, accelerates, and leads to sample failure.

The tertiary stage can be caused by four different macroscopic phenomena [Figure 57]:

- brooming
- bulging
- buckling
- kinking

each of which is characterized by a microscopic phenomenon, i.e. fiber deflections away from the loading axis. Brooming and bulging, wherein the fiber rotations are typically rotationally symmetrical about the loading-axis, exhibit out-of-loading-plane fiber rotations, while fiber rotations are typically constrained to the loading plane when kinking occurs. Buckling can happen in either mode.

Brooming and bulging display a strong dependence on the local stress-states at the regions of application of stresses and hence are classified as end-effect phenomena. When the end-effects are suppressed, buckling or kinking, becomes the dominant mode of deformation and thus represents the bulk behavior of the material. The influence of extrinsic factors, i.e. temperature and stress, and intrinsic factors, i.e. fiber volume fraction and defect geometry, on buckling and kinking, is examined and their effects on the composite creep-rate is then established.

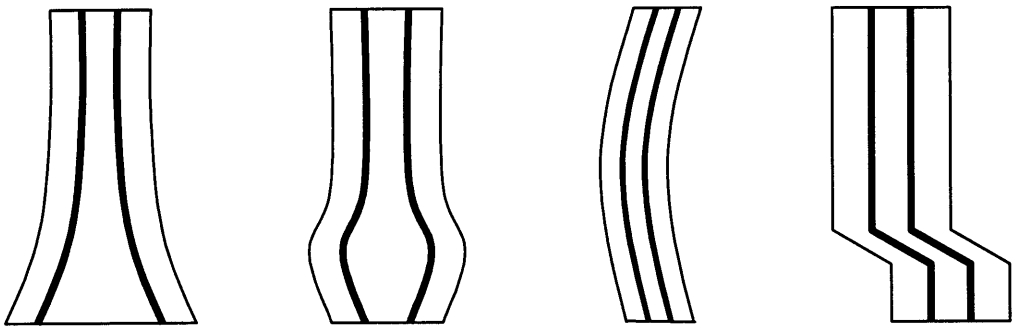

Figure 57. Schematic indicating four fiber deformation modes – brooming, bulging, buckling, and kinking, that contribute to composite tertiary creep.

3.4.4.3.1 Kinking Model

3.4.4.3.1.1 Assumptions

The kinking model is built upon the following key assumptions:

1. Processing of long-fiber composites typically result in composites with local imperfections in fiber alignment [Figure 58a].
2. As kinking involves fiber-rotations/deflections that are typically constrained to the loading-plane, the problem is treated under plane-stress conditions.
4. Upon application of a far-field composite stress, the kinked region, being transversely isotropic, and loaded in a direction that does not contain a symmetry plane, a net plastic shear strain is developed in the local volume element [Figure 58b].
5. Since the matrix deforms by creep wherein the material volume is conserved, the plastic shear strain developed in the local volume element, is transmitted across the entire width of the material, causing all other fibers to rotate from their originally straight geometries, thus creating a kink band [Figure 58b].
6. The bending stiffness of the creeping fibers is assumed to be low and hence rotations in the originally kinked fiber translate fully and immediately to other straight fibers.
7. Composite creep-rate in the direction of the applied stress is obtained as a sum of the strain-rates in the kink band and from the unkinked portions of the material, weighted according to their corresponding length scales [Figure 58c].
8. At the late stages of the tertiary, when the kink band is fully developed, the composite will experience bending moments and the global stress-state is no longer expected to be purely uni-axial. The bending moments are expected to increase the creep-rate of the composite. This model, by not accounting for the additional creep-rate contribution from the bending moments, presents a conservative lower bound for the composite creep-rate.

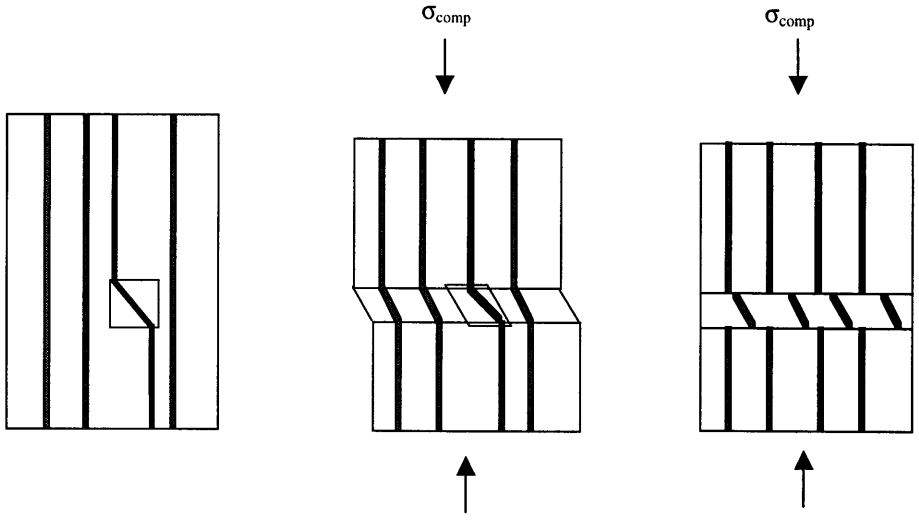

Figure 58. Schematic of model for tertiary creep.

The creep-rate of a composite with a kink band of length l_k and a straight unkinked segment of length l_u is given as:

$$\dot{\varepsilon}_{comp} = \left[\frac{l_k \dot{\varepsilon}_k + l_u \dot{\varepsilon}_u}{l_k + l_u}\right] \quad [60]$$

where $\dot{\varepsilon}_k$ and $\dot{\varepsilon}_u$ represent strain-rates in the kinked and unkinked regions of the material, in the direction of the applied compressive stress. The strain-rate contribution from the straight segment can be modeled exactly as in § 3.4.4.2.1 [Eq. [59]]:

$$\sigma_{comp} = v_f \left[\frac{\dot{\varepsilon}_u}{K_f}\right]^{1/n_f} + v_m \left[\frac{\dot{\varepsilon}_u}{K_m}\right]^{1/n_m} \quad [61]$$

where σ_{comp} is the applied composite stress, v_f and v_m are fiber and matrix volume fraction, n_m and n_f are matrix and fiber stress-exponents, and K_m and K_f are matrix and fiber creep constants in the power law that relates strain-rate to stress [Eq. [7]].

Eq. [61] describes a relationship between stress and strain-rate that does not conform to a power law when a wide stress range is considered. However, within a limited range of stresses, the composite creep-rate can be modeled accurately by a power law [Figure 60]:

$$\dot{\varepsilon}_{straight} = K_{comp} \sigma_{comp}^{\ n_{comp}} \quad [62]$$

where n_{comp} and K_{comp} are stress-exponent and creep constants for the composite.

The strain-rate contribution from the kink-band is obtained following Johnson's approach [61]. The applied uni-axial composite stress-state σ_{comp} is transposed to an equivalent three component multi-axial stress-state consisting of a compressive stress parallel to the fiber axis σ_{zz}, a compressive stress normal to the fiber σ_{xx} and a shear stress in a plane parallel to the fibers σ_{xz}:

$$\sigma_{zz} = \sigma_{comp} \cos^2 \alpha \quad [63]$$

$$\sigma_{xx} = \sigma_{comp} \sin^2 \alpha \quad [64]$$

$$\sigma_{xz} = \sigma_{comp} \cos \alpha \sin \alpha \quad [65]$$

where α is the fiber orientation with regard to the loading direction.

The corresponding strain-rate components in the plane of loading are [61]:

$$\dot{\varepsilon}_{zz} = U^{m-1}\sigma\left[-\frac{1}{2}\lambda\sin^2\alpha + \lambda\cos^2\alpha\right] \quad [66]$$

$$\dot{\varepsilon}_{xx} = U^{m-1}\sigma\left[\mu\sin^2\alpha - \frac{1}{2}\lambda\cos^2\alpha\right] \quad [67]$$

$$\dot{\varepsilon}_{xz} = \frac{1}{2}U^{m-1}\sigma[\nu\sin\alpha\cos\alpha] \quad [68]$$

where U is given as:

$$U = \left[\lambda\cos^4\alpha + (\nu-\mu)\sin^2\alpha\cos^2\alpha + \mu\sin^4\alpha\right]\sigma^2 \quad [69]$$

wherein, λ, ν, and μ are material constants, and m is related to the composite stress-exponent as:

$$m = \frac{n_{comp}+1}{2} \quad [70]$$

The strain-rate in the loading direction is given by the transformation:

$$\dot{\varepsilon}_{\alpha} = \dot{\varepsilon}_{zz}\cos^2\alpha + \dot{\varepsilon}_{xx}\sin^2\alpha + 2\dot{\varepsilon}_{xz}\sin\alpha\cos\alpha \quad [71]$$

Using Eqs. [66-70] in Eq. [71] [61]:

$$\dot{\varepsilon}_{\alpha} = \left[F_{\alpha}\right]\left[\frac{n_{comp}+1}{2}\right]\sigma^{n_{comp}} \quad [72]$$

where F_{α} is given as:

$$F_{\alpha} = \lambda\cos^4\alpha + (\nu-\mu)\sin^2\alpha\cos^2\alpha + \mu\sin^4\alpha \quad [73]$$

The material constants λ, ν, μ are obtained by using three different boundary conditions set by three creep tests with different values for α. The conditions chosen for this analysis are $\alpha=0^{o}$,

α=90°, and α=89°. When α=0°, the composite creep-rate is predicted exactly by Eq. [61]. When α=90°, typically, the matrix creep-rate dominates that of the fiber by several orders of magnitude. Hence the composite creep-rate is taken to be equal to that of the matrix. At very high values of α, when the composite creep-rate is still dominated by the matrix creep-rate, the composite creep-rate is expected to be relatively insensitive to the changes in α. Hence for α=89°, it is reasonable to set the composite creep-rate to be equal to that of the matrix.

The strain-rate contributions from the kink-band [Eq. [72]] and straight regions [Eq. [61]] of the material are then input in Eq. [60] to obtain the composite creep-rate.

With deformation, the fibers rotate away from the loading axis and α increases. This increases the creep-rate contribution from the kink-band [Eq. [72]] and thus results in an increase in the composite creep-rate. As the creep-rate equations are implicit in nature, an explicit analytical solution to the problem in its most general form is not available. Hence a numerical approach is adopted to solve for the composite creep-rates in an incremental manner over a sequence of finite time-steps, assuming the creep-rates to remain constant with in each time-step.

3.4.4.3.1.2 Application of the model to a typical composite

The Johnson model is applied to a NiAl-W composite system to characterize the kink-band creep-rate as function of α at 1025°C under compressive stresses of 120 MPa [Figure 61] for a range of volume fractions of W from 5% to 20% [Table 19].

The model demonstrates:

- kink-band creep-rates exhibit a weak dependence with changes in α for very low α;
- kink-band creep-rates increase rapidly with small changes in α, at intermediate values of α; and
- at higher values of α, kink-band creep-rates converge to the matrix-strain rate.

Table 19. Input parameters used for the numerical analysis of the kink band model at 1025°C and under applied composite stresses of 80 and 120 MPa.

T [°C]	Stress [MPa]	v_f [%]	Time step [s]	Initial kink length [mm]	Initial kink angle [°]	Sample height [mm]	λ	μ	ν
1025	120	5	20	2	2	20	$2.2\ 10^{-5}$	$9.7\ 10^{-5}$	$1.9\ 10^{-4}$
		10	50	2	2	20	$9.8\ 10^{-6}$	$9.6\ 10^{-5}$	$1.8\ 10^{-4}$
		15	80	2	2	20	$5.7\ 10^{-6}$	$9.6\ 10^{-5}$	$1.9\ 10^{-4}$
		20	100	2	2	20	$3.7\ 10^{-6}$	$9.5\ 10^{-5}$	$1.9\ 10^{-4}$
	80	5	20	2	2	20	$2.1\ 10^{-5}$	$1\ 10^{-4}$	$2.1\ 10^{-4}$
		10	40	2	2	20	$9.8\ 10^{-6}$	$1\ 10^{-4}$	$2.1\ 10^{-4}$
		15	80	2	2	20	$5.6\ 10^{-6}$	$1\ 10^{-4}$	$2.1\ 10^{-4}$
		20	200	2	2	20	$3.7\ 10^{-6}$	$1\ 10^{-4}$	$2.1\ 10^{-4}$

The tertiary kink model is applied to a composite with an initial kink angle of 2^{o} and an initial kink length of 2 mm in a sample 20 mm tall [Table 19]. These defect parameters are typical for normal fiber composites. It is evident from Figure 62 and Figure 63, that the composite creep-rate exhibits three stages when modeled as a function of composite strain:

- In the first stage, the composite creep-rate remains virtually unchanged with composite strain. This region is associated with small rotations of the fibers in the kink-band.
- In the second stage, the composite creep-rate increases rapidly with composite strain. This is associated with the rapid acceleration in fiber rotations in the kink-band.
- In the third stage, the composite creep-rate converges to a new steady-state.

The main results from this analysis are:

- The critical threshold strain defined by the completion of stage 1 and onset of stage 2, varies inversely with the volume fraction of the composite. This implies composites with higher volume fractions of reinforcements are more susceptible to the onset of compressive creep instability in the form of kinking. The higher volume fraction composites are exhibit greater anisotropy in creep strengths and thus fiber rotations cause a relatively higher increase in creep-rates and hence the second stage begins at an earlier time.
- The new steady-state is also reached at the smallest composite strain by the composite with the highest volume fraction of fibers.
- The onset of the second stage, which is typically characterized by an increase in composite creep-rate by many orders of magnitude, signals the onset of the macroscopic tertiary that is observed in the composites.
- While a new steady-state is predicted by this model to occur after the second stage, it is unlikely that such a stage might ever be reached in reality as the problem moves to the domain of large deformations, with the local strains in the kink-band being much larger than the composite strain and will have to be reformulated to account for complex stress-states. From a practical viewpoint, it is of little interest to pursue the problem as the composite will be deemed to have failed soon after the onset of the tertiary stage wherein tremendous accumulations in creep strain occurs over an extremely short period of time.

The tertiary kink model is applied to investigate the effect of initial kink length and kink angle.

First, the effect on the composite tertiary behavior due to changes in initial kink lengths from 1 mm to 4 mm at a constant initial kink angle of 2^{o} at $1025^{o}C$, 120 MPa, and 10% W (sample height 20 mm) is examined [Figure 64].

It is demonstrated that:

- The critical strain threshold for the onset of stage 2 remains almost invariant with changes in the initial kink-lengths.
- The theoretically predicted new steady-states are different for the different composites. The composite with the highest initial kink length converges to the highest creep-rate. This is because the strain-rate contribution from the kink band equals that of the matrix creep-rate and thus the overall composite creep-rate becomes larger.

Second, the effect on the composite tertiary behavior due to changes in initial kink angles from 1^{o} to 4^{o} at a constant initial kink length of 2 mm at 1025°C, 120 MPa, and 10% W is examined [Figure 65].

It is demonstrated that:

- The critical strain threshold for the onset of stage 2, varies inversely with the initial kink angle. The composite with an initial kink angle of 4^{o} moves to stage 2 at the smallest composite strain [Figure 66]. This is because for a composite with a given volume fraction of reinforcement, there exists a critical threshold for α above which the material moves into the tertiary regime. If the initial kink-angle is larger, then the material reaches this threshold value at a lower value of composite strain.
- All composites converge to the same steady-state creep-rate at the end of stage 2. This is because l_k is the same for all the composites.

It is thus concluded for the range of kink angles and kink widths investigated, the critical threshold strain for the onset of stage 2, is determined entirely by the initial kink angle in the composite [Figure 67].

3.4.4.3.2 Experimental verification

Compression creep studies were conducted on NiAl composites reinforced with 5 – 20 volume % W. In most cases, brooming and bulging were the dominant modes of deformation [Table 13]. In one case A2f, the fiber deformation by buckling was observed. In two cases H1r and H2r, pure kinking [Figure 28] was observed. The fiber volume fraction estimated from the observed steady-state creep-rates for the two cases presented here are 15% (H1r) and 17% (H2r). Figure 68 and Figure 69 compare the theoretically predicted creep behavior assuming an initial kink-band angle of 2^{o} and a kink-band length of 2 mm with the experimentally observed creep behavior (The experimentally determined kink-band length is approximately 2 mm).

It is evident that:

- In general there is reasonable agreement between the theoretically predicted and the experimentally observed creep behavior.
- In particular, the critical time threshold for the onset of a catastrophic tertiary is under-predicted by the model in both cases H1r and H2r by 2 and 10 hours respectively when the primary creep of the composite is also taken into account.
- While theory predicts the composite creep-rate to transition from the steady-state to the tertiary almost instantaneously, experiments indicate the transition to be more gradual.

3.4.4.3.3 Limitations of the tertiary kink model

The differences between the predicted and observed creep behavior can be explained as arising from the model assumptions that:

- Local shear strains in regions where fibers are misaligned are transmitted fully and immediately to all other fibers and thus the kink-band sweeps through the entire width of the material. But in reality, the kink-bands are not expected to traverse the entire width , esp. at the early stages. Hence it takes a longer time for the kink-band to fully develop and for the fibers in the kink-band to rotate past the critical threshold angles.
- The model assumes an initial kink angle of 2^{o}. If the initial kink-angle is lower than 2^{o}, that would again increase the critical time threshold for the onset of catastrophic tertiary.

3.4.4.3.4 Buckling Model

When long-fiber composites are manufactured with care to ensure local imperfections that could be precursors to kink-bands are eliminated, global fiber waviness might still be unavoidable [Figure 59a]. In polymer matrix composites, there are many reasons for fiber waviness [62]:

- machine vibration during filament winding, especially when performed under low tension;
- using sheets or strips of material in a closed mould whose length is smaller than the sheet length;
- electrostatic repulsion of fibers not completely overcome by the application of agents that reduce such repulsion;
- disturbance caused by the application of resin, especially when the resin contains inhomogeneities; and
- non-uniform curing and cooling shrinkages.

In particular for NiAl-W composites produced by reactive infiltration, there could be W waviness due to:

- Non-uniform elastic constriction of W in the porous nickel-wire preform prior to infiltration;
- Inhomogeneous infiltration forces that are generated in the nickel preform upon infiltration; and
- Thermal mismatch stress induced elasto-plastic curvature upon cooling the composite from $1638^{o}C$ to room temperature.

At high temperatures, in a creeping-fiber/creeping-matrix system the matrix is typically much weaker than at lower temperatures. Hence upon the application of a global compressive stress to the composite, the wavy fibers can exhibit lateral deflections as the matrix is quite weak and offers less resistance to fiber bending. This bending of the fibers contributes to an increase in its curvature (with the radius of curvature actually decreasing from infinity when the fibers are straight) with deformation. As the deflected fibers have lower load carrying capacity than straight fibers, the composite is expected to become weaker with increasing strain. Qualitatively, the composite should thus exhibit increasing creep-rates with deformation for constant stress and temperature. Quantitatively, the extent and the rate of increase in creep-rate with deformation is a function of the actual and relative magnitudes of creep parameters (stress exponents and activation energies) of matrix and fiber; the test conditions (temperature and stress); the fiber volume fraction; the initial fiber geometry (alignment and curvature); the evolution of fiber

geometry with deformation. In this case, the fibers in the composite will deform gracefully by global buckling as opposed to local kinking. A simple model factoring all of the above parameters to predict strains and strain-rates with deformation under a constant uni-axial compressive stress is presents in what follows.

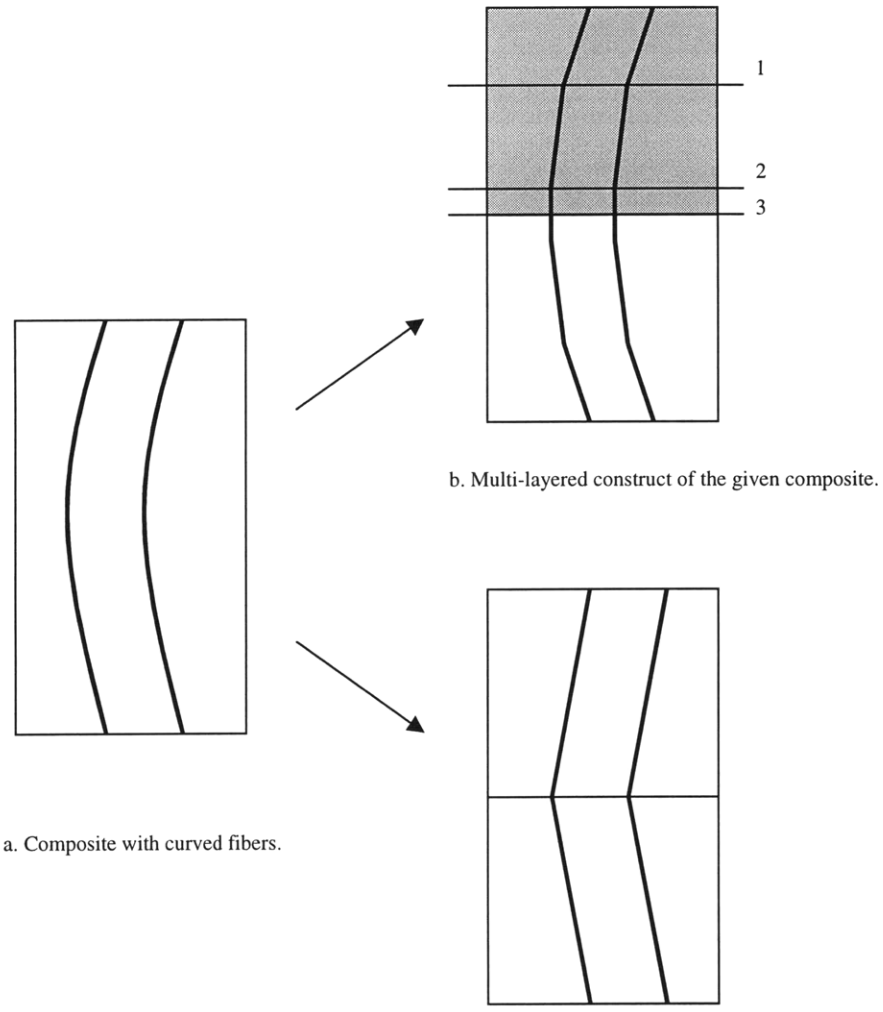

b. Multi-layered construct of the given composite.

a. Composite with curved fibers.

c. Bi-layered construct of the given composite.

Figure 59. Compressive creep modeling using bi-layered and multi-layered constructs.

A composite with buckled fibers can be treated in the most general case as a multi-layered composite [Figure 59b] or in the simplest case as a two-layered composite, each layer with fibers that are straight but mis-oriented with the loading direction [Figure 59c]. For the purpose of illustration, the latter case wherein the composite is envisioned as two diffuse kink-bands symmetric about the mid-section of the sample spanning the entire height of the sample, is investigated. Hence all of the assumptions that apply to the kink-band model apply to this buckling model as well.

The composite creep-rate is then given by Eq. [72]. The buckling model is then applied to a typical NiAl-W composite. The W fibers extracted from a typical NiAl-W composite by dissolving the matrix prior to creep testing exhibit curvatures that can be well approximated by two-layered composite model [Figure 70a]. The angles of mis-orientation range from < 1^{o} to about 2^{o} [Figure 70c]. Hence the error associated with using the two-layered composite model with a median mis-orientation angle of 1^{o} is expected to be small.

The relevant input parameters for this model are as indicated in Table 20. As expected the composite creep-rate increases with deformation [Figure 71, Figure 72] which is associated with fiber rotations within the kink-band [Figure 73, Figure 74]. The composite creep-strain obtained as a function of time [Figure 75, Figure 76] indicates the presence of a threshold strain which varies inversely with the volume fraction of fibers in the composite.

The buckling model predictions [Eq. 72] are compared to experiment A2f [Figure 77] wherein partial buckling of the fibers was observed [Figure 27]. Using an initial fiber mis-orientation of 1^{o}, it is thus possible to demonstrate reasonable agreement in creep-behavior of experiment with the model predictions [Figure 77].

Table 20. Input parameters used for the numerical analysis of the buckling model at 1025°C and under applied composite stresses of 80 and 120 MPa.

T [°C]	Stress [MPa]	v_f [%]	Time step [s]	Initial kink length [mm]	Initial kink angle [°]	Sample height [mm]	λ	μ	ν
1025	120	5	20	5	2	10	$2.2\ 10^{-5}$	$9.7\ 10^{-5}$	$1.9\ 10^{-4}$
		10	50	5	2	10	$9.8\ 10^{-6}$	$9.6\ 10^{-5}$	$1.8\ 10^{-4}$
		15	80	5	2	10	$5.7\ 10^{-6}$	$9.6\ 10^{-5}$	$1.9\ 10^{-4}$
		20	100	5	2	10	$3.7\ 10^{-6}$	$9.5\ 10^{-5}$	$1.9\ 10^{-4}$
	80	5	20	5	2	10	$2.1\ 10^{-5}$	$1\ 10^{-4}$	$2.1\ 10^{-4}$
		7	30	5	2	10	$1.5\ 10^{-5}$	$1\ 10^{-4}$	$2.1\ 10^{-4}$
		10	40	5	2	10	$9.8\ 10^{-6}$	$1\ 10^{-4}$	$2.1\ 10^{-4}$
		15	80	5	2	10	$5.6\ 10^{-6}$	$1\ 10^{-4}$	$2.1\ 10^{-4}$
		20	200	5	2	10	$3.7\ 10^{-6}$	$1\ 10^{-4}$	$2.1\ 10^{-4}$

The sensitivity of the composite strains to the initial mis-orientation of fibers is examined [Figure 78] and it is demonstrated that the sensitivity is low at lower composite strains and high at higher strain levels as indicated by the greater divergence in the creep behavior predicted for different starting conditions (i.e. fiber mis-orientations from 0.5^{o} to 4^{o}).

The evolution of fiber rotation with deformation in a NiAl-7 volume % W composite at 80 MPa is examined [Figure 79]. It is demonstrated that fibers with an initial mis-alignment of 1^{o} will rotate to attain a new orientation of 2^{o}.The actual experimental observation of the deformed fibers also indicate fiber rotations to approximately 2^{o} [Table 21] thus demonstrating reasonable agreement of the model predictions with the experimental results.

Table 21. Analysis of fiber orientations in experiment A2f tested at 1025°C and 80 MPa after 9% creep-strain was obtained.

Fiber	Angle [degree]	Fiber	Angle	Fiber	Angle
1	2	16	2.25	25	2.5
4	1	18	2	33	1.5
5	2	19	1.75	34	1
6	0.75	20	2.5	36	2
12	1.5	22	1	37	2.5
14	2	23	2.5	38	2
15	2	24	1.75	40	3
42	2.25				

Average fiber mis-orientation angle = 1.9°.
Of the 42 fibers recovered from the sample, 22 exhibited simple curvatures, 11 exhibited localized kinks, 5 exhibited double curvature. Four fibers that had been present at the surface of the sample had oxidized partially and thus the entire fibers could not be recovered and hence were not used for this analysis.

3.4.4.3.5 Limitations of the buckling model

- The model presented above approximates a composite with curved fibers as a bi-layered composite with fibers that are straight but misaligned and computes an upper bound to the steady-state strain-rates. A more accurate but computation-intensive analysis could be done following the multi-layered construct, by applying the same procedure to each layer and computing the average the strain-rate of each layer weighted by their corresponding length scales to obtain the composite creep-rate.

- The model assumes the fiber deformation to occur in one plane. However out-of-plane deformations have been observed and hence a 3-D approach would be required for a more accurate analysis.

- The initial fiber imperfection is taken to be symmetric about the mid-section of the sample so that fiber-deflections evolve in a symmetric manner with deformation; asymmetry in the initial fiber configuration needs to be addressed.

- The local matrix stresses generated by deflecting fibers [63] and their effects on the composite creep are assumed to be negligible.

- Processing induced residual stresses are assumed to decay quickly during sample pre-heating stage and hence their effects have also been ignored.

- Some of the W fibers have been observed to kink locally while others buckled globally. The buckling model presented here does not consider the effects of localized kinking.

- The primary creep component has also not been incorporated in this model.

3.4.4.3.6 Figures and illustrations

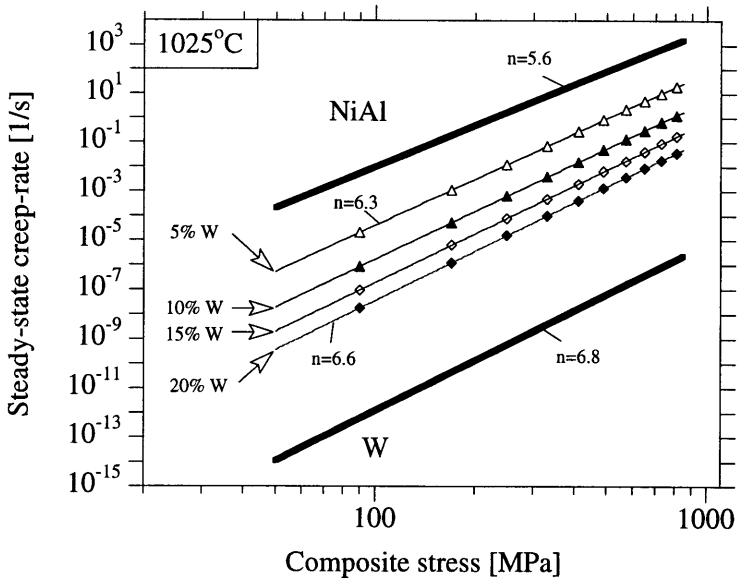

Figure 60. The 1025°C NiAl-W composite steady-state creep-rates described accurately by power-laws with different stress exponents corresponding to different volume fractions of W and within the stress-range 50 MPa and 850 MPa.

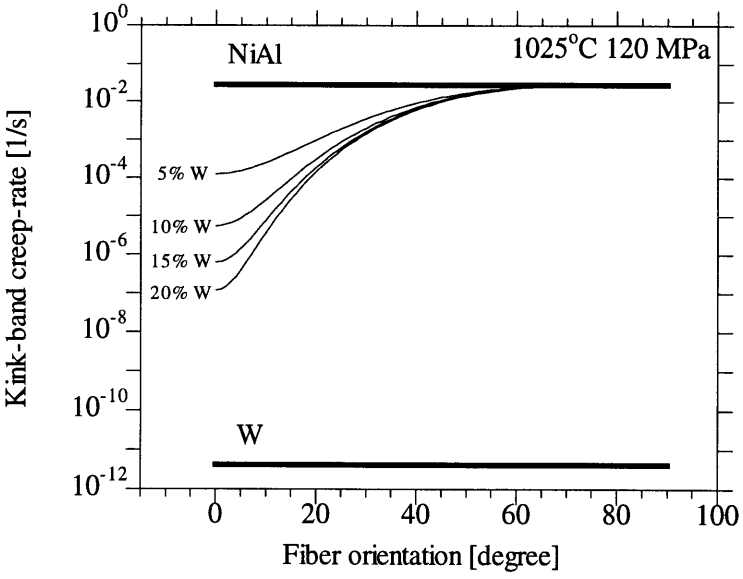

Figure 61. Variation of the kink-band creep-rate with fiber orientation with the loading direction at 1025°C, 120 MPa, and for varying volume fractions of W.

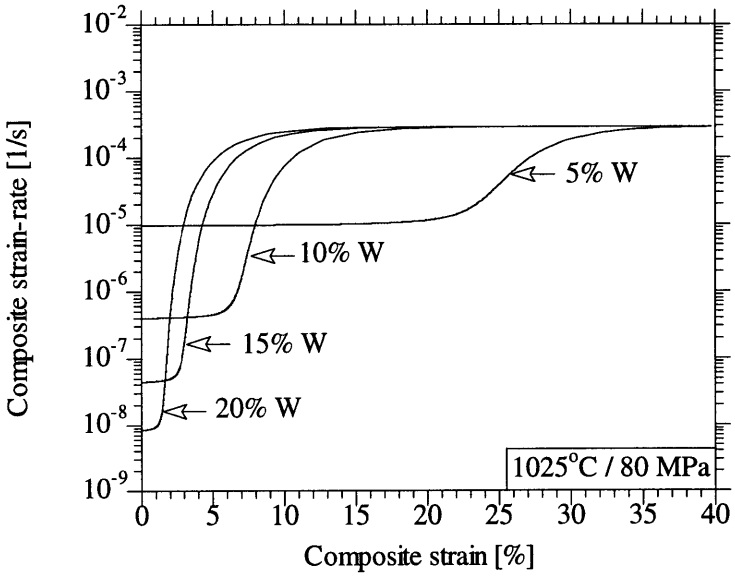

Figure 62. The tertiary kink-band model is applied to NiAl-W composites with an initial kink angle of 2° and an initial kink length of 2 mm to obtain composite strain-rates as functions of composite strains under an applied composite stress of 80 MPa.

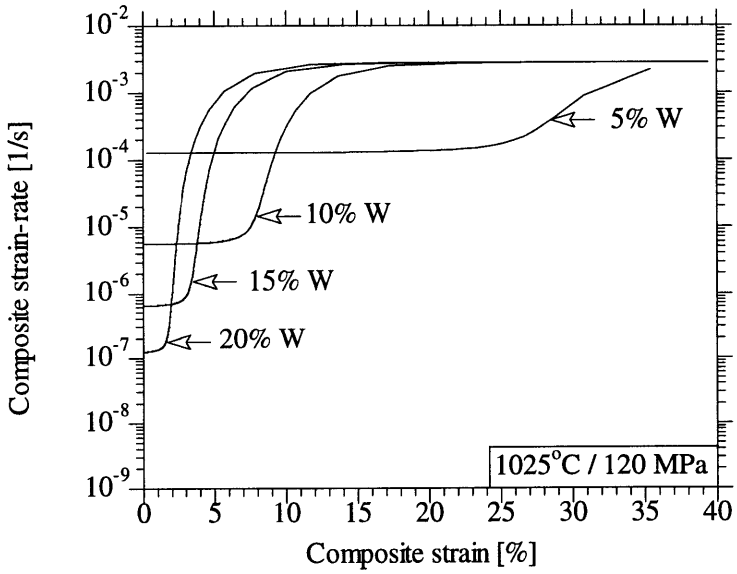

Figure 63. The tertiary kink-band model is applied to NiAl-W composites with an initial kink angle of 2° and an initial kink length of 2 mm to obtain composite strain-rates as functions of composite strains under an applied composite stress of 120 MPa.

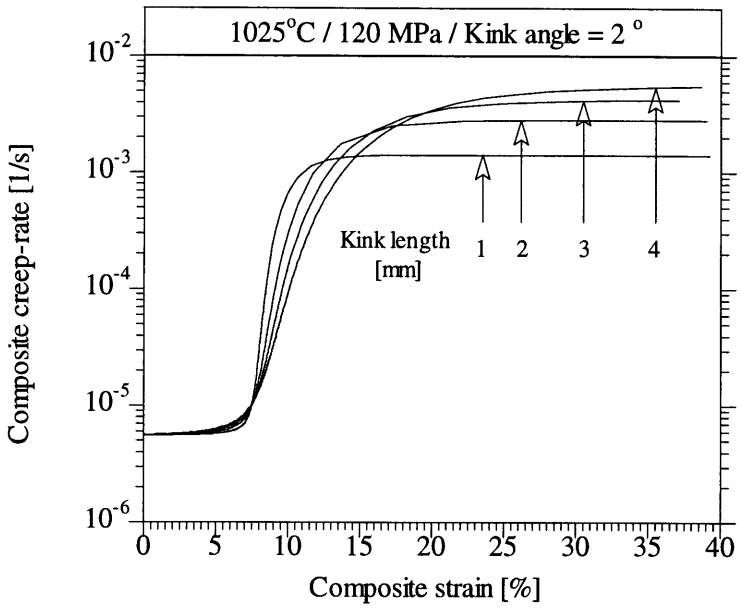

Figure 64. The tertiary kink-band model is applied to NiAl-10 volume % W composites with a constant initial kink angle of 2° but with different initial kink lengths to obtain composite strain-rates as functions of composite strains under an applied composite stress of 120 MPa.

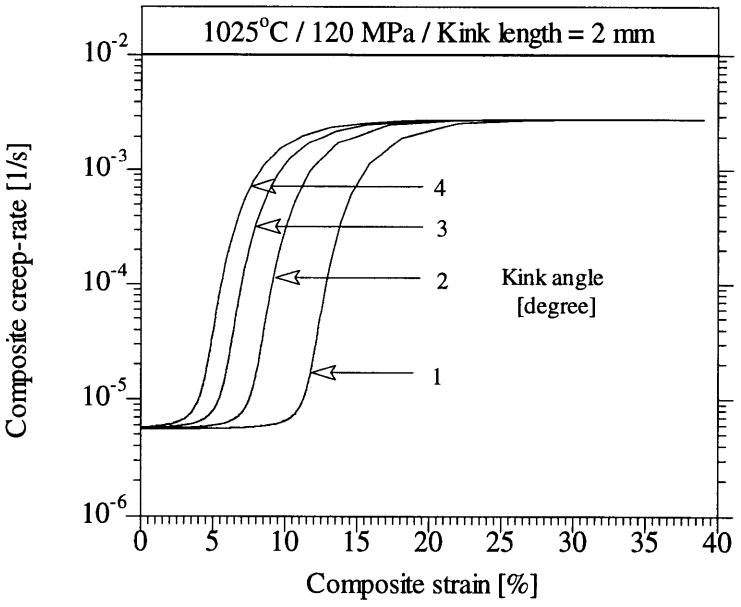

Figure 65. The tertiary kink-band model is applied to NiAl-10 volume % W composites with a constant initial kink length of 2 mm but with different initial kink angles to obtain composite strain-rates as functions of composite strains under an applied composite stress of 120 MPa.

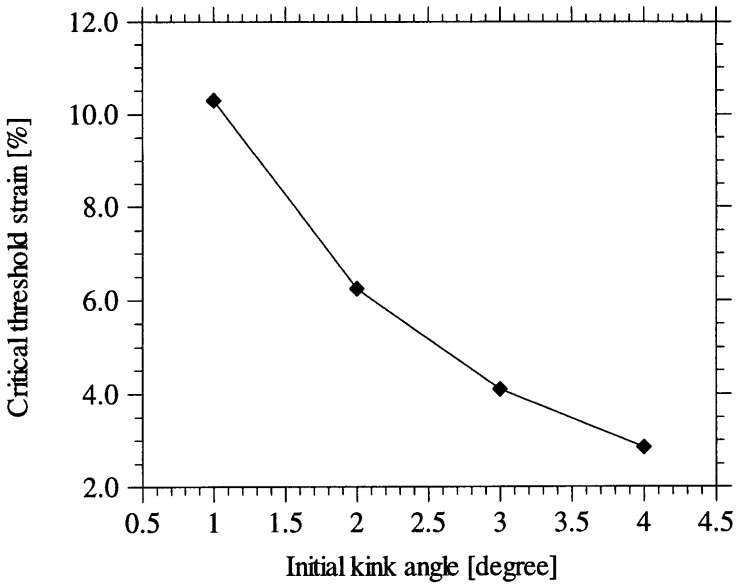

Figure 66. The tertiary kink-band model is applied to NiAl-10 volume % W composites with a constant initial kink length of 2 mm but with different initial kink angles to obtain critical threshold strains for the onset of tertiary as functions of initial kink angles under an applied composite stress of 120 MPa.

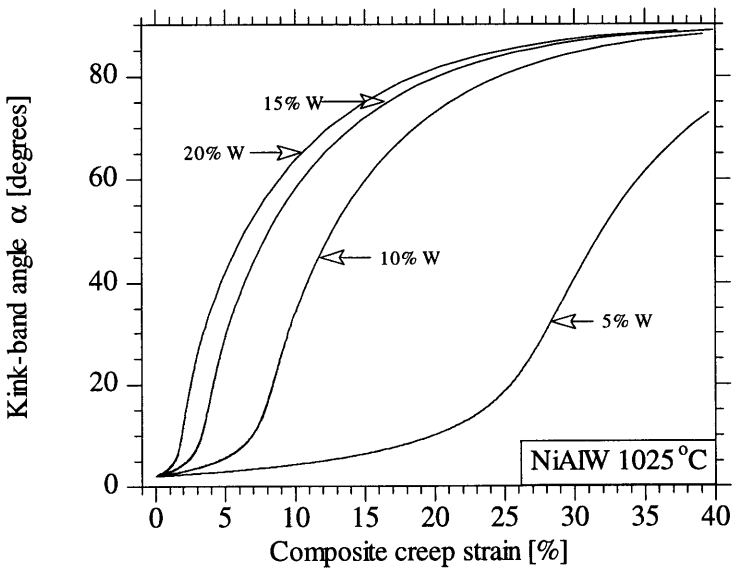

Figure 67. The tertiary kink-band model is applied to NiAl-W composites with an initial kink length of 2 mm and an initial kink angle of 2° to obtain kink-band angle as functions of composite strains under an applied composite stress of 120 MPa. The lower volume fraction composites exhibit lower levels of anisotropy and thus the changes in kink-band angles are gradual at lower composite strains.

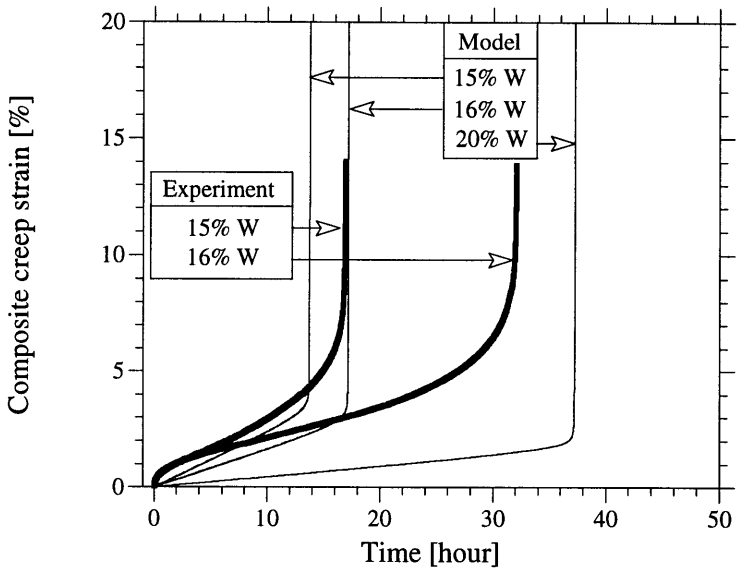

Figure 68. The composite creep behavior predicted by the tertiary kink-band model (exclusive of composite primary creep) is compared to experiments H1r and H2r and reasonable correlation between theory and experiments is demonstrated.

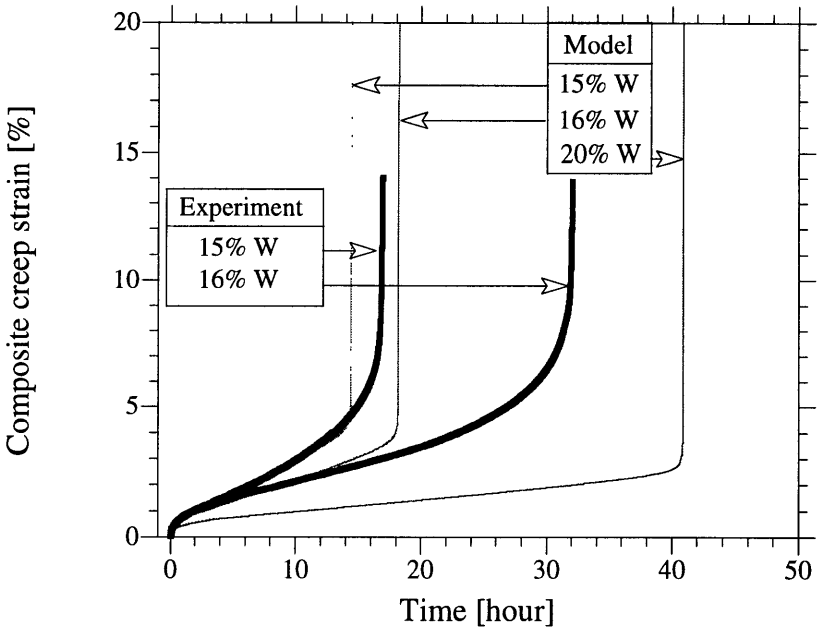

Figure 69. The composite creep behavior predicted by the tertiary kink-band model (inclusive of composite primary creep) is compared to experiments H1r and H2r and reasonable correlation between theory and experiments is demonstrated.

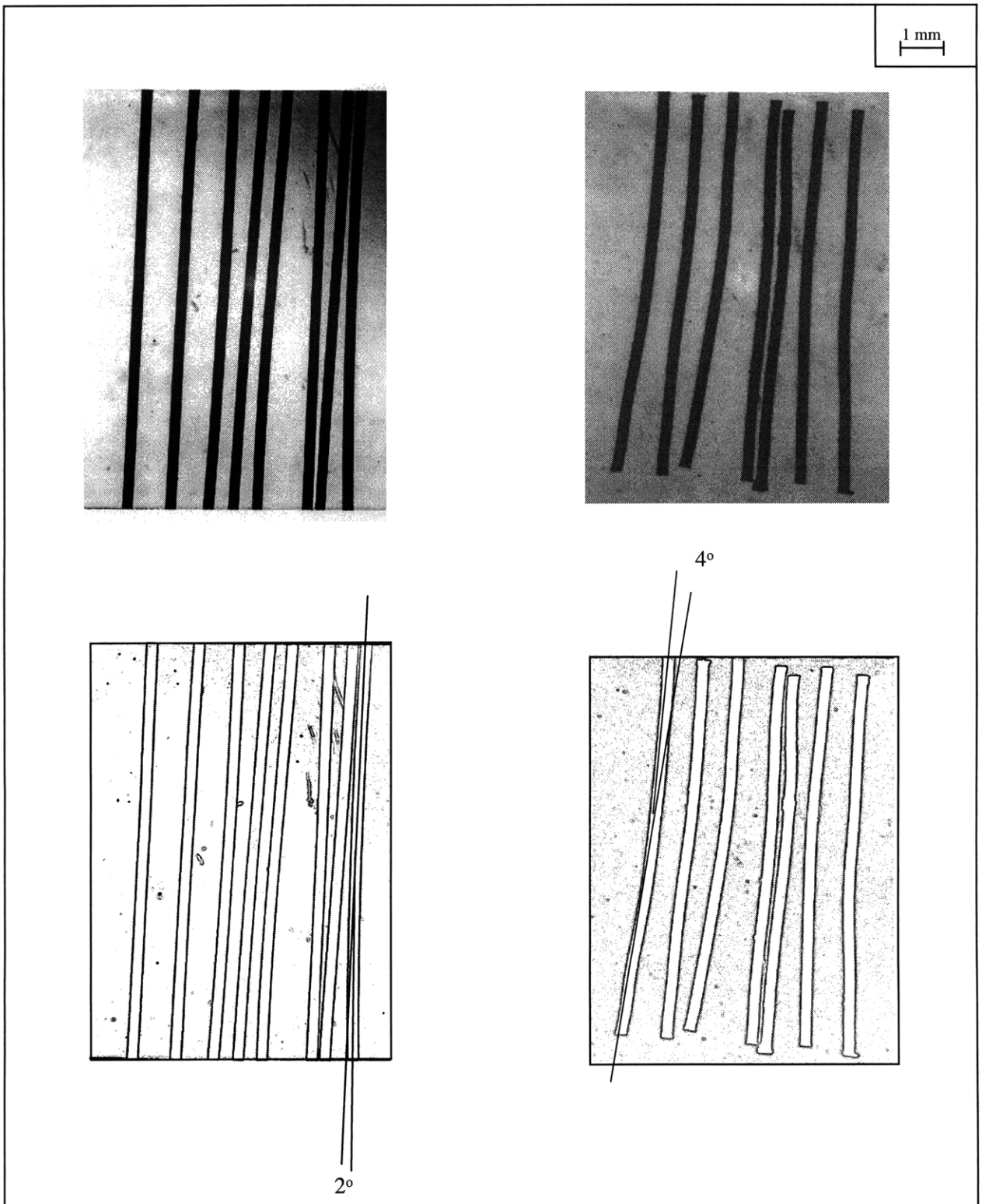

Figure 70. W fibers prior to creep testing (a,c) exhibiting small curvature with misorientation of approximately 2° (thus the orientation with the load axis is 1°)and the W fibers after creep testing (b, d) (A2f) exhibiting more pronounced mis-orientation of approximately 4° (thus the orientation with the load axis is 2°).

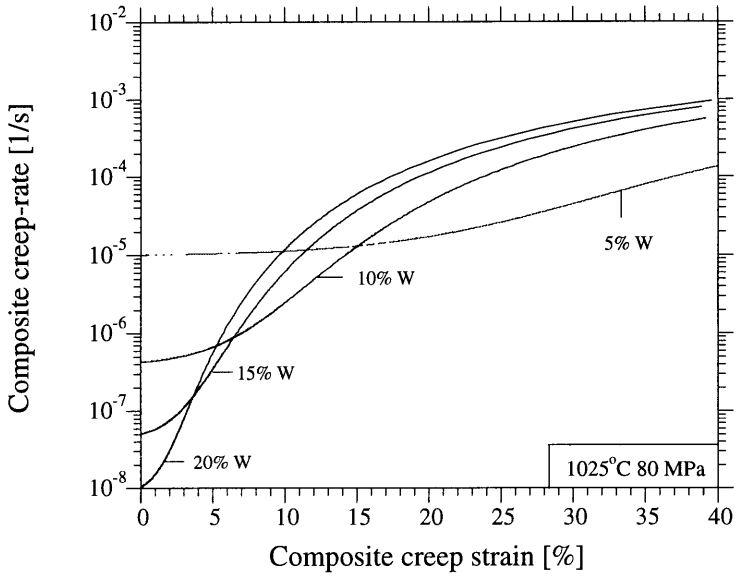

Figure 71. The buckling model is applied to a NiAl-W composite with varying volume fractions of W (for the case when the initial kink-angle is 2^{o}) at 1025^{o}C and an applied compressive stress of 80 MPa to obtain composite creep-rate as a function of composite creep strain.

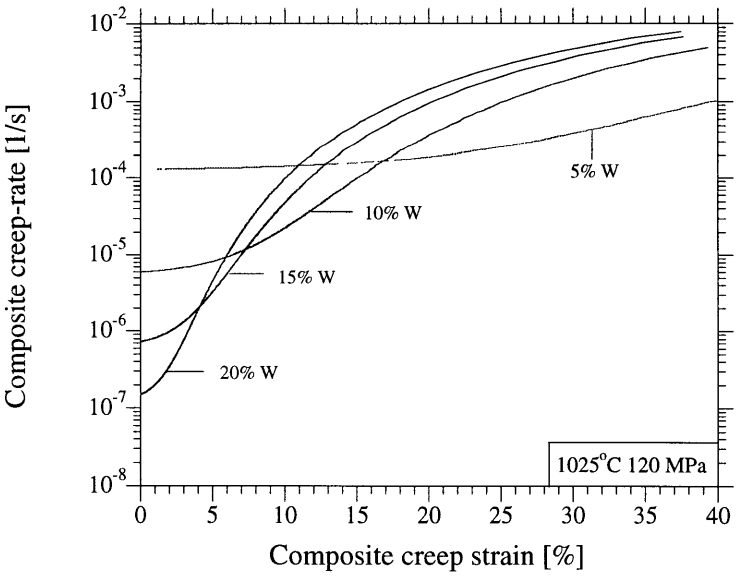

Figure 72. The buckling model is applied to a NiAl-W composite with varying volume fractions of W (for the case when the initial kink-angle is 2^{o}) at 1025^{o}C and an applied compressive stress of 120 MPa to obtain composite creep-rate as a function of composite creep-strain.

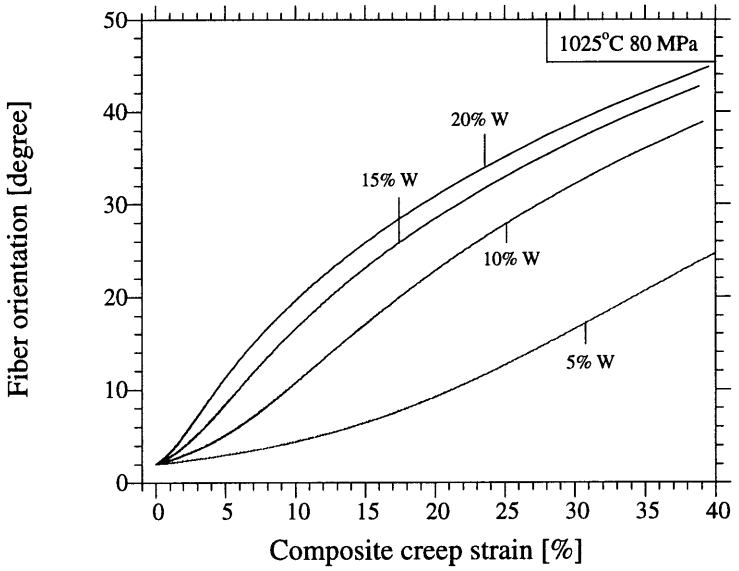

Figure 73. The buckling model is applied to a NiAl-W composite with varying volume fractions of W (for the case when the initial kink-angle is 2°) at 1025°C and an applied compressive stress of 80 MPa to obtain fiber orientation as a function of composite creep strain.

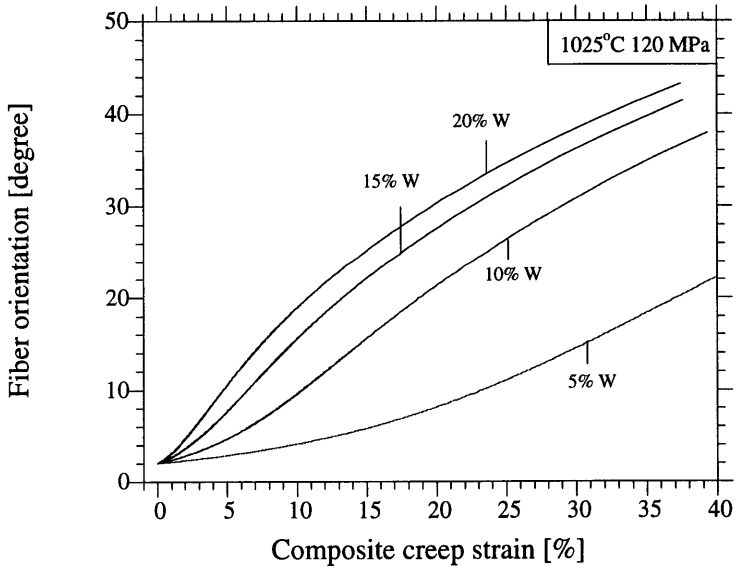

Figure 74. The buckling model is applied to a NiAl-W composite with varying volume fractions of W (for the case when the initial kink-angle is 2°) at 1025°C and an applied compressive stress of 120 MPa to obtain fiber orientation as a function of composite creep strain.

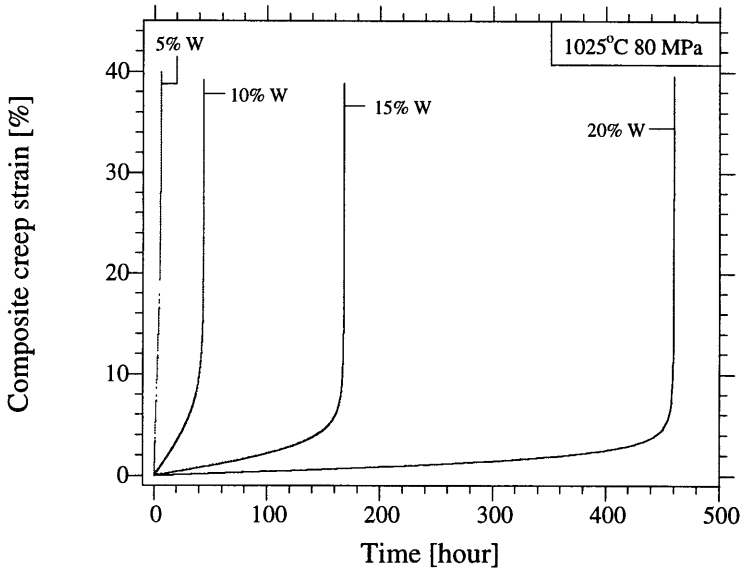

Figure 75. The buckling model is applied to a NiAl-W composite with varying volume fractions of W (for the case when the initial kink-angle is 2^{o}) at $1025^{o}C$ and an applied compressive stress of 80 MPa to obtain composite creep-strain as a function of time.

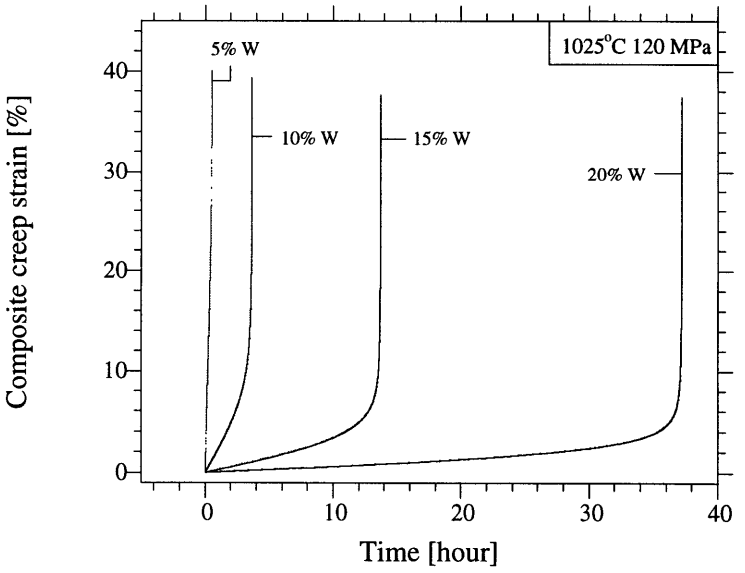

Figure 76. The buckling model is applied to a NiAl-W composite with varying volume fractions of W (for the case when the initial kink-angle is 2^{o}) at $1025^{o}C$ and an applied compressive stress of 120 MPa to obtain composite creep strain as a function of time.

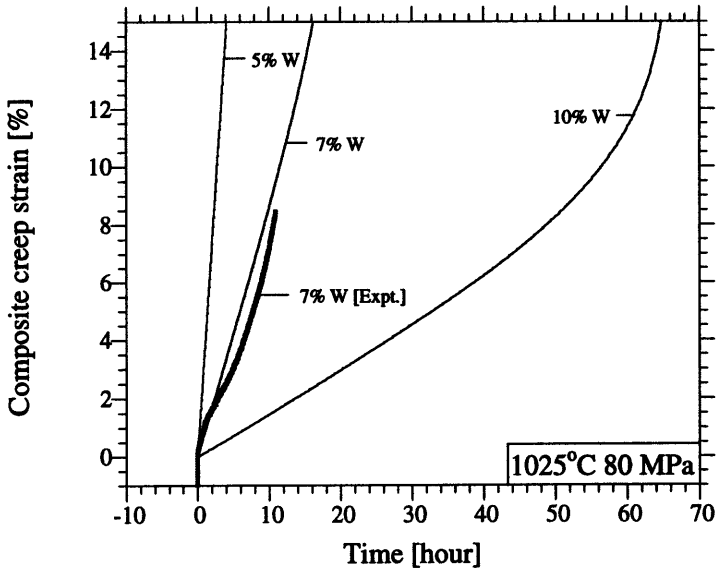

Figure 77. The composite creep behavior predicted by the tertiary buckling model is compared to experiment A2f and reasonable correlation between theory and experiment is demonstrated.

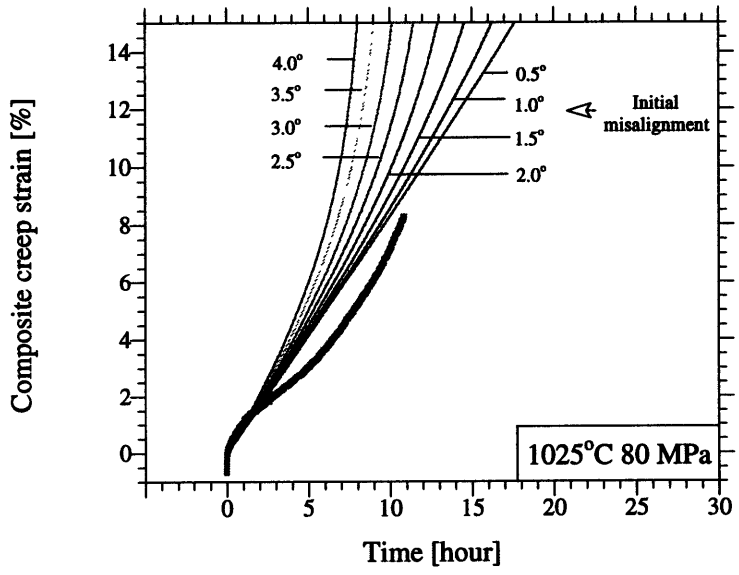

Figure 78. The sensitivity of the buckling model predictions to the initial fiber mis-orientations at 1025°C and 80 MPa is examined and it is demonstrated that the buckling model predictions tend to diverge at larger composite creep strains.

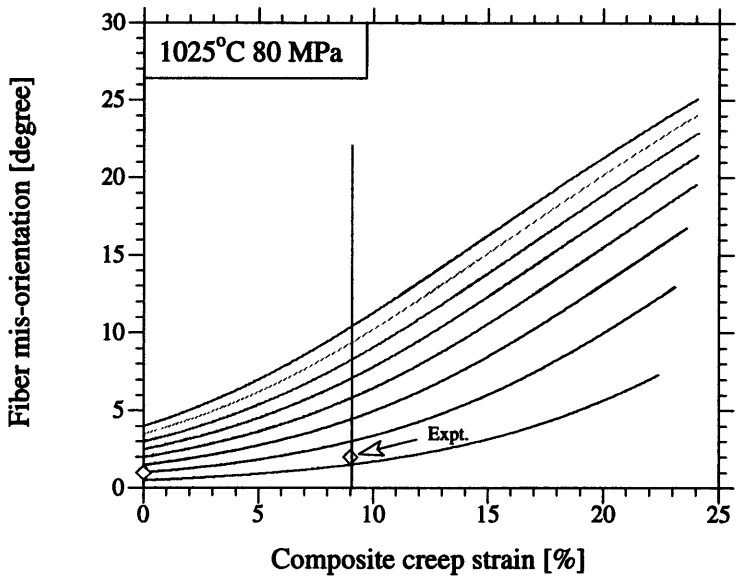

Figure 79. The evolution of fiber orientation with composite deformation is examined for different initial fiber mis-orientations ranging from 0.5° to 4° and compared to experiment A2f to demonstrate reasonable agreement with model predictions.

3.5 Conclusions

The high-temperature uni-axial compression creep behavior of uni-directional continuous fiber reinforced composite materials has been investigated using NiAl-W as a model system for the case where both the NiAl matrix and the W fiber undergo plastic deformation by creep.

- In the most general case, these composites exhibit classical three stage creep behavior with distinct primary, secondary, and tertiary stages, wherein the composite creep-rate decreases monotonically, remains constant, and increases rapidly during the primary, secondary, and tertiary stages, respectively.

- The composite primary creep stage is characterized by load-transfer from the weaker phase (matrix) to the stronger phase (fiber) and by the respective primary creep of both the fiber and the matrix. A simple physical model that has been developed predicts composite primary creep strains to be significant at high applied composite stresses and for composites with high volume fractions of fibers. The composite primary time is uniquely related to the composite steady-state creep-rate by a power-law at a given temperature and for a limited stress-range investigated. Good correlation between the primary creep model predictions and experiments is obtained when the observed composite steady-state creep behavior converges to the steady-state derived originally by McLean, for tension.

- The composite secondary creep stage is characterized by stable steady-state creep of matrix and fiber at their respective steady-state stresses. Reasonable correlation exists between experiments and the McLean model.

- The composite tertiary creep stage is characterized by fiber deformations away from the loading axis. Brooming and bulging are typically characterized by axi-symmetric fiber rotations while buckling and kinking are typically characterized by in-plane fiber deflections. A simple kink-band model developed here predicts the critical threshold strain for the onset of tertiary stage to be most sensitive to the initial kink angles while being relatively insensitive to the initial kink-band heights and varies inversely with the volume fraction of fiber in the composites. By extension of the kink-band model, effects of fiber buckling have also been examined. Reasonable correlation between the model and experiments is obtained when the observed composite steady-state correlates well with the McLean steady-state.

- The models developed here capture the physics of the compressive creep behavior in a qualitative manner by using many simplifying assumptions. Hence the model predictions are approximate in nature and thus in most cases only reasonable correlation with experiments is obtained.

4 SUMMARY OF MAIN CONTRIBUTIONS

Using a combination of theoretical, numerical, and experimental methods, this thesis investigated:

- reactive infiltration processing of the intermetallic NiAl and its composites; and
- the compression creep behavior of unidirectional long-fiber composites using NiAl-W as a model system.

The highlights of the investigation on reactive infiltration processing are:

- First successful demonstration of the fabrication of dense, monolithic NiAl from nickel wire-preforms on a reasonable size-scale that exhibited creep properties as good as those of NiAl fabricated by conventional casting techniques.
- First successful demonstration of the fabrication of NiAl-low volume fraction long-fiber W composites with W recrystallization levels lower than that obtained through conventional processing of NiAl-W composites.
- Demonstration that it is kinetically near impossible to fabricate NiAl-low volume fraction fine Mo particulate composites.

The highlights of the investigation on the compression creep behavior of NiAl-W long-fiber composites are:

- Development and experimental verification of a continuum level mechanical model that accounts for load-transfer across, and primary creep of, the fiber and the matrix, to describe and predict primary creep of the composite.
- Application and experimental verification of existing rule of mixtures McLean model that describes composite steady-state strain-rates under tensile stresses to the case with a compressive state of stress.
- Development and experimental verification of a continuum level mechanical model to describe kinking and buckling of creeping fibers within a creeping matrix and thus the tertiary creep of the composite under compressive stresses.

5 SUGGESTIONS FOR FUTURE WORK

- The reactive infiltration process can be modified to correct for the mis-alignment problem in the NiAl-sapphire system.

- Fabrication of NiAl and its composites from nickel-wire preforms could be tried out on a larger scale to check for feasibility of industrial production.

- An extensive modeling effort could help understand the thermodynamics and kinetics of the process and thus solve the macrosegregation problem.

- The Johnson model which is used in developing the tertiary creep model, is strictly valid for a transversely isotropic material which displays a stress exponent that is invariant with the orientation of the material to the stress axis. In long-fiber composites, in the most general case, the stress-exponents are expected to be different in the longitudinal and transverse directions. Hence the Johnson model needs to be modified to account for this anisotropy.

- A more accurate tertiary creep model could be derived by considering the effects of bending moments as the kink-band rotates during the tertiary stage.

- A full-scale 3-D finite element modeling taking into account the exact fiber geometries of all of the fibers in a given composite sample, factoring frictional as well as constraint effects at the ends of the samples would be able to generate exact solutions that can then be compared to the analytical solutions.

- The finite element modeling could then be extended to investigate high-volume fraction composites by taking inter-fiber interactions into account.

- While reasonable correlation between theory and experiments has been demonstrated in this thesis using the NiAl-W system which exhibits complexities such as W recrystallization, investigations on other simpler metal matrix composite systems such as the Cu-W system would help validate the primary and tertiary creep models with more accuracy.

- Creep testing of W fiber composites (NiAl-W or Cu-W) in an inert or reducing atmosphere is recommended as this would prevent oxidation of W and thus preserve the volume fraction of W in the composite and thereby reduce errors and ambiguities in determining volume fractions.

6 APPENDICES

6.1 Primary Creep Model – Program Listing

This program tracks the evolution of stresses in fiber and matrix upon loading. Assuming the fiber has a primary that follows a 1/3rd time law, the pseudo-primary of the composite is captured. Convergence with McLean steady-state at long-times is also observed. T=1025C

MATRIX AND FIBER PROPERTIES

$ENiAl := 128000$

$EW := 366000$

$km := 6.37 \cdot 10^{-14}$

$kf := 3.48 \cdot 10^{-26}$

$nm := 5.6$

$nf := 6.77$

$vf := .05$

$Total\_time := 1\ hours$

COMPOSITE STRESS

$\sigma_0 := 120$

CALCULATION OF McLEAN STEADY-STATE

$n := 15$

$i := 0..n$

$\varepsilon_i := \frac{i}{100}$

$A_i := \frac{A_0}{1 - \varepsilon_i}$

$\sigma_i := \sigma_0 \cdot (1 - \varepsilon_i)$

$edt := 1 \cdot 10^{-9}$ (Guess Value)

Given

$$\sigma = vf \cdot \left(\frac{edt}{kf}\right)^{\frac{1}{nf}} + (1 - vf) \cdot \left(\frac{edt}{km}\right)^{\left(\frac{1}{nm}\right)}$$

$edot(\sigma) := Find(edt)$

$edot_i := edot(\sigma_i)$

$edot_0 = 1.268 \cdot 10^{-4}$

$$\sigma ssW := \left(\frac{edot_0}{kf}\right)^{\frac{1}{nf}}$$

$$\sigma ssNiAl := \left(\frac{edot_0}{km}\right)^{\frac{1}{nm}}$$

$\sigma ssW = 1.53053 \cdot 10^{3}$

$\sigma ssNiAl = 45.762$

ELASTIC STATE UPON LOADING

$\sigma comp := \sigma_0$

$$\sigma W := \frac{\sigma comp}{\left[vf + \frac{ENiAl}{EW} \cdot (1 - vf)\right]}$$

$$\sigma NiAl := \sigma W \cdot \left(\frac{ENiAl}{EW}\right)$$

$\sigma W = 313.939$

$\sigma NiAl = 109.793$

$vm := (1 - vf)$

$y_0 := \sigma W$

$p_0 := -0.0002824$

$p_1 := 8.6417 \cdot 10^{-7}$

$$D(t,y) := \frac{\left[km \cdot \left(\frac{\sigma_0 - vf \cdot y_0}{vm}\right)^{nm} - kf \cdot (y_0)^{nf} - \frac{1}{3} \cdot \left[p_0 + p_1 \cdot (y_0)\right] \cdot t^{-\frac{2}{3}}\right]}{\frac{1}{EW} + \frac{vf}{vm} \cdot \frac{1}{ENiAl}}$$

$Z := Rkadapt(y, 0.001, Total\_time \cdot 3600, Total\_time \cdot 3600 \cdot 3, D)$

$i := 1 .. rows(Z) - 1$

$rows(Z) = 1.08 \cdot 10^{4}$

FIBER ELASTIC RATE DETERMINATION

$$fiberelasticrate_i := \frac{1}{EW} \cdot \frac{Z_{i,1} - Z_{i-1,1}}{Z_{i,0} - Z_{i-1,0}}$$

FIBER PLASTIC RATE DETERMINATION

$i := 1 .. rows(Z) - 1$

$q1_i := p_0 + p_1 \cdot (Z_{i,1})$

$q1_1 = 5.017 \cdot 10^{-4}$

$$fiberprimaryplasticrate_i := \frac{1}{3}\cdot q1_i \cdot \left(Z_{i,0}\right)^{-\frac{2}{3}}$$

$$fiberprimaryplasticrate_1 = 3.471\cdot 10^{-4}$$

$$fibersecondaryplasticrate_i := kf\cdot \left(Z_{i,1}\right)^{nf}$$

$$fibersecondaryplasticrate_1 = 3.678\cdot 10^{-6}$$

$$fiberplasticrate_i := fiberprimaryplasticrate_i + fibersecondaryplasticrate_i$$

$i := 1.. rows(Z) - 1$

$$checkvector_i := fiberprimaryplasticrate_i - fibersecondaryplasticrate_i$$

$tav(checkvector, thres) :=$ | $j \leftarrow 1$ | while $checkvector_j > thres$ | $j \leftarrow j + 1$ | $j - 1$

$flag1 := tav(checkvector, 0)$

$flag1 = 21$

FIBER CREEP RATE DETERMINATION

$$fibercreeprate_i := fiberelasticrate_i + fiberplasticrate_i$$

FIBER CREEP DETERMINATION

$$fibercreep_0 := \frac{Z_{0,1}}{EW}$$

$$fibercreep_1 := Z_{1,0}\cdot fibercreeprate_1 + fibercreep_0$$

$i := 2.. rows(Z) - 1$

$$fibercreep_i := fibercreep_{i-1} + \left(Z_{i,0} - Z_{i-1,0}\right)\cdot fibercreeprate_i + \frac{1}{2}\cdot\left(Z_{i,0} - Z_{i-1,0}\right)\cdot\left(fibercreeprate_{i-1} - fibercreeprate_i\right)$$

$n := 10$

$$j := 1.. \frac{rows(Z) - 1}{n}$$

$x_j := Z_{n\cdot j,0}$

$y2_j := fibercreeprate_{n\cdot j}$

$y1_j := Z_{n\cdot j,1}$

FILEOUTPUT

$PRNPRECISION := 8$

$PRNCOLWIDTH := 40$

$rows(Z) = 10801$

$w := 10$

$$ub := floor\left(\frac{rows(Z) - 1}{w}\right)$$

$ub = 1.08\cdot 10^3$

$i := 0.. ub$

$FiberResult_{i,0} := Z_{w\cdot i,0}$

$FiberResult_{i,1} := fiberelasticrate_{w\cdot i}$

$FiberResult_{i,2} := fiberplasticrate_{w\cdot i}$

$FiberResult_{i,3} := fibercreeprate_{w\cdot i}$

$FiberResult_{i,4} := fibercreep_{w\cdot i}$

$fibercreep_{flag1} = 6.26907 \cdot 10^{-3}$

$FiberResult_{i,5} := Z_{w\cdot i,1}$

$Z_{flag1,0} = 7.00100$

$fibercreeprate_{flag1} = 2.06 \cdot 10^{-4}$

$$FiberResult_{i,6} := \frac{\sigma_0 - vf \cdot Z_{w\cdot i,1}}{vm}$$

$FiberResult_{i,7} := fiberprimaryplasticrate_{w\cdot i}$

$FiberResult_{i,8} := fibersecondaryplasticrate_{w\cdot i}$

WRITEPRN (thesis_1025_120mpa_05vf _1)

6.2 Tertiary Kink-Band Model – Program Listing

This program assumes:

- T=1025C
- a given fiber misalignment..only one slice symmetric about midsection of sample.
- locates new fiber orientation by considering Johnson model.
- computes composite creep rate (weighted sum of the kinked and the unkinked) as a function of strain
- calculates actual length of fiber in the fiber direction due to fiber creep and thus determines the level of rotation of the fiber for the next iteration.

```
sigma[comp]:= 80:
Temperature:=1025:
v[f]:=0.10:
l[kink]:=5:
l[sample]:=05:
misalignment:=1.0:
time_step:=40:
strainlimit:=0.40:

if v[f]=0.05 then n[comp]:=6.25: fi:
if v[f]=0.10 then n[comp]:=6.47: fi:
if v[f]=0.15 then n[comp]:=6.57: fi:
if v[f]=0.20 then n[comp]:=6.63: fi:
if v[f]=0.17 then n[comp]:=6.60: fi:
if v[f]=0.07 then n[comp]:=6.36: fi:

g:=100000:

strain:=array(1..g):
sample_strain:=array(0..g):
```

```
ao:=array(1..g):
y_o:=array(1..g):

phi:=array(1..g+1):
t:=array(1..g):
edot[kink]:=array(1..g):
F[kink]:=array(1..g):
edot[comp]:=array(1..g):
edot[unkink]:=array(1..g):
edot[fparallel]:=array(1..g):

l[unkink]:=l[sample]-(l[kink]/cos(misalignment*Pi/180)):

if Temperature=1025 then

n[m]:=5.6:
k[m]:=6.37e-14:
n[f]:=6.77:
k[f]:=3.48e-26:

elif Temperature=715 then

n[m]:=5.49:
k[m]:=1.74e-18:
n[f]:=13.56:
k[f]:=3.83e-49:
fi:

phi[1]:= evalf(misalignment/180*Pi):

edot[matrix]:=k[m]*(sigma[comp])^n[m]:

edot[unkink]:= fsolve( (v[f]*(edt/k[f])^(1/n[f])  + (1-v[f])*(edt/k[m])^(1/n[m]) = sigma[comp] ), edt=0..1    ):

lambda:= (edot[unkink]/sigma[comp]^n[comp])^(2/(n[comp]+1)):
mu:= (edot[matrix]/sigma[comp]^n[comp])^(2/(n[comp]+1)):
edot[fit]:=edot[matrix]:
angle:=89:
nu:=( (edot[fit]/sigma[comp]^n[comp])^(2/(n[comp]+1)) - lambda*(cos(angle*Pi/180))^4 -
mu*(sin(angle*Pi/180))^4 )/ ( ((cos(angle*Pi/180))^2)*(sin(angle*Pi/180))^2 ):


y_o[1]:=l[kink]:
ao[1]:=y_o[1]/cos(evalf(misalignment/180*Pi)):

sample_strain[1]:=0:
strain[1]:=0:
j:=1:
t[1]:=0:

while sample_strain[j]<= strainlimit
do

F[kink][j]:=evalf(lambda*(cos(phi[j]))^4 + (nu-lambda)*((sin(phi[j]))^2)*((cos(phi[j]))^2) + mu*(sin(phi[j]))^4):

edot[kink][j]:= evalf( ((F[kink][j])^((n[comp]+1)/2))*(sigma[comp])^n[comp] ):
```

```
edot[comp][j]:= evalf( (l[kink]*edot[kink][j] + l[unkink]*edot[unkink])/l[sample] ):

edot[fparallel][j]:=evalf( (( F[kink][j]*(sigma[comp]^2) )^( (n[comp]-1)/2 ) )*sigma[comp]*( -
0.5*lambda*(sin(phi[j]))^2 + lambda*(cos(phi[j]))^2 )):

if edot[comp][j]>1e-5 then time_step:=5: fi:

l_new:=ao[j]*(1-edot[fparallel][j]*time_step):
y_new:=y_o[j]*(1-edot[kink][j]*time_step):

phi[j+1]:=arccos(y_new/l_new):

ao[j+1]:=l_new:
y_o[j+1]:=y_new:

strain[j+1]:=edot[comp][j]*time_step:
sample_strain[j+1]:=sample_strain[j]+strain[j+1]:
t[j+1]:=t[j] + 0.5*(sample_strain[j+1]-sample_strain[j])*(1/edot[comp][j]+1/edot[comp][j+1]):
j:=j+1
od:

w:=7:
Result:=array(1..trunc((j-1)/w), 1..6):

for i from 1 to trunc((j-1)/w)

do

Result[i,1]:=sample_strain[w*i]:
Result[i,2]:=edot[comp][w*i]:
Result[i,3]:=edot[kink][w*i]:
Result[i,4]:=edot[fparallel][w*i]:
Result[i,5]:=evalf(phi[w*i]/Pi*180):
Result[i,6]:=t[w*i]:

od:

filename:=`./MODEL/DATAOUT/JOHNSON/JK4_19`:

writedata(filename, Result):
```

7 REFERENCES

1. Westbrook, J.H., *Historical sketch*, in *Intermetallic Compounds*. 1967, Wiley: New York.
2. Miracle, D.B., *The physical and mechanical properties of NiAl.* Acta Metall. et Mater., 1993. **41**: p. 649-684.
3. Noebe, R.D., R.R. Bowman, and M.V. Nathal, *Physical and mechanical properties of the B2 compound NiAl.* International Materials Reviews, 1993. **38**: p. 193-232.
4. Dimiduk, D.M., D.B. Miracle, and C.H. Ward, *Development of intermetallic materials for aerospace systems.* Materials Science and Technology, 1992. **8**: p. 367-375.
5. Stoloff, N.S., *Toughening mechanisms in intermetallics.* Metallurgical Transactions A, 1993. **24**: p. 561-567.
6. Essock, D.M., *Continuous tungsten fiber MMCs*, in *Composites*, T.J. Reinhart, Editor, ASM: Metals Park. p. 878-888.
7. Euler, L., *Methodus inveniendi lineas curvas maximi minimive proprietate gaudentes - Appendix I.* De curvis elasticis, 1744.
8. Gere, J.M., *Mechanics of Materials*. 1984, Boston: PWS-KENT.
9. Rosen, B.W., *Mechanics of composite strengthening*, in *Fiber Composite Materials*. 1965, ASM: Ohio. p. 37-75.
10. Lager, J.R. and R.R. June, *Compressive strength of boron-epoxy composites.* Journal of Composite Materials, 1969. **3**: p. 48-56.
11. Waas, A.M. and C.R. Schultheisz, *Compressive failure of composites, Part II: Experimental studies.* Progress in Aerospace Science, 1996. **32**: p. 43-78.
12. Argon, A.S., *Fracture of composites*, in *Treatise on Materials Science and Technology*. 1972, Academic Press: New York. p. 79-114.
13. Budiansky, B., *Micromechanics.* Computers and Structures, 1983. **16**(1-4): p. 3-12.
14. Budiansky, B. and N.A. Fleck, *Compressive failure of fiber composites.* Journal of the Mechanics and Physics of Solids, 1993. **41**: p. 183-211.
15. Kyriakides, S., *et al.*, *On the compressive failure of fiber reinforced composites.* International Journal of Solids and Structures, 1993. **32**(6/7): p. 689-738.
16. Moran, P.M., X.H. Liu, and C.F. Shih, *Kink band formation and band broadening in fiber composites under compressive loading.* Acta Metallurgica et Materialia, 1995. **43**(8): p. 2943-2958.
17. Schultheisz, C.R. and A.M. Waas, *Composite failure of composites, Part I: Testing and micromechanical theories.* Progress in Aerospace Science, 1996. **32**: p. 1-42.
18. Noebe, R.D., *et al.*, *Propects for ductility and toughness enhancement by ductile phase reinforcement.* ISIJ, 1991. **31**: p. 1172-1200.
19. Munir, Z.H. and U. Anselmi-Tamburini, *Self-propagating exothermic reactions: The synthesis of high-temperature materials by combustion.* Materials Science Reports, 1989. **3**: p. 277-365.
20. Alman, D.E. and N.S. Stoloff, *Powder fabrication of monolithic and composite NiAl.* International Journal of Powder Metallurgy, 1991. **27**(1): p. 29-41.
21. Munir, Z.A. *Microstructural and mechanistic analyses of SHS systems.* in *1992 Powder Metallurgy World Congress.* 1992. San Francisco: Metal Powder Industries Federation, American Powder Metallurgy Institute, Princeton, NJ.
22. Chen, H., M. Kaya, and R.W. Smith, *Near net-shape long fiber reinforced intermetallic matrix composites produced by reactive infiltration process.* Materials Letters, 1992. **13**(4-5): p. 180-183.
23. Suganuma, K., *Simple fabrication process of intermetallic compounds utilizing low-temperature pressure casting of aluminum.* Materials Letters, 1993. **16**(1): p. 22-25.
24. Dunand, D.C., J.L. Sommer, and A. Mortensen, *Synthesis of Bulk and Reinforced Nickel Aluminides by Reactive Infiltration.* Metallurgical Transactions, 1993. **24A**(10): p. 2161-2170.
25. Dunand, D.C., J.L. Sommer, and A. Mortensen. *Reactive infiltration of nickel preforms with molten aluminum.* in *Processing and Fabrication of Advanced Materials for High-Temperature Applications II.* 1993: p. 635-646, TMS, Warrendale, PA.
26. Dunand, D.C. *Reactive Synthesis of Aluminide Intermetallics.* in *Processing and Fabrication of Advanced Materials III.* 1994. p. 771-793, Pittsburgh: TMS, Warrendale, PA.

27. Dunand, D.C., *NiAl Formation by Annealing of Infiltrated Aluminium-Nickel Precursors.* Journal of Materials Science, 1994. **29**: p. 4056-4060.
28. Dunand, D.C., *Reactive synthesis of aluminide intermetallics.* Materials and Manufacturing Processes, 1995. **10**: p. 373-403.
29. Isaacs, J.A., *et al.*, *Chemical stability of zirconia-stabilized alumina fibers during pressure infiltration by aluminum.* Metallurgical Transactions, 1991. **22A**: p. 2855-2862.
30. SanMarchi, C.W., *Processing of aluminum-nickel intermetallics by reactive infiltration*, in *Materials Science and Engineering*. 1997, Massachusetts Institute of Technology: Cambridge, MA.
31. Venkatesh, T.A., *et al. Reactive infiltration processing of bulk and fiber-reinforced NiAl.* in *High temperature ordered intermetallic alloys*. 1997. p. 737-742, Boston: Materials Research Society.
32. SanMarchi, C.W. and A. Mortensen, *Reactive infiltration processing of aluminum-nickel intermetallic compounds.* Metallurgical Transactions, 1997: *in print.*
33. Kubachewski, O., *Aluminum-Molybdenum-Nickel*, in *Ternary alloys - A comprehensive compendium of evaluated constitutional data and phase diagrams*, G. Petzow and G. Effenberg, Editors. 1993. p. 199-218.
34. Alkaseeva, Z.M., *Aluminum-Nickel-Tungsten*, in *Ternary alloys - A comprehensive compendium of evaluated constitutional data and phase diagrams*, G. Petzow and G. Effenberg, Editors. 1993. p. 49-57.
35. Nourbakhsh, S., F.L. Liang, and H. Margolin, *Fabrication of a Ni_3Al/Al_2O_3 unidirectional composite by pressure casting.* Advanced Materials and Manufacturing Processes, 1988. **3**(1): p. 57-78.
36. Nash, P., M.F. Singleton, and J.L. Murray, *Al-Ni*, in *Phase Diagrams of Binary Nickel Alloys*, P. Nash, Editor. 1991, ASM: Materials Park. p. 3-11.
37. Darolia, R., *NiAl alloys for high temperature structural applications.* Journal of Materials, 1991(March): p. 44-49.
38. Lowell, C.E., C.A. Barrett, and J.D. Whittenberger. *Cyclic oxidation resistance of a reaction-milled NiAl-AlN composite.* in *Intermetallic matrix composites*. 1990. p. 355-360, San Francisco, CA: Materials Research Society.
39. Polvani, R.S., W.S. Tzeng, and P.R. Strutt, *High temperature creep in a semi-coherent NiAl-Ni_2AlTi alloy.* Metallurgical Transactions, 1976. **7A**: p. 33-40.
40. Reuss, S. and H. Vehoff. . in *High temperature ordered aluminides and intermetallics*. 1990: The Minerals, Metals, and Materials Society.
41. Chawla, K.K., *Composite Materials*. 1987, New York: Springer Verlag.
42. McLean, M., *Mechanical Behavior of In-Situ Composites*. 1983, London: The Metals Society.
43. Dunand, D.C. and B. Derby, *Creep and thermal cycling*, in *Fundamentals of Metal Matrix Composites*, S. Suresh, A. Mortensen, and A. Needleman, Editors. 1993, Butterworth-Heinemann: Boston. p. 191-214.
44. Slaughter, W.S., N.A. Fleck, and B. Budiansky, *Compressive failure of fiber composites: The roles of multi-axial loading and creep.* Transactions of the ASME- Journal of Engineering Materials and Technology, 1993. **115**: p. 308-313.
45. Bowman, R.R. *Influence of the interfacial characteristics on the mechanical properties of continuous fiber reinforced NiAl composites.* in *Intermetallic Matrix Composites II*. 1992: MRS.
46. Proulx, D. and F. Durant. *Creep failure of the $CuAl_2$ lamellar eutectic.* in *Failure Modes in Composites II*. 1974: TMS/AIME. p. 188-196.
47. Alman, D.E. and N.S. Stoloff, *The elevated temperature compressive behavior of a $MoSi_2$/20 v% Nb aligned fibrous composite.* Scripta Metallurgica et Materiala, 1993. **30**: p. 203-208.
48. Weber, C.H., *et al.*, *High temperature deformation and rupture in SiC-C composites.* Materials Science and Engineering A, 1995. **196**: p. 25-31.
49. Nguyen, D.H. and A.A. Ogale, *Compressive and flexural creep behavior of carbon fiber /PEEK composites.* Journal of Thermoplastic Composite Materials, 1991. **4**: p. 83-99.
50. Robinson, S.L. and O.D. Sherby, *Mechanical behavior of polycrystalline tungsten at elevated temperature.* Acta Metallurgica et Materialia, 1969. **17**: p. 109-125.
51. Pugh, J.W., *Tensile and creep properties of tungsten at elevated temperatures.* Proceedings of ASTM, 1957. **57**: p. 909-916.
52. Harris, B. and E.G. Ellison, *Creep and tensile properties of heavily drawn tungsten wire.* Transaction of the ASM, 1967: p. 744-754.
53. Misra, A.K., *Thermodynamic analysis of compatibility of several reinforcement materials with β phase NiAl alloys*, 1988, NASA-4171.
54. Frost, H.J. and M.F. Ashby, *Deformation-Mechanism Maps*. 1982: Pergamon.

55. Massalski, T.B., *Binary Alloy Phase Diagrams.* Vol. 3. 1990, Materials Park, OH: ASM.
56. Massalski, T.B., *Binary Alloy Phase Diagrams.* Vol. 1. 1990, Materials Park, OH: ASM.
57. Sadananda, K. and C.R. Feng, *The creep of intermetallics and their composites.* Journal of Materials, 1993(May): p. 45-48.
58. Rudy, M. and G. Sauthoff. *Creep behavior of the ordered intermetallic (Fe, Ni)Al phase.* 1985: MRS.
59. Miracle, D.B. and R. Darolia, *NiAl and its Alloys*, in *Intermetallic Compounds*, J.H. Westbrook and R.L. Fleischer, Editors. 1994, Wiley. p. 53-72.
60. Goto, S. and M. McLean, *Role of interfaces in creep of fiber reinforced metal matrix composites - I. Continuous fibers.* Acta Metallurgica et Materialia, 1991. **39**(2): p. 153-164.
61. Johnson, A.F., *Creep characterization of transversely-isotropic metallic materials.* Journal of the Mechanics and Physics of Solids, 1977. **25**: p. 117-126.
62. Swift, D.G., *Elastic moduli of fibrous composites containing misaligned fibers.* Journal of Physics D:Applied Physics, 1975. **8**: p. 223-240.
63. Piggott, M.R., *A theoretical framework for the compressive properties of aligned fiber composites.* Journal of Materials Science, 1981. **16**: p. 2837-2845.
64. DeSilva, A.R.T., *Creep deformation and creep rupture of fiber reinforced composites.* in *Third International Conference on Composite Materials.* 1980. Paris: Pergamon Press. p. 1115-1128.

GRC-35